Transportation and Installation of the TetraSpar Floating Offshore Wind Turbine

Master Thesis

Eduardo Benitez Villaespesa
Cristino Manuel Gonzalez
Nils G. K. Martin

Aalborg University
Faculty of Engineering and Science
Department of Civil Engineering

AALBORG UNIVERSITY

STUDENT REPORT

Title:

Transportation and Installation of a Floating Offshore Wind Turbine

Project period:

02. February 2018 - 15. June 2018

Participants:

Eduardo Benitez Villaespesa

Cristino Manuel Gonzalez

Nils G. K. Martin

Supervisor:

Morten T. Andersen

Editions: 04

Report pages: 53

Completed June 15, 2018

Front page image source:

[https://phys.org]

Abstract:

Offshore wind energy faces the need to reduce it cost to become a competitive alternative in the global renewable energy market. The Stiesdal TetraSpar is an innovative floating offshore wind turbine foundation that industrializes floating foundations, which associates advantages from known floating structures such as spar, semi-sub and tension leg platform foundations. The current project is classified in a level 6 in regards to a Technology Readiness Level, in other words, the TetraSpar model needs to be demonstrated in a relevant environment. Until now, only the fully installed structure has been tested, therefore it is intended to cover the gap from its launch in harbour to its operational stage. This process includes four stages: tow out, hook up, lowering and ballast of the counterweight. First, transportation is studied by analyzing different configurations in regards of counterweight positions as well as towing directions of the structure. On this basis, a configuration is chosen to be investigated during the installation process. The aim is to study the hydrodynamic response of the structure to prove its safety within the designed environmental conditions. Finally, advises are given regarding both transportation and installation of the TetraSpar floating offshore wind turbine.

Preface

This report is produced by a group of 4th semester students at Aalborg University as a part of the Master programme in Structural and Civil Engineering. It is written by Eduardo Benitez-Villaespesa, Cristino M. Gonzalez and Nils G.K. Martin and supervised by Morten T. Andersen. The theme of the project is hydrodynamics of floating offshore structures during its transportation and installation processes. The basis of the project is the experimental assessment of the TetraSpar structure. Further investigations are done numerically and analytically. From this study, the Master Thesis was written and two scientific papers arise. Basic knowledge regarding structural mechanics and fluid and water wave mechanics is required when reading the report to have an adequate understanding of the content. The final form of this work consists of four parts.

- Part I - Master Thesis.
- Part II - Paper A "Towing Investigation of the TetraSpar Floating Offshore Wind Turbine".
- Part III - Paper B " Investigation of the Dynamic Response of the TetraSpar Floating Offshore Wind Turbine during Installation".
- Part IV - Appendix for the Master Thesis.

Reading guide

Throughout the project references will be made to source material, which is located in the bibliography at the end of the report. Source references in the report will follow the Harvard method and appear in the text with the name of the author, organisation etc., followed by the year of publication in the form of either "[Name, Year]" or "Name [Year]" depending on the context. The literature in the bibliography is written with author, title and date.

Furthermore figures and tables in the report are numbered in accordance to the respective chapters. This means that the first figure or table in chapter 3 for instance is numbered 3.1 followed by 3.2 etc. Explanatory text is found under the given figures and above tables. Figures without references are composed by the project group. Equations are referred to by a number in parenthesis, e.g. (3.1).

Cristino M. González	Eduardo Benítez	Nils G.K. Martin

Table of contents

Part I

Thesis

Introduction 1

Since 2000 the European wind market is under a considerable growth. In 2017 Europe installed 16.8 GW with a total installed capacity of 169 GW, which makes wind energy the second largest form of energy behind gas installations.

According to [EWEA, 2017], in 2020 renewables will be able to power approximately 35% of the European Union (EU) electricity mix. Figure 1.1a represents the evolution of the different energy sources for the electricity production in the upcoming years. Wind energy will become the leading source of renewable energy by producing around 16.5% of the total electricity consumption, representing one third of the total green energy.

As seen in Figure 1.1b, wind energy investments accounted for 52% of the new clean energy finance in 2017, compared to 86% in 2016. This is explained by the reduction of costs in the industry, which means that it is possible to finance more wind power with less money. Germany is the leading country in EU regarding the installed wind power, representing the 45% of all new installations in 2017. It is followed by United Kingdom with 26% and France with 10% of all new installations. Onshore wind projects alone generated 35% of the total investment activity in the renewable energy sector, nevertheless the offshore market is under constant development.
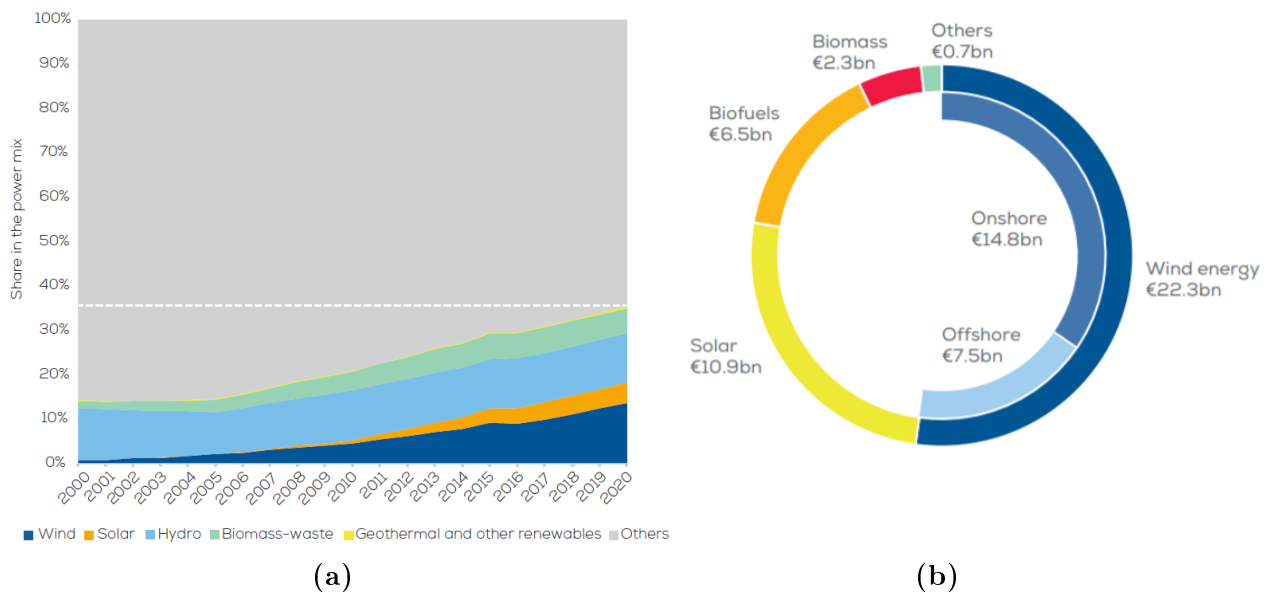

(a)   (b)

Figure 1.1. **(a)** Evolution of the EU electricity mix. **(b)** Clean energy investment in 2017. [EWEA, 2017].

1.1 Offshore Wind Energy

Traditional onshore turbines originally have been dominating the market, however recent advancements in the technology has lead this industry to look towards implementing offshore wind farms [NES, 2016]. Offshore wind energy is now an attractive option due to the advantages that it presents, the fact that the average wind speed is higher and more consistent results in higher capacity factors compared with onshore wind. Besides, there is no visual impact, interference with land usage nor noise impact.

In Figure 1.2 the European bathymetry shows a limited access to shallow waters for countries such as France, Spain, and Portugal facing the Atlantic Ocean and countries surrounding the Mediterranean Sea such as Italy and Greece. These countries represent a large potential market in the offshore wind industry. Therefore, the floating offshore wind energy faces the need to reduce it cost to become a more competitive alternative in the global renewable energy industry. Some improvement should cover the standardization of the sector, reduction of manufacturing and installation costs.
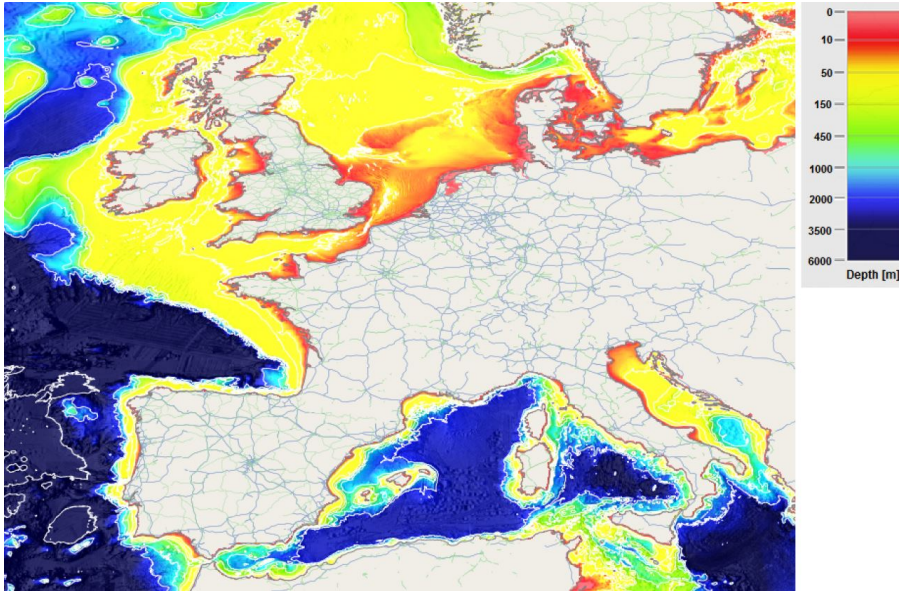

Figure 1.2. European bathymetry. [EMODnet, 2016].

From Figure 1.3, it is seen that the most installed type of offshore wind turbine in 2017 is the fixed monopile foundation. This kind of structure is preferred due to its feasibility and low cost production. On the other hand, deploying fixed foundations in regions with increasing water depth, it dramatically increases costs as well as limitations with regards to the maximum operational depth of existing and scheduled new wind turbine installation vessels [Musial et al., 2006]. Unlike fixed-bottom plants, floating structures are not required to be site-specific in terms of conceptual design and lower cost mass-production is a more viable proposition.

According to [New Energy Update, 2016], simple, safe and efficient in-shore assembly is one of the main advantages of floating wind units compared with bottom-fixed. Onshore assembly, combined with the ability to tow a fully assembled structure to site via tug boats for installation rather than require expensive Dynamic Positioning (DP) vessels or heavy lift jack-ups, should provide significant CAPEX savings.
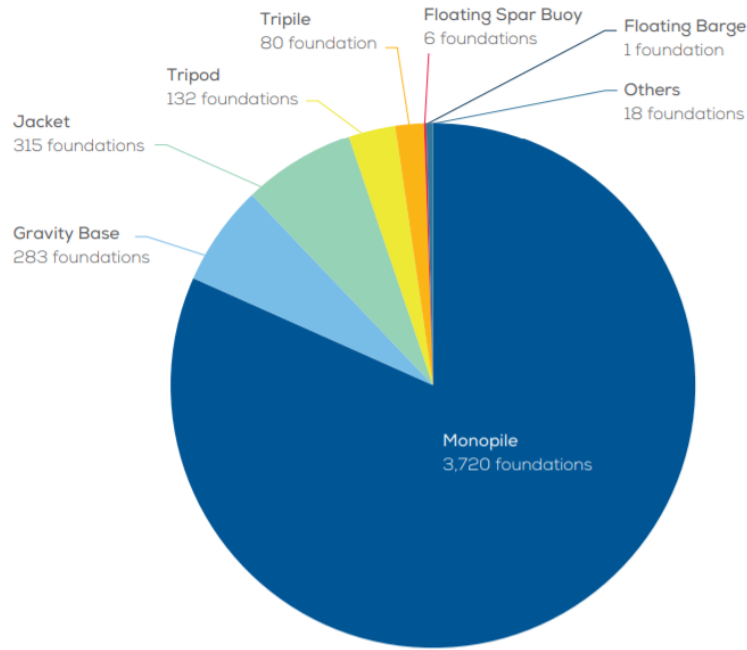
Figure 1.3. Share of substructure types for wind turbines for 2017. [EWEA, 2017].

Table 1.1 shows the significant cost incurred in transporting and installing fixed offshore wind turbines, which can be up to five times the cost for floating offshore wind turbines (FOWTs).

Table 1.1. Vessel costs for different offshore wind turbines. [New Energy Update, 2016]

Fixed-bottom installations		Floating wind installations	
Vessel	**Day rate**	**Vessel**	**Day rate**
Heavy lift vessel	€150 k − 500 k	Standard tug boat	€30 k − 60 k
Jack-up vessel	€150 k − 200 k	Anchor handling tug	€20 k − 50 k
Mobilisation	Several M €	Mobilisation	€< 100 k

1.2   Floating Offshore Wind Energy

The overall benefits shown in the previous section has lead to an interest to propose the study of floating offshore wind turbines. Today, a large amount of FOWT designs are present in the market. They usually are attached to the following concepts: spar-buoy, semi-submersible and tension leg platform (TLP). As seen in Figure 1.4, these structures have their differences, which at the same time have its advantages and disadvantages. The spar-buoy concept is a simple concept which tolerate moderate wave loads and has a simple mooring system, but it is a heavy structure which requires at least 80 metres water depth and requires special installation vessels. The semi-submersible concept is a versatile structure which allows for a large range of water depth with a simplified installation process where the wind turbine is installed in the harbour and towed to site, but it is a heavy steel structure. Finally, the TLP concept is a lightweight structure with a simplify installation process as the semi-submersible concept. It is a complex structure where the mooring system is expensive and requires special vessels for installation.
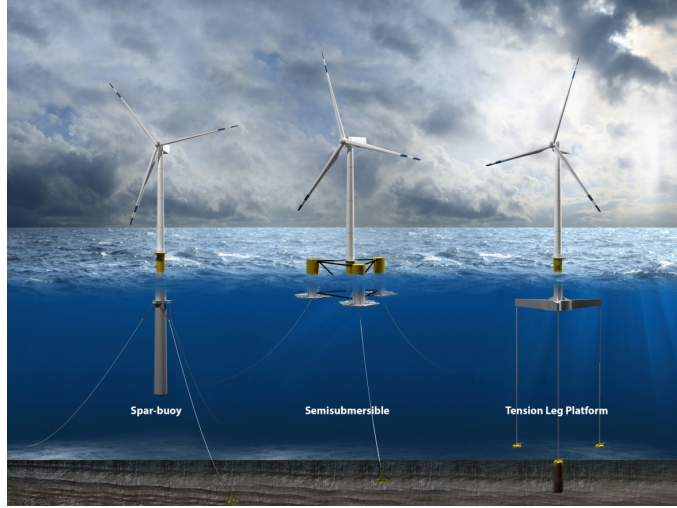
Figure 1.4. Floating platform concepts for offshore wind turbines.

In 2016, Henrik Stiesdal, a Danish inventor and businessman in the modern wind power industry, proposed a new concept of FOWT. It combines the best advantages from spar-buoy, semi-submersible and TLP concepts. This lead to the TetraSpar concept, which is a simple tetrahedral structure with a counterweight (CW), as seen in Figure 1.5. The structure is an innovative floating offshore wind turbine foundation that industrializes floating foundations by simplifying manufacturing and installation processes. Manufacturing process is simplified by using simple circular steel members that are joint in harbour. The wind turbine is installed on the floater so that the structure can be towed and installed at the chosen site as the floater has semi-submersible stability. Once it is on site, the counterweight, also called keel, is ballasted pulling down the structure and acting as a spar-buoy floating foundation. Figure 1.6 shows the different stages of the Stiesdal TetraSpar installation concept. This versatile structure can be installed in different locations going from shallow to deep water, by being built in as a fixed foundation in shallow waters and as a spar-buoy foundation in deep waters.
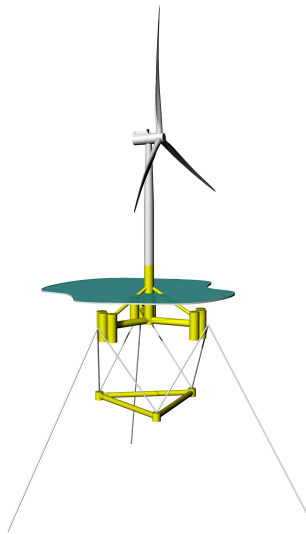

Figure 1.5. Stiesdal TetraSpar concept.[Henrik Stiesdal, 2017]

1.3   Problem formulation

Due to the technological progress achieved, a hydrodynamic study is required to understand the behaviour of the TetraSpar during transportation and installation as it represents large expenses in the total costs of the floating foundation. These processes are divided into four stages: tow out, hook up, ballasting of the counterweight and spar stage, as seen in Figure 1.6. This hydrodynamic study lead to form the following inquiries:

- How does the TetraSpar floating foundation behaves during towing, and to what extent do the analytical and numerical solutions verify the experimental models with different counterweight configurations?
- How does the TetraSpar floating foundation behaves from hook-up stage to the spar configuration, and to what extent do the analytical and numerical solutions verify the experimental models with different counterweight configurations?
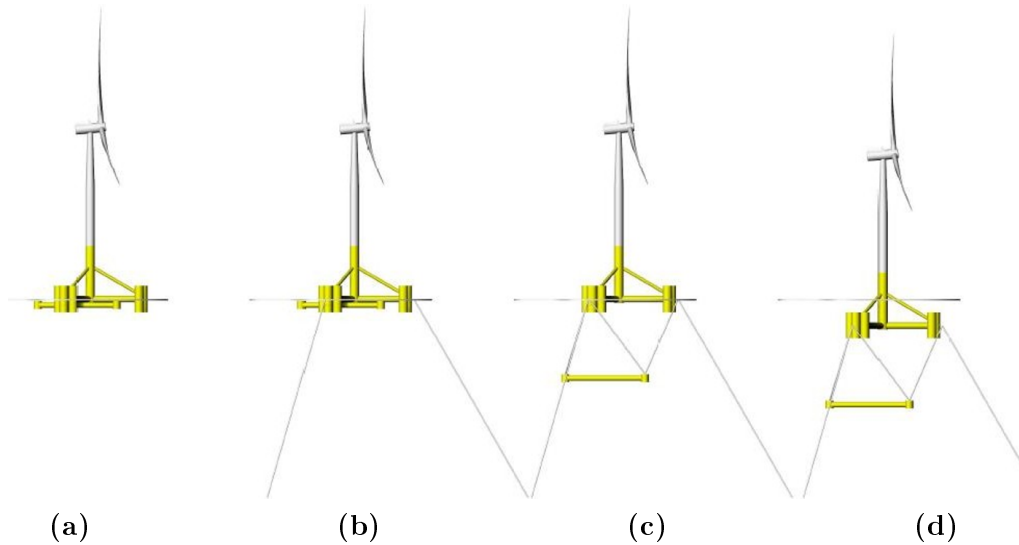

      (a)   (b)   (c)   (d)

Figure 1.6. Stiesdal TetraSpar installation concept. **(a)** Floating configuration **(b)** Hook-up configuration **(c)** Ballasting **(d)** Spar configuration. [Henrik Stiesdal, 2017]

1.4   Project scope

The project uses as a starting point the test model of the TetraSpar floater of Stiesdal Offshore Technologies that got tested out in a test campaign done by DTU Wind Energy, Stiesdal Offshore Technologies and DHI Denmark. The FOWT is tested in different configurations with a 1:60 model scale with a 10MW wind turbine. From this model, the towing process is tested with different counterweight configurations in a wave flume at Aalborg University. Then, analytical and numerical models are built and benchmarked to the laboratory work. From these results, the most suitable counterweight configuration is chosen, and further investigations are carried out regarding the end of the installation process. From hook-up to final stage, the TetraSpar is studied experimentally in a wave basin at Aalborg University, then numerical models made with FAST v8 are benchmarked. The TetraSpar's motion during installation is studied by performing regular waves based on Hywind project sea states.

Research Summary

2

This Chapter gives an overview of the theory used in the papers and methods applied to answer the formulated questions in Chapter 1. Two papers are the results of a research based on analytical, numerical and experimental analysis. Both transportation and installation analyses consider the structure as a rigid body, which means that the motion of the wind turbine, the platform and the counterweight remains constant in time indifferently of the forces applied on it. Six rigid body degrees of freedom (DOF) are used to describe the motion of the platform. It includes translational and rotational DOFs, as seen in Figure 2.1. The translational DOFs are defined by surge, sway and heave displacements in the $x-$, $y-$ and $z-$directions. Rotations are characterized by roll, pitch and yaw around $x-$, $y-$ and $z-$axes. The interaction of all these DOFs and the wide ranging ocean conditions implies the simplification of the forces applied on the system. Therefore, only the hydrodynamic performance and response are studied.
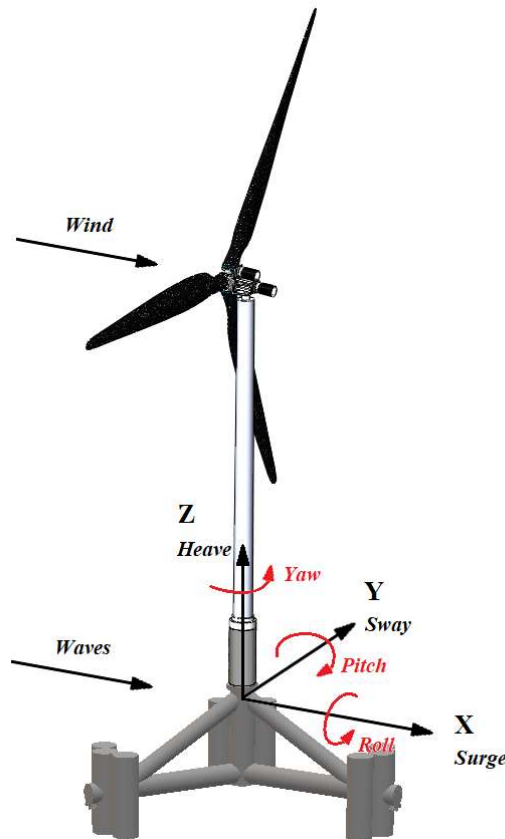

Figure 2.1. DOFs of the TetraSpar FOWT. [F.J.Madsen et al., 2017]

2.1   Experimental Assessment

Two different experiments are carried out. In this section a description of the scaled model is presented. Then, the transportation set-up is introduced, where different TetraSpar configurations are tested in regards of counterweight positions and towing directions. On this basis, a configuration is chosen to be investigated during the installation process. Next, the basin set-up is explained for two of the installation stages. The aim is to study the hydrodynamic response of the structure to prove its safety within the designed environmental conditions.

2.1.1   Scale models

The scaled model is provided by [Henrik Stiesdal, 2017]. It is scaled to 1:60 following Froude scale law. Table 2.1 shows the scaling factor of the most common variables used within the test according to Froude's law, being $\lambda = 60$ the multiplication factor.

Table 2.1. Scaling of variables using Froude's law.

Variable	Symbol	Scale factor	Units
Linear dimensions	D	λ	[m]
Time or period	T	$\lambda^{1/2}$	[s]
Force	F	λ^3	[N]
Mass	m	λ^3	[kg]
Moment of inertia	I	λ^5	[m^4]
Fluid velocity	u	$\lambda^{1/2}$	[m/s]

Floater model

As seen in Figure 2.2, the floater is is divided into three parts: wind turbine, floater and counterweight. The floater is composed of a central column joint to three sets of buoyancy tanks. The central column is connected to three radial tubes and three diagonal tubes. A connection plate and a transition piece are installed on top of the central column, which form the interface between the floater and the wind turbine tower. Finally, the floater is balanced by a CW and attached to the fairlead by six chains. Dimensions of the TetraSpar are shown in Figure 2.3.
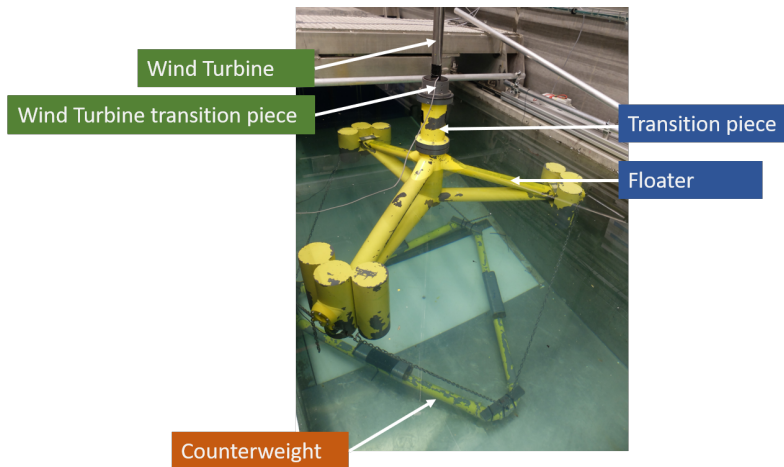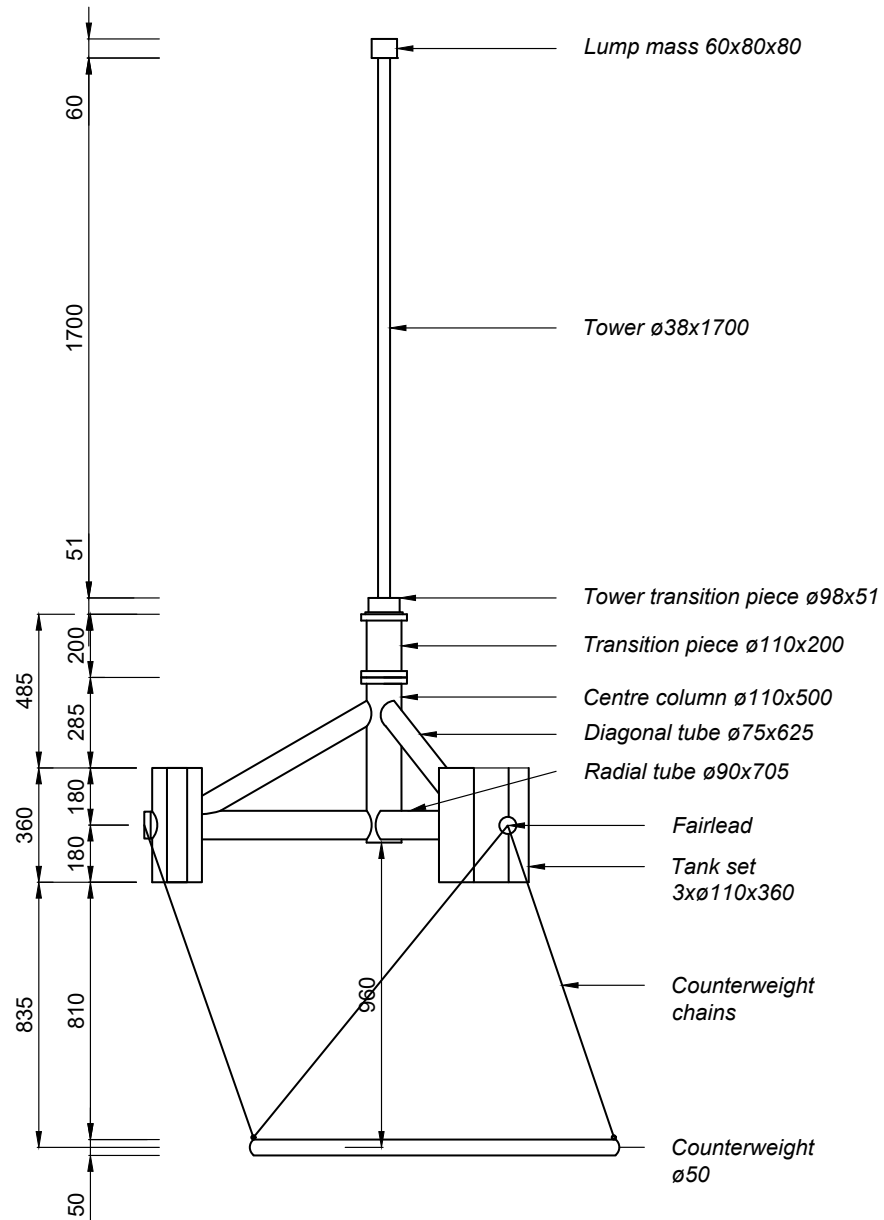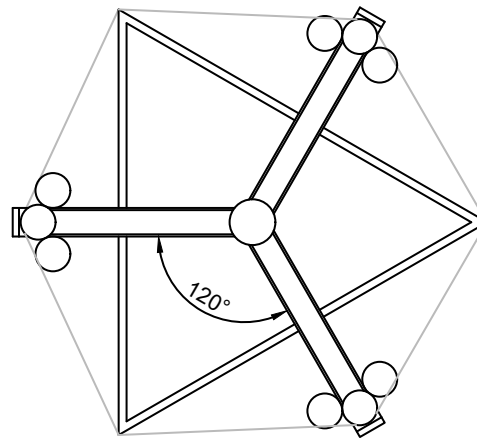

Figure 2.2. Floater parts and nomenclature.

Side View

Lump mass 60x80x80

Tower ø38x1700

Tower transition piece ø98x51

Transition piece ø110x200

Centre column ø110x500

Diagonal tube ø75x625

Radial tube ø90x705

Fairlead

Tank set
3xø110x360

Counterweight
chains

Counterweight
ø50

60

1700

51

200

485

285

360

180

180

835

810

50

960

Plan View

120°

Figure 2.3. Detail drawing of the 1:60 scale model.

Wind Turbine model

The TetraSpar is designed to support 10 MW wind turbines. Therefore, this project is using the DTU 10 MW Reference Wind Turbine, for which the description is given in [Bak et al., 2013]. An equivalent wind turbine model is built at Aalborg University. The DTU 10 MW Reference Wind Turbine and the equivalent model are shown in Figure 2.4. In this project the aerodynamic influence of the wind turbine on the floating foundation is not studied, therefore a lump mass replaces the nacelle, rotor and blades. The actual 10 MW model is built to match the mass, inertia, and height properties of the DTU 10 MW Reference Wind Turbine. These are shown in Table 2.2 with the Froude model scale. An additional transition piece is installed so that the tower can be connected to the floater's transition piece. Although this piece is lowering the centre of gravity of the wind turbine of about 10% in comparison to the Froude model scale, it is considered acceptable.

Table 2.2. Global properties of the 10 MW Reference Wind Turbine, Froude scaled 1/60 model, and the AAU 1/60 scaled model.

Dimension	10MW Reference Wind Turbine	Froude Model Scale	Actual Model Scale
Nacelle and rotor			
Nacelle+hub+rotor mass	$677\ t$	$3.13\ kg$	$3.14\ kg$
Tower			
Diameter	$7.82 - 5.50\ m$	$130 - 92\ mm$	$38\ mm$
Tower length	$100.4\ m$	$1.67\ m$	$1.73\ m$
Hub height in floating conf. from MWL	$125\ m$	$2.08\ m$	$2.43\ m$
Hub height in spar conf. from MWL	$119\ m$	$1.98\ m$	$2.14\ m$
Mass	$516\ t$	$2.39\ kg$	$2.23\ kg$
Transition piece mass	-	-	$0.38\ kg$
Nacelle, rotor and tower			
Centre of gravity	$93.15\ m$	$1.55\ m$	$1.30\ m$
Moment of inertia about $x-$axis	$8.3 \cdot 10^9\ kg \cdot m^2$	$10.63\ kg \cdot m^2$	$10.27\ kg \cdot m^2$
Moment of inertia about $y-$axis	$8.27 \cdot 10^9\ kg \cdot m^2$	$10.58\ kg \cdot m^2$	$10.27\ kg \cdot m^2$
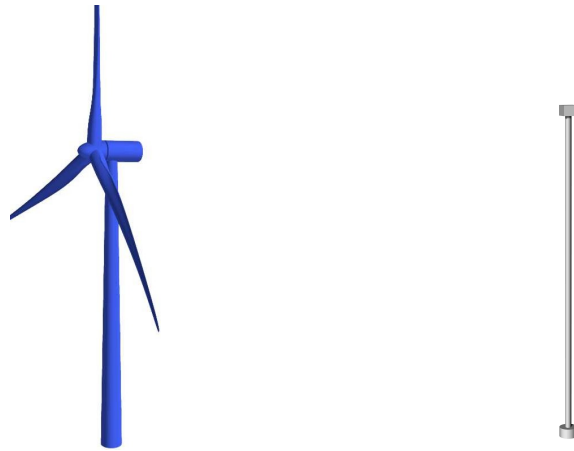
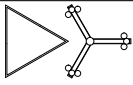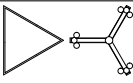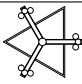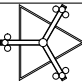***Figure 2.4.*** DTU 10 MW Reference Wind Turbine and Aalborg University Scale Model Wind Turbine.

2.1.2 Towing assessment

The transportation of the TetraSpar system is investigated when it is being towed out to site. For this purpose, four different configurations are studied with the aim of determining the one that presents less resistance force. The notation used throughout this work is presented in Table 2.3, where a top view of the different configuration is also presented. Note that the current direction goes from right to left. Both A configurations stand for the CW being placed behind the structure when being towed. The difference between A_1 and A_2 is that the latest one is rotated 180° with respect the towing direction, although the CW remains in the same position. On the other hand, B configurations stand for the CW being placed under the TetraSpar, and again, B_2 corresponds to the system being rotated 180°.

Table 2.3. Towing configurations.

Configuration	Analytical	Experimental	Numerical
	A	A_1	A_1
		A_2	—
	B	B_1	—
		B_2	—

Test procedure

Tests are carried out in Aalborg University's hydraulic laboratory wave flume. The maximum depth of the flume is 1.53 meters at one of its sides, while in the other part its depth reaches up to 1.37 m. The difference in height is covered by an slope of approximately 4 meters long. Figure 2.5 shows an overview of the experimental setup in the flume for the B_2 configuration.
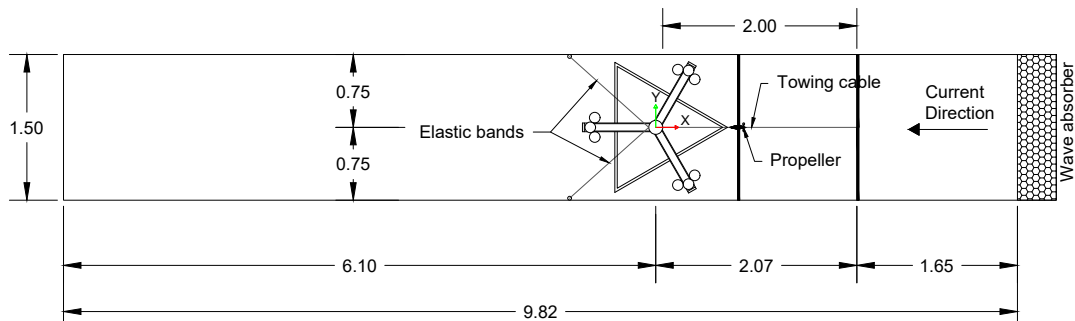

Figure 2.5. Plan view of the experiment set-up for B2 configuration.

A cable is attached to the TetraSpar at the transition piece. In order to simulate the towing procedure, a current is generated against the floating structure, which remains fixed thanks to elastic bands. In Figure 2.6, the four different set-ups tested are depicted. Each configuration is tested with different current velocities. The characterization of the flow is described in Appendix A.
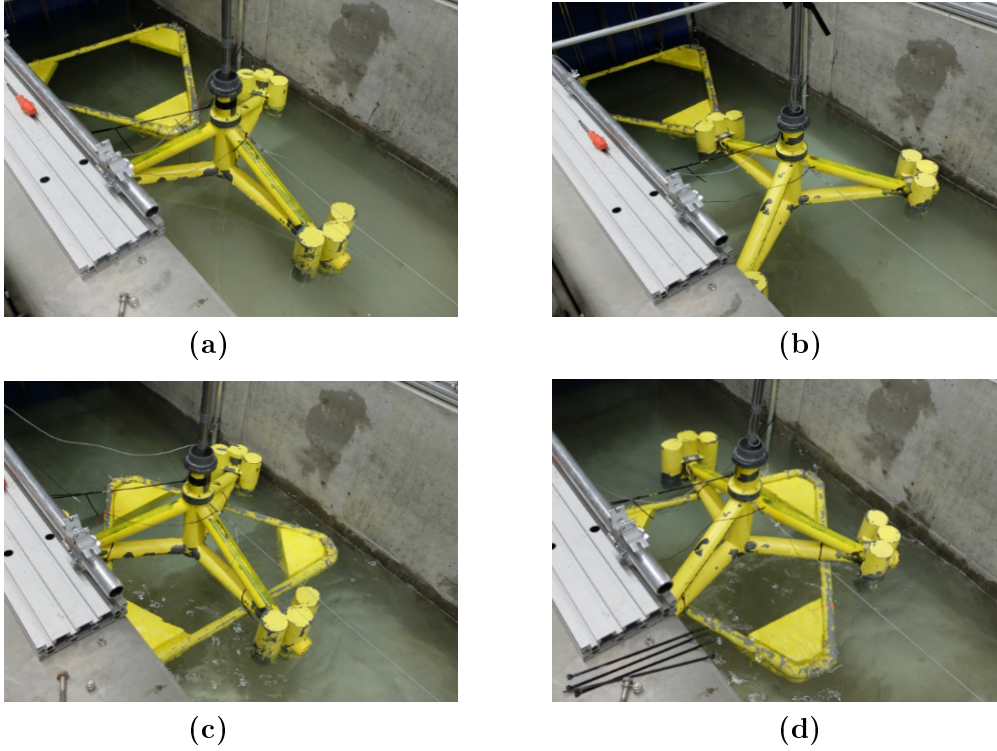
(a)   **(b)**

(c)   **(d)**

Figure 2.6. Towing test configurations. **(a)** A_1. **(b)** A_2. **(c)** B_1. **(d)** B_2.

Instrumentation

An overview of the TetraSpar instrumentation in the wave flume is provided in Figure 2.7. The instrumentation is detailed below.
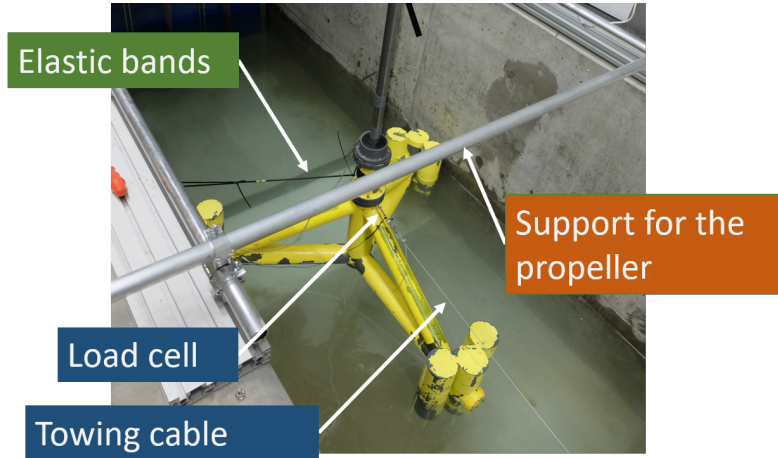

Figure 2.7. Wave flume instrumentation set-up.

- Load cell: A load cell is placed at the connection towing cable-structure. It is used to measure the tension present in the cable. The load cell is calibrated by applying known forces and a regression line is determined. It is used to convert the voltage readings to forces. The calibration results are shown in 2.8.
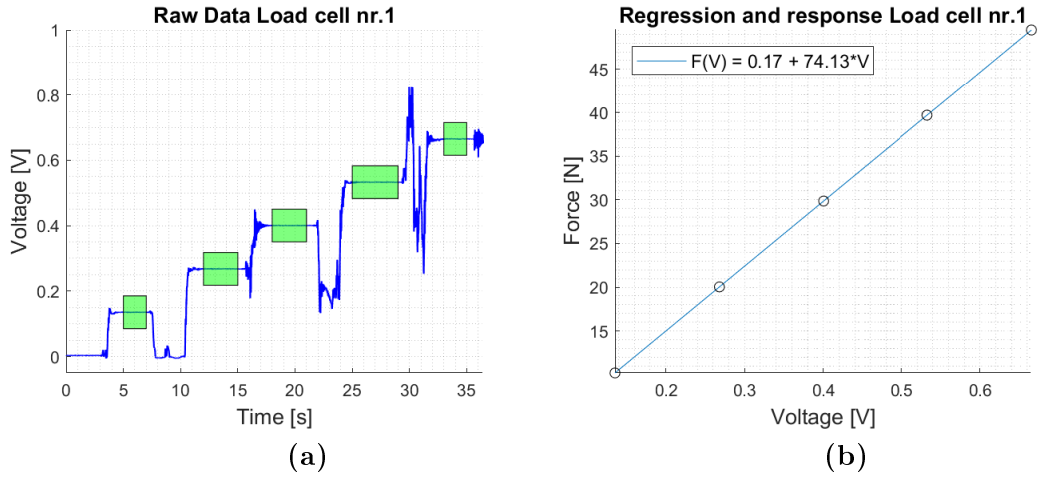
Figure 2.8. Load calibration. **(a)** Reading of the load cell, selected values are shown in green. **(b)** Regressions and response of the load cell.

- Propeller: This device is used to measure the current velocity. It is place at different heights in order to determine the current profile as a function of depth.
- Elastic bands: These are used to keep the structure in place as the wave flume is narrow. These bands are placed in a such way that the influence of them is limited.

2.1.3 Installation assessment

In the presented work, effort is made to better understand the installation responses of the TetraSpar system. Special attention is paid to hook-up and spar configurations. Hook-up configuration corresponds to the mooring of the floater at the designed location. On the other hand, spar configuration represents the final position of the structure once the CW is ballasted.

Test procedure

Tests are carried out at the Hydraulic laboratory at Aalborg University where the wave basin is 14.6 m x 19.3 m x 1.5 m (length x width x depth). The bottom of the basin is lowered under the structure by the help of a deep water pit of 6.5 m x 2.0 m. It is set to a depth of 1.5 m so that a deep water condition is fulfilled during testing. The structure is placed above it.

Several sea states are implemented to get some initial results of simulated dynamic responses of the TetraSpar during the installation process. These sea states follow the Norwegian Continental Shelf defined in Beels et al. [2007]. The wave climate is taken at Utsira, in Norway with a mean water depth of 200 meters and a a distance of 21 km away from the shore. During the test campaign only the most extreme sea states are tested, corresponding to sea states 7 to 10.

On Figure 2.9 two set-ups are seen, these are representative of the hook-up and spar configurations. Each configurations are tested with free oscillation tests and regular waves. On Figure 2.10 a plan view can be seen where the mooring lines are place at 120° from each other.
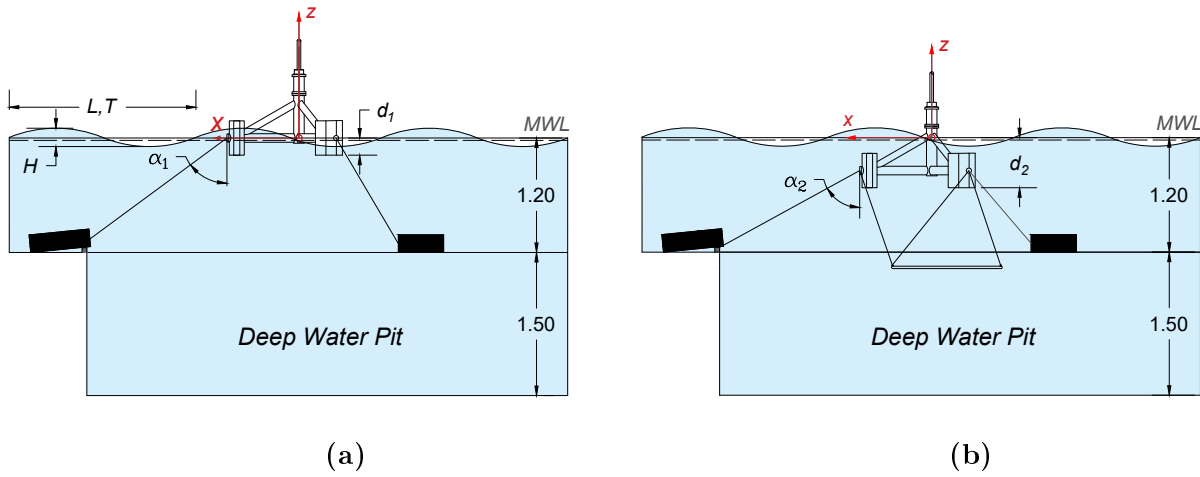
(a)   (b)

Figure 2.9. Basin set-up. **(a)** Hook-up configuration. **(b)** Spar configuration.
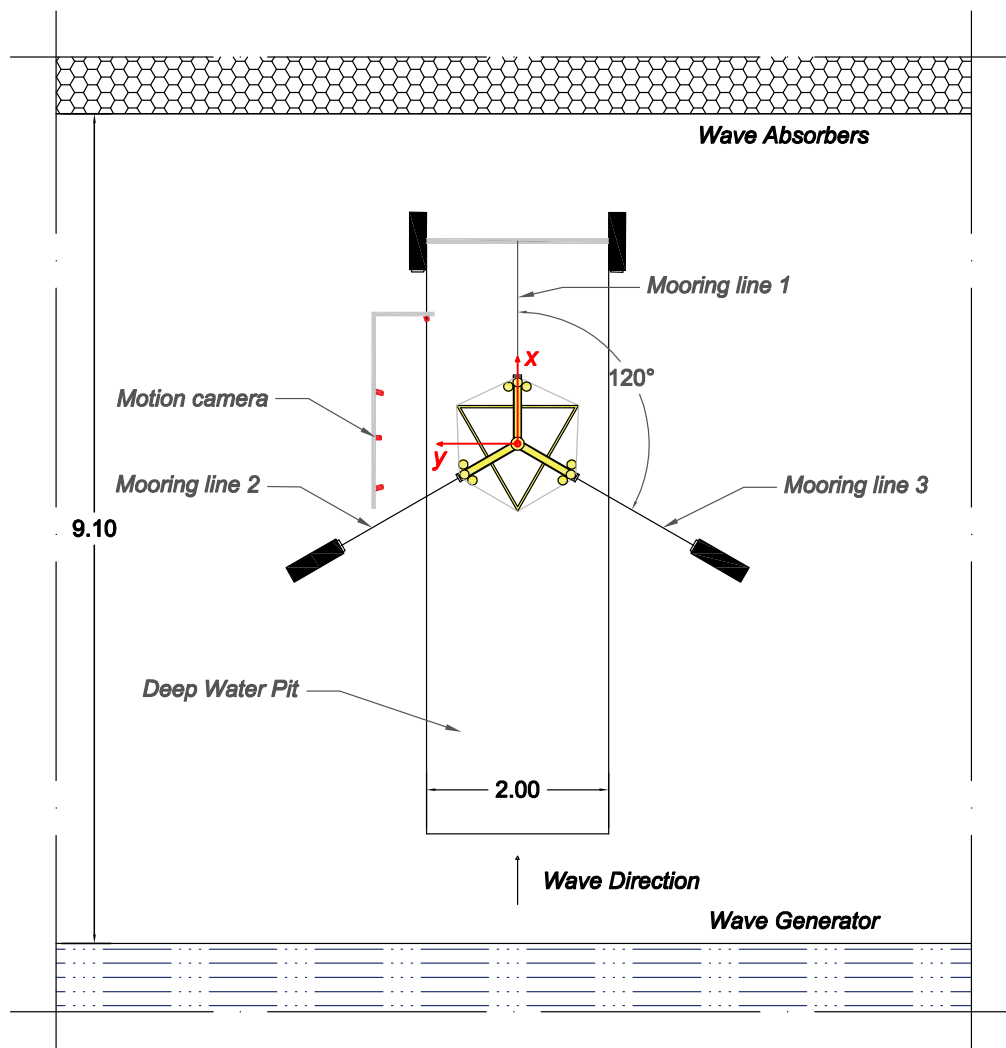

Figure 2.10. Wave basin experimental set-up: plan view.

Instrumentation

An overview of the TetraSpar instrumentation in the wave basin is provided in Figure 2.11. The instrumentation is detailed below.

- Mooring gauge: Three load cells are placed at the end of mooring lines number one, two and three. These are used to measure the tension present in the mooring lines.
- Wave gauges: These are used to measure the wave elevation during testing.
- Motion cameras: Four OptiTrack Flex cameras are used to register the motion in six DOFs. These records the motion with the help of five reflective markers. The are placed in a random positions which provide non-symmetrical markers for the cameras to measure. The cameras are calibrated following the instructions given by the manufacturers.
- Wave paddles: Long-stroke segmented piston wave generator are used to generate waves.
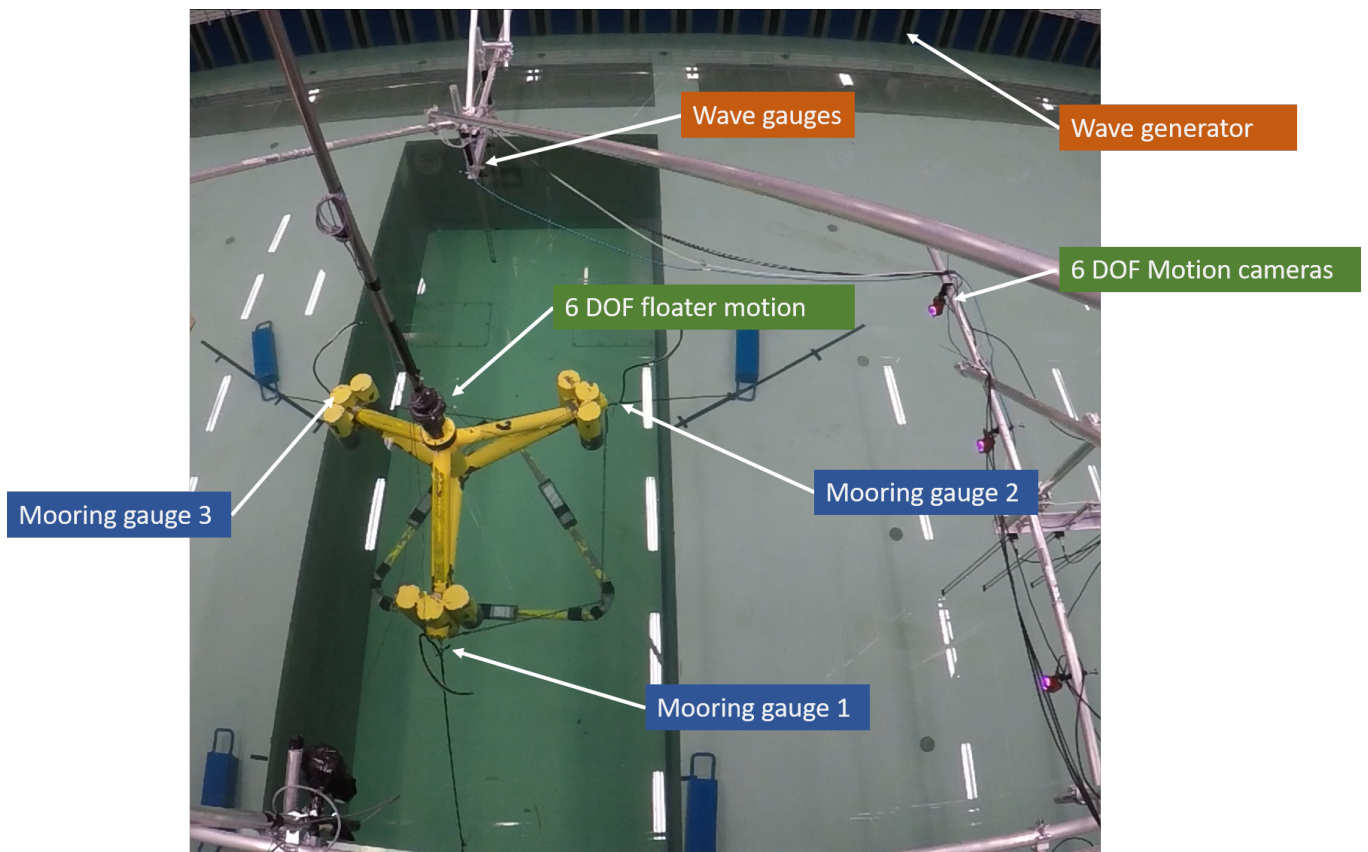

Figure 2.11. Wave basin instrumentation set-up.

2.2 Forces on a floating platform in a current flow

As stated in [Journée and Massie, 2001], the resultant force produced by the current on a floating platform is composed of:

- A viscous part, from the friction between the structure and the fluid; and due to pressure drag. For blunt bodies the frictional force may be neglected, since it is small compared to the viscous pressure drag.
- A potential part, with a component due to circulation around the object, and another component due to the free water surface (wave resistance). In most cases, the latter component is small in comparison with the first.

To calculate the current force in a structure that is not ship shaped as the TetraSpar, [Remery and van Oortmerssen, 1973] suggested that it can be estimated by dividing the structure in a number of members with elementary geometry such as cylinders, spheres, plates, etc; where the drag coefficient is known. Then the current force can be calculated from the summation of the contributions of all the member parts. This is done in paper [A] to compute the analytical solution, where the structure is considered to be formed by a group of slender cylinders; meaning that their diameters are small relative to the wave length. This assumption implies that the water motion near the cylinder is not changing both vertically and horizontally. The hydrodynamic force is determined by adding the linear inertia force, F_I, from potential theory, and the quadratic drag force, F_D, which was formulated by Morison, and expressed as

$$F(t) = F_I(t) + F_D(t). \tag{2.1}$$

or

$$F(t) = \rho V \ddot{u}(t) + \rho C_a(\ddot{u}(t) - \ddot{v}(t)) + \tfrac{1}{2}\rho C_d A(\dot{u}(t) - \dot{v}(t))|\dot{u}(t) - \dot{v}(t)| \tag{2.2}$$

where ρ is the water density, V is the volume of the body, A the area of the body, C_a the added mass coefficient, C_d the drag coefficient, u the fluid displacement and v the fluid displacement.

The transportation process investigated in paper [A] considers a fixed FOWT subjected to a steady current. Therefore, the linear inertia force in Eq.(2.2) is neglected due to the Keulegan Carpenter number (KC) tending to the infinite and the fluid velocity remaining the same over time. Moreover, the floater is considered fixed meaning that the body displacement is null. From there, the drag force in Eq.(2.3) becomes

$$F_D = \tfrac{1}{2}\rho C_d A \dot{u}|\dot{u}| \tag{2.3}$$

A simplification of the structure is done due to the complexity of the geometry. The forces are computed considering the projected area of the structure under water. Three different velocities are used for the calculations and the analytical results are compared experimentally and numerically. The numerical model is built following configuration A_1, as proved to be the best configuration based on experimental results shown in Figure 2.12. The governing equations used in the numerical solution are the Reynolds-averaged Navier Stokes (RANS). The turbulence model used to solve RANS equations is the Realizable $k - \epsilon$, which assumes that the turbulent viscosity, μ_t, is an scalar quantity.
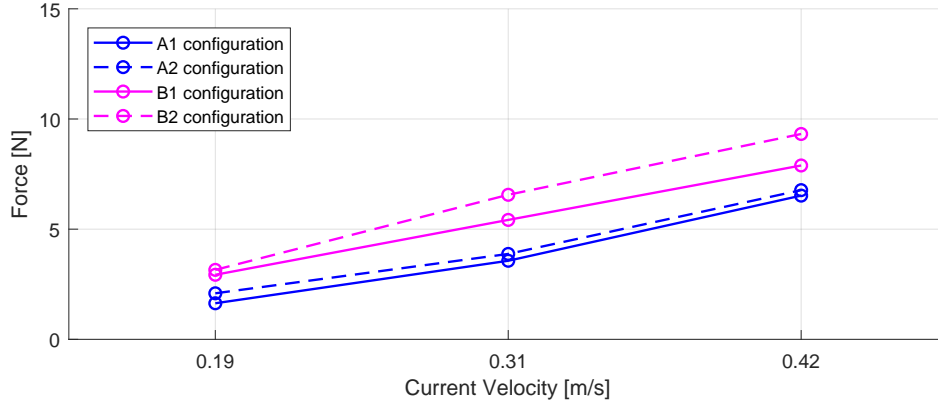
Figure 2.12. Experimental forces obtained for all the configurations.

The drag coefficient used in the analytical solution is set to 1.0, based on Reynolds number. The outputs are shown in Figure 2.13a, where it is seen that the numerical and experimental results are in good agreement. The analytical approach give a more conservative result, thus an optimal drag coefficient is determined. The determination of the drag coefficient is further explained in paper [A]. Results are shown in Figure 2.13b for the new C_d equal to 0.5. Finally, the results are compared with the numerical solution and, as the contribution of the floater and the counterweight can be divided, they have been analysed independently for a better understanding of the effect that each of the elements have on the structure. This can be seen in Figures 2.13c and 2.13d.
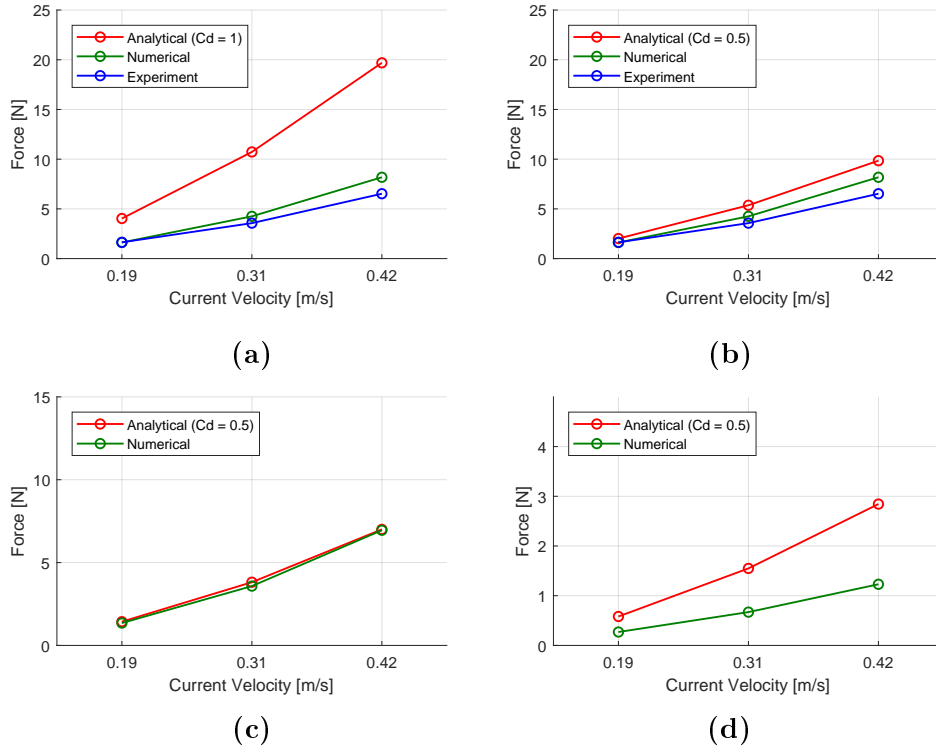

(a)

(b)

(c)

(d)

Figure 2.13. Forces in A_1 configuration. **(a)** Total force $C_d = 1$. **(b)** Total force $C_d = 0.5$. **(c)** Floater force. **(d)** Counterweight force.

2.3 Dynamic response of a platform during installation

In paper [B] the hydrodynamics behaviour is obtained by using the FAST wind turbine design code developed by the National Renewable Energy Laboratory (NREL). This non-linear time domain tool is capable of coupling aerodynamics, hydrodynamics, control strategy forces and structural dynamics. In the current work only the hydrodynamic behaviour is studied, which means that only certain modules of the program are considered. Further information regarding these modules are given in Appendix B. The hydrodynamics are included by assuming that the structure is a bluff body, which implies that the problem can be separated in three problems: one for diffraction, one for radiation and one for the incident undisturbed wave field. The total hydrodynamic force is expressed as

$$\phi = \phi_i + \phi_r + \phi_d, \tag{2.4}$$

where each term stand for the incident, radiation and diffraction wave velocity potential respectively. The linear radiation and diffraction forces of the platform are solved by making use of WAMIT [WAMIT Inc., 2016]. This Boundary Element Method (BEM), also called panel method, considers the potential flow formulation of the flow field by analysing the interaction of plane progressive waves with one or multiple interacting offshore structures. The WAMIT models used for the numerical analysis in paper [B] are shown in Figure 2.14. The different meshes developed correspond to the wetted area of the floater for each configuration. Additional outputs of the WAMIT calculations are used in FAST such as the displaced volume of water and the linear hydrostatic restoring matrix.
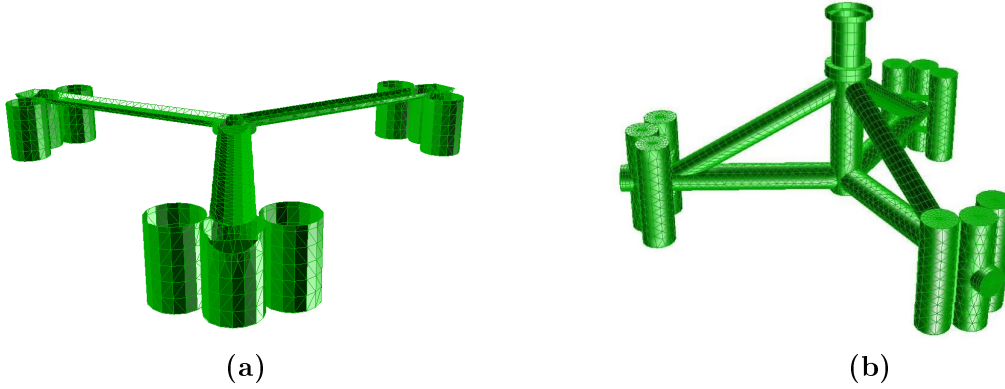

| (a) | (b) |

Figure 2.14. WAMIT input 3D mesh. **(a)** Hook-up configuration. **(b)** Spar configuration. [F.J.Madsen et al., 2017]

The hydrodynamic behaviour is governed by the general dynamic equation, expressed as

$$M_{ij}\,\ddot{x}_i(t) + C_{ij}\,\dot{x}_i(t) + K_{ij}\,x_i(t) = F_i^G + F_i^H + F_i^M, \tag{2.5}$$

where $x_i(t)$ corresponds to the 6 DOFs: surge, sway, heave, roll, pitch and yaw; $\dot{x}_i(t)$ and $\ddot{x}_i(t)$ correspond to the first and second derivatives respectively. M_{ij} stands for the mass matrix of the whole system (including the contribution of the added mass), C_{ij} is the linear damping matrix and K_{ij} the stiffness matrix. The total forces are represented by a combined system of forces composed of hydrodynamic, F_i^H, mooring, F_i^M, and gravitational forces, F_i^G.

In paper [B] the investigation of the installation process is done by studying the hydrodynamic behaviour of the floater in two configurations: hook-up and spar configurations. Between these two configurations, it is assumed that the structure behaves adequately in the considered time frame. The experimental campaign based on the scaled model is used in a first place to obtain characteristic hydrodynamic parameters such as natural frequencies and damping ratios. In Appendix A further information is given regarding the experimental results. These are used for the calibration of numerical models as explained in Appendix B.

After validation of the numerical models, response amplitude operators (RAOs) of the TetraSpar motion are determined from regular waves. The performed regular waves are based on characteristic sea states of the Norwegian Continentant Shelf defined in [Beels et al., 2007]. Ten sea states are considered numerically and four experimentally. The RAOs are shown in Figures 2.15 and 2.16. A good agreement of the responses is observed in pitch DOF in both numerical models. For the heave and surge DOFs, the results are more incompatible in hook-up configuration, but a fully coupled response is observed for all DOFs in spar configuration. In paper [B] it is supposed that the errors in the hook-up model are taking its origin in the mooring line modelling. Therefore, further investigation of the mooring system modelling is advised.
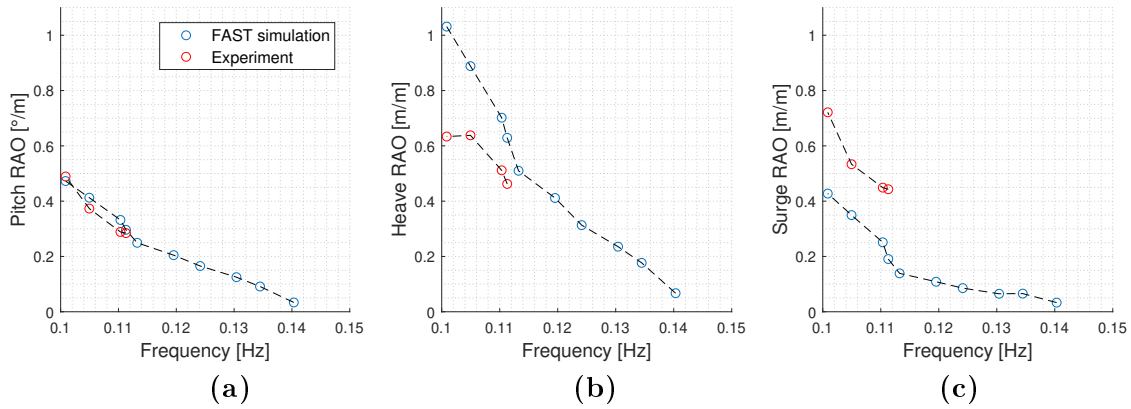

Figure 2.15. Experimental and FAST RAO results for hook-up configuration. **(a)** Pitch RAO. **(b)** Heave RAO. **(c)** Surge RAO.
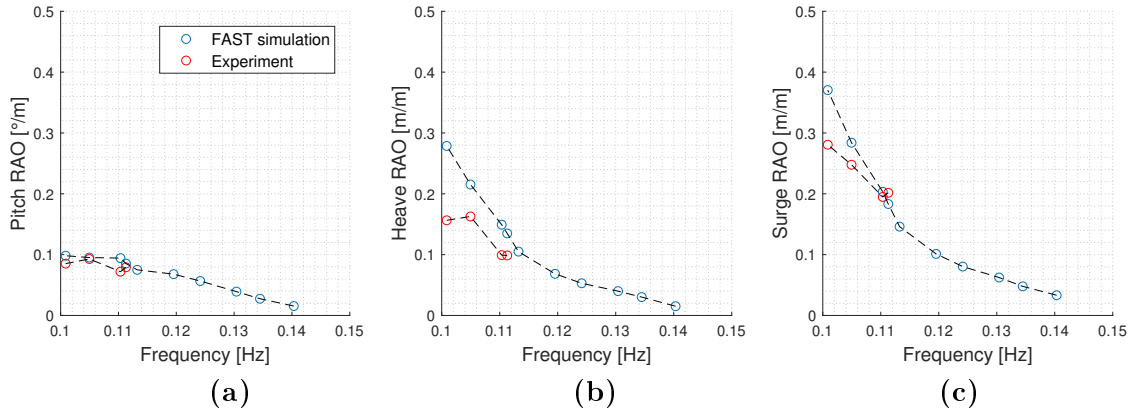

Figure 2.16. Experimental and FAST RAO results for spar configuration. **(a)** Pitch RAO. **(b)** Heave RAO. **(c)** Surge RAO.

Furthermore, it is observed that for higher wave frequencies, in other words lower wave heights and periods, the response of the TetraSpar is lowered. This has its importance as the installation process takes place in low sea states, which means that the floater is considerably safe from the ocean conditions.

Conclusion 3

For the past decades, the need for renewable energies has become a necessity as the aftermath of climate change around the world has proved to be an increasingly serious issue. Wind energy is a long-term potential alternative in the global renewable market, which is believed to produce five times the current global energy production. The development of floating offshore wind turbines is fundamental for the achievement of this goal. As offshore wind speed is 90% greater than onshore, these kind of structures are promising candidates for success on the market. A new concept of FOWT is proposed by H. Stiesdal. The TetraSpar, which is a combination of spar-buoy, semi-submersible and TLP concepts, shows great promises in regards of LCOE as the estimated price is between 42 to 84 €/MWh. These low prices are directly in competition with LCOE of land-based wind turbines. In the present work the hydrodynamic behaviour is investigated during transportation and installation. The output from theoretical, experimental and numerical analyses allows to give advises regarding the studied stages.

To determine the most feasible towing procedure, the investigation was performed by proposing four possible configurations for the TetraSpar tow out. Regarding the analytical approach, it is well known that in an ideal case, the drag coefficient should be determined from laboratory tests. However, due to limitations in the experiment the drag coefficient is determined by matching analytical and numerical forces. Given the satisfactory results obtained, this procedure is considered adequate for the studied scenarios. In general, the analytical solution is very good for predicting the most optimal configuration, but at the same time it is too conservative. Thus it demonstrates the need of using a numerical solution to compute the towing force accurately. Based on experimental and analytical forces, the most optimal configuration is found to be when the CW is placed behind the floater. This configuration reduces the towing force by a 30% in comparison to placing the CW below the floater.

From the chosen towing configuration, the dynamic response of the platform during installation is studied based on experimental and numerical work. It is concluded that during installation the response of the TetraSpar is limited during the advised installation sea state. In other words, the safety of the TetraSpar is fulfilled within the designed environmental conditions. Great importance is given to the experimental precision as it has a direct impact on the numerical models. The numerical tool FAST is used to determine the hydrodynamics of the floater. The construction of FAST models has demonstrated that FOWTs are complex dynamic structures where it is challenging to couple all the physical phenomena. Despite the constraints, after calibration of the numerical models, good agreement is found with the dynamic response of the structure in the wave basin.

The satisfactory findings from the presented work shows a promising future for the upcoming full scale TetraSpar floating offshore wind turbine and its development. A favourable towing procedure is proposed, and from the installation investigation it is proven that the TetraSpar is structurally safe. Hopefully, the work accomplished in this thesis will facilitate the design process of the full scale structure and move a step forward to end our reliance on fossil fuels and overcome the threats from climate change.

Part II

Paper A - Towing Investigation of the TetraSpar Floating Offshore Wind Turbine

Article

Towing Investigation of the TetraSpar Floating Offshore Wind Turbine

Eduardo Benitez Villaespesa [1,‡], **Cristino M. Gonzalez** [1,‡], **Nils G.K. Martin** [1,‡,*], **Lasse Sørensen** [1] and **Morten T. Andersen** [1]

1   Department of Civil Engineering, Aalborg University, Aalborg, Denmark; ebenit16@student.aau.dk; cgonza16@student.aau.dk; nmarti16@student.aau.dk; las@civil.aau.dk; mta@civil.aau.dk
*   Correspondence: nmarti16@student.aau.dk
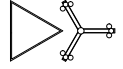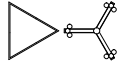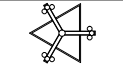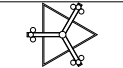‡   These authors contributed equally to this work.

Abstract: The TetraSpar floating foundation is a new design by Stiesdal Offshore Technologies that combines the advantages of existing floating offshore wind turbines. By industrializing the process of manufacturing, the TetraSpar concept allows the wind turbine to be mounted at quayside and further towed to the desired location. This paper focuses on the transport operation of the TetraSpar to accomplish an advance progress in its industrialization process. A test campaign is performed in the wave flume at Aalborg University to investigate the towing force. The towing tests were performed at different current speeds in absence of any other environmental forces. By considering different towing set ups, the results are compared with analytical and numerical models to evaluate the effects of their limitations and assumptions. Based on the results, the drag coefficient of the TetraSpar for constant flow is determined according to the current velocities implemented. Furthermore, the most feasible towing procedure is determined.

Keywords: Towing; FOWT; Drag coefficient, Draft, current velocity.

1. Introduction

Offshore wind energy has become an attractive option within the renewable energy market. The depth limitations of the traditional fixed foundations are leading to the evolution of the technology in this field. In so, different types of floating offshore wind turbines (FOWTs) are being developed in the industry, such as the TetraSpar floating foundation [1]. It is composed of a floater and a counterweight (CW), which is ballasted during the installation to reach an equilibrium and stable position. In this paper, it is intended to investigate the transportation of the TetraSpar system when it is being towed out to site. For this purpose, four different configurations are studied with the aim of determining the one that presents less resistance force. The notation used throughout this work is presented in Table 1, where a top view of the different configuration is also presented. Note that the current direction goes from right to left. Both A configurations stand for the CW being placed behind the structure when being towed. The difference between A_1 and A_2 is that the latest one is rotated 180º with respect the towing direction, although the CW remains in the same position. On the other hand, B configurations stand for the CW being placed under the TetraSpar, and again, B_2 corresponds to the system being rotated 180º. The authors emphasize the importance of knowing the distinct notations employed for each configuration. A 1:60 Froude scale model of the TetraSpar is used during the test campaign, based on [2]. In conjunction with the experiment, an analytical and numerical analysis of the towing is conducted to investigate the influence of their assumptions and limitations.

Table 1. Towing configurations.

Configuration	Analytical	Experimental	Numerical
	A	A_1	A_1
		A_2	—
	B	B_1	—
		B_2	—

2. Materials and Methods

2.1. TetraSpar structure

The TetraSpar floating offshore foundation is comprised of two distinguishable parts, namely the Tetraspar and the counterweight. The TetraSpar, or floater, is made up of an assembly of several cylinders, as seen in Figure 1. Three sets of tanks are connected to a central column through three radial tubes and three diagonal tubes at the same time. On the central column, a transition piece is mounted so the tower can be installed. A lumped mass is placed on top of the tower to simulate the Nacelle and the blades inertia. The second piece, the CW, is attached to the mid set of tanks, called fairlead, by means of 6 chains. During the transportation, the CW is floating with the design draft, and its position will depend on the configuration being studied. The analytical and numerical analysis are conducted considering the geometry and properties of the scaled model. Further details regarding the geometry can be find in [3].
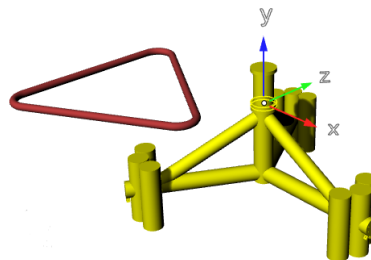
Figure 1. 3D render of the TetraSpar model in A_1 configuration.

2.2. Towing procedure and structure draft

The reduction of the installation time is achieved by attaching the CW to the structure in harbour. During transportation, chains will not be in tension so there will not be any interaction between floater and CW. Regardless of the chosen configuration, the CW will contain some initial ballast before the transport. The purpose of it, is to reduce the ballasting time at the final location. However, this fact will increase the CW draft and consequently the total resistance force. To find a compromise between ballasting time at site and resistance force, an optimal CW draft is selected among the ones presented in Figure 2.
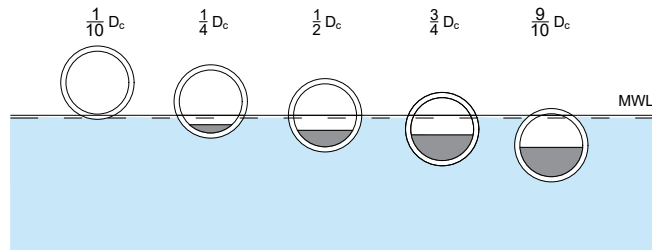
Figure 2. Different counterweights drafts used in the analysis.

The CW drafts are presented as a function of the outer diameter of the cylinders that form the CW, being D_c equal to 0.5 m. In the absence of initial ballast the CW draft is around $1/10D_c$. The maximum CW draft before sinking is approximately $1/9D_c$. By using Archimedes principle it is concluded that the optimal CW draft is $1/2Dc$. For the calculations it is assumed that the CW is completely hollow with a thickness of 1×10^{-5} m. The ballast used is concrete with density, $\rho = 2400\frac{Kg}{m^3}$, and the material of the CW is PVC with density $\rho = 1400\frac{Kg}{m^3}$. The results are presented in Table 2, which shows the draft of the model for both configurations depending on the volume of ballast used in the CW before transport. The structure drafts used in the analytical and numerical approaches are marked in red. They seem to have the best balance between volume of concrete and the ballasting time after transport.

Table 2. Drafts depending on the volume of initial ballast in the CW. Model scale values.

Volume of concrete [m^3]	A configuration draft [m]		B configuration draft [m]
	CW	Floater	Floater and CW
0	1/10 D_c	0.161	0.138
5×10^{-4}	1/4 D_c	0.161	0.143
12×10^{-4}	1/2 D_c	0.161	0.150
23×10^{-4}	3/4 D_c	0.161	0.155
28×10^{-4}	9/10 D_c	0.161	0.159

2.3. General Assumptions and Limitations

The investigation is performed in still water, thus it is assumed that there are no wave forces, nor wind forces acting on the structure. Since the experiment is not performed in a real towing tank, the resistance force is calculated by keeping the structure still and generating steady current against it. Besides the mentioned simplifications, it is expected that the best configuration under these assumptions will be also the most favourable for the case when all the environmental forces are taken into account. To compute the towing force, the chains are neglected although it is acknowledged that they would induce some drag resistance.

2.4. Analytical

To compute the resistance force analytically, it is assumed that the structure is fixed and formed by a group of slender cylinders [4]. Therefore, the resistance force presented by the structure is analogous to the sum of the drag forces exerted by the current on each cylinder. The drag force in a fixed cylinder is defined in Eq. (1).

$$F_D = \frac{1}{2} \cdot \rho \cdot V^2 \cdot D \cdot C_d, \tag{1}$$

where F_D is the current force per unit cylinder length, ρ is the water density, V is the perpendicular velocity component, D is the diameter of the cylinder and C_d is the drag coefficient.

In reality the structure is not fixed and it may oscillate when the current is passing through it. Then inertia forces will be present too. Nevertheless, in many realistic situations the cylinder velocity is considerably smaller than the incident flow velocity. Therefore, the assumption of ignoring the inertia forces is accepted. [5]

2.4.1. Simplification of the structure

Due to the complexity of the geometry, the actual structure is substituted by a much simpler and equivalent one. An example of the simplification is shown in Figure. 4.
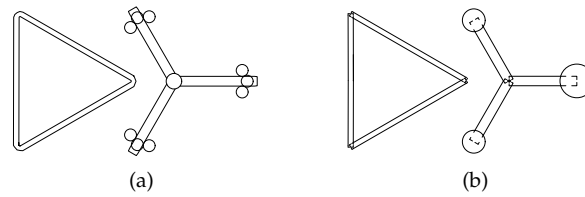

(a)   (b)

Figure 3. Plan view of structure simplification for A_1 configuration. **(a)** Original. **(b)** Simplified.

The simplification is done according to the following criteria:

- In the case of the buoyancy tanks, since they are adjacent in each "leg" and there are no gaps between them, it is assumed that each leg is formed by an unique cylinder with D_e equal to the width of projected area of the leg. As a compensation, the outer part of the radial beams is disregarded in the calculations.
- The simplified length of the radial beams spans from their nodes at the centre column connection to the centre of the simplified cylinders used for the buoyancy tanks. This is done as a compensation for the fact that the flow will be more complex in the joint vicinity and will lead to higher forces. Then, the top of the centre column is not included in the calculations.
- The CW is assumed to be formed by three cylinders of equal length.

2.4.2. Force Computation

As Eq. (1) is given per unit length, the structure is divided into several slices from the MWL until the bottom of the structure. See Figure 4a. At one specific slice, the force would be the sum of all forces acting on the components present in this slice. Then the total force acting on the structure is the sum of all forces. The projected area of the structure onto a vertical plane perpendicular to the flow direction is considered for the calculations. See Figure 4b.
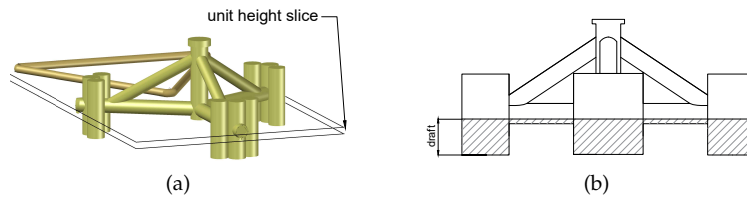

(a)   (b)

Figure 4. A_1 configuration. **(a)** 3D view of the original structure. **(b)** Projected area of the simplified structure.

The hatched area in Figure 4b represents the wetted part of the structure. In the projection, there are some parts of the structure hidden by others that need to be included in the force computation. Note that for the cylinders that are not vertical, an equivalent diameter must be used in Eq. (1) instead of D. This equivalent diameter will depend on the member orientation with respect to the vertical plane of the projection.

The force is calculated for the three different velocities given in Table 3. The theoretical value of the drag coefficient, C_d, is calculated based on Reynolds number, *Re*. The characteristic length chosen to determine *Re*, is the largest diameter of the members in the simplified structure. *Re* for the three velocities considered is in the range of $5K < Re < 200K$ and so $C_d \approx 1$. [5]

Table 3. Maximum velocities of each current profile according to the pump frequency.

Pump Frequency [Hz]	Max Velocity [m/s]
30	0.19
40	0.31
50	0.42

2.5. Experiment

Figure 6 presents the four towing configurations investigated during the test campaign. The triangular objects present in the counterweight are floats that were used to give buoyancy to the CW, since during the campaign it was not floating by itself. Figure 5 shows the experiment set-up in B_2 configuration at the hydraulic laboratory at Aalborg University. The three other configurations have the same set-up with the difference that they are placed according to Figure 6.

The wave flume is 9.82 m x 1.50 m x 1.50 m (length x width x height). To resemble the towing line, a steel wire is used. One of its ends is connected to the centre of the upper flange of the transition piece while the other is attached to a fixed horizontal bar. Between the transition piece and the steel wire, a load cell is placed to measure the force exerted by the current on the structure.

To avoid rotations or contact between the structure and the flume walls, two elastic bands with very low stiffness were attached to the transition piece at the same point as the steel wire. The ends of these bands were fixed to the flume sides having the same angle with the walls. The current velocity is generated by an hydraulic pump that was set to three different frequencies in each test, being 30, 40 and 50 Hz. The water depth, d remained unchanged for every test and it is set to $d = 0.5$ m. To measure the undisturbed current velocity a propeller is placed right before the structure as it is seen in Figure.5. The propeller measured the velocities at different heights to determine the current profile as a function of depth. Table 3 shows the max velocities of each current profile that are used in the analytical and numerical solution.
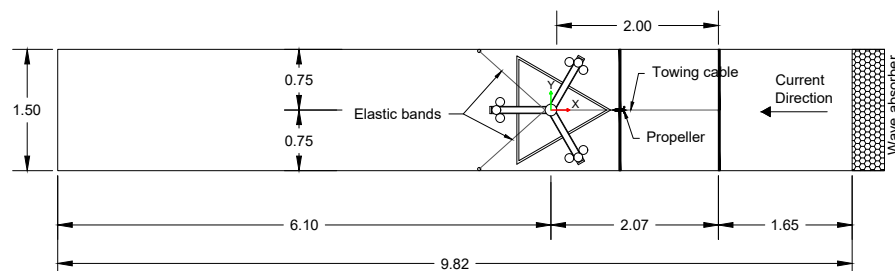

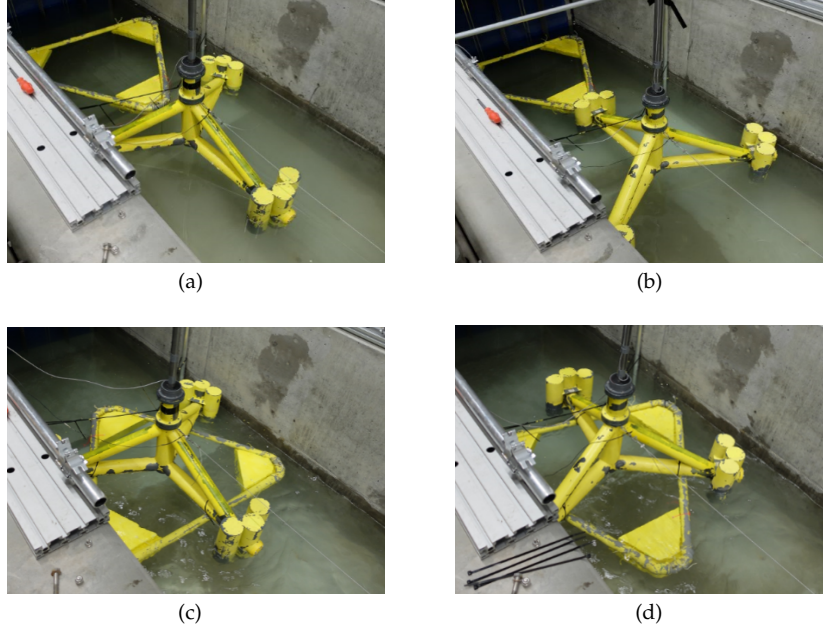**Figure 5.** Plan view of the experiment set-up for B_2 configuration.

Figure 6. Towing test configurations.**(a)** A_1. **(b)** A_2. **(c)** B_1. **(d)** B_2.

2.6. Counterweight buoyancy

The design of the floats that give buoyancy to the CW is shown in Figure 7. The material used to design the floats of the CW is expanded polystyrene, with density $\rho = 20 \frac{Kg}{m^3}$. It is seen that they increase the CW draft. In order to make the experiment results comparable with both analytical and numerical, the floats are designed so that the CW draft in the experiment is equivalent to the optimal one chosen in Table 2.
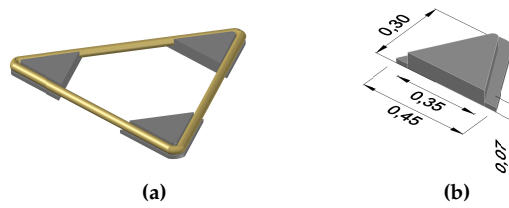

Figure 7. Floats used in the CW. **(a)** 3D view. **(b)** Dimensions in meters.

Figure 8 represents the relation between both experimental draft (left) and optimal draft (right). The hatched area represents the floats and the grey area the concrete used as ballast. Both have the same ratio between draft and height of projected area. The increment of draft at the corners of the CW due to the floats is counterbalanced with the lower draft of the CW parts that are not in direct contact with the floats.
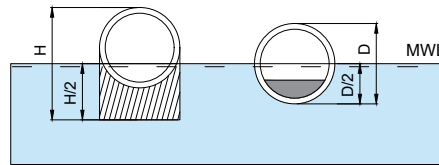
Figure 8. Relation between experiment draft (left) and optimal draft (right).

2.7. Numerical

Based on analytical and experimental investigations, both *A* configurations have presented the lowest resistance force. Nevertheless, among them, A_1 appears to be the best option because its arrangement requires less length of the chains. Therefore, the analysis is performed only to A_1 configuration. The governing equations used in the solution are the so called Reynolds-averaged Navier Stokes (RANS) that represent transport equations for the mean flow quantities , with all the scales of turbulence being modelled. The turbulence model used is the Realizable $k - \epsilon$, which focuses in the mechanisms that affect the turbulent kinetic energy [6]. Therefore, the model requires two additional transport equations to describe the turbulence of the flow, one for the kinetic energy, *k*, and the other for the rate of dissipation of turbulence energy, ϵ. The model also adopts the Boussinesq hypothesis which assumes the turbulent viscosity, μ_t, to be an isotropic scalar quantity.

The flow is assumed to be steady and uniform. Likewise the analytical and the experiment analysis, the drag force is computed for the three different flow velocities given in Table. 3.

2.7.1. Boundary conditions

As it is seen in Figure 9, the flow velocity, *V* , in the inlet boundary is steady and uniform over the entire boundary. Only the atmospheric pressure,P_0 , being 101325 Pa, is applied to the outlet boundary. The walls of the structure are modelled as smooth with non-slip condition, while the walls for the outer boundary of the set-up are modelled with slip-conditions. The outlet flow velocity equals the inlet, since the boundaries are far away from the flow disturbance region.
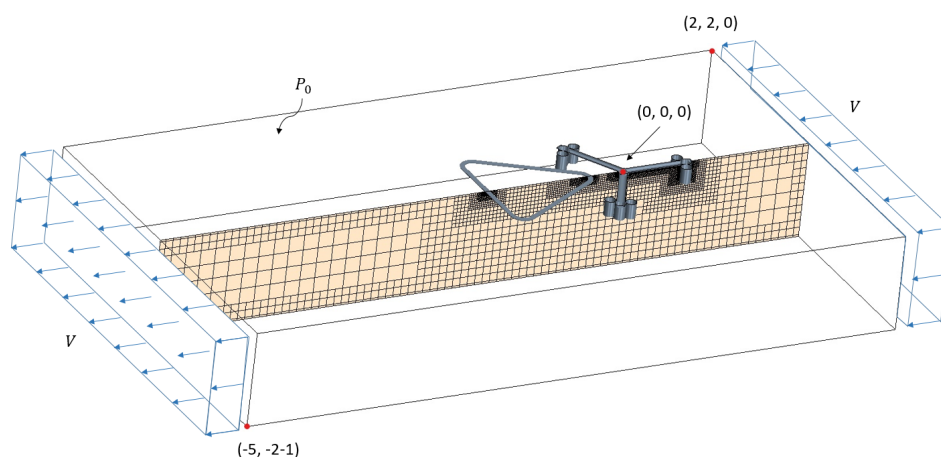

Figure 9. Boundary conditions in the CFD analysis of A_1 configuration.

2.7.2. Force computation

The drag force is calculated for the floater and CW separately, being the total one the sum of both. A mesh dependence analysis is performed for the case with current velocity, $v = 0.42 \ m/s$. As seen in Table 4, the output gives that the forces in both floater and CW converge with around 1% of difference when the number of cells is increased from 3M of cells to 9M, meaning that the amount of chosen cells does not compromise the accuracy of the results. Figure 9 shows how the mesh is refined in the vicinity of the structure.

Table 4. Results from mesh dependency analysis. $V = 0.42 \ m/s$.

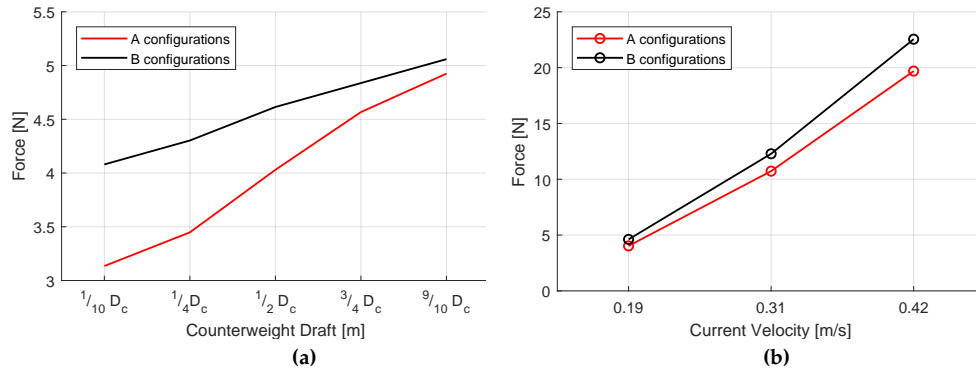| Cells	Force floater [N]	Force CW [N]	Total force [N]	Change [%]
680495	6.77	1.06	7.83	—
2977882	6.96	1.33	8.29	5.87
8958062	6.95	1.23	8.18	-1.33

3. Results

3.1. Analytical

Figure 10. Analytical forces. **(a)** For arbitrary velocity and C_d. **(b)** For CW draft $= \frac{1}{2}D_c$ and $C_d = 1$.

The main focus in Figure 10a is to investigate the variation of the analytical force depending on the counterweight draft. Note that the velocity and drag coefficient used are arbitrary values. It can be seen that the force in both configurations converges as the CW draft increases. The variation in *B* configurations is not as pronounced as for *A* configurations, which suggests that the influence of the CW draft is determinant in *A* configurations.

In B configurations, the fact that the CW is placed below the floater, reduces the draft of the whole system. This is due to the increase of the buoyant force when the CW is pushed down, which tends to force the structure back upwards. In spite of the decrease of draft in B configurations, the total force is still larger in B than in A for all the cases studied.

Figure 10b represents the analytical forces for the three current velocities determined during the test campaign. Again the drag Force in *B* is larger than in *A*, being the difference of around 13%. Thus the analytical solution suggests that the best configuration for the transportation regarding the drag force is any of the *A* configurations, with the CW placed behind the floater.

3.2. Experimental

The experimental results are presented in Figure 11. Forces in *B* are around 30% larger than in *A*. While in the analytical solution, the differences between *A* and *B* are only 13%. In the same way as for the analytical results, the variation of the force due to the change in flow velocity can be considered as linear. There is a good match between A_1 and A_2, being the values almost equal. On the other hand, the results for B_1 and B_2 are less similar when the flow is becoming more turbulent.

During the campaign it was observed that some parts of the CW were slightly more submerged. This fact was leading to a less accuracy in the results. Unlike in A_1 and A_2, where the CW is not in contact with the floater, for B_1 and B_2 the total projected area of both floater and CW is altered by this error. Furthermore the flow velocity facing the CW for A_1 and A_2 configurations is considerably reduced by the presence of the floater so the contribution of the CW to the force is not as important in this cases. Finally the more turbulent is the flow the more uncertainty is present, so it also explains the differences between *B*1 and *B*2 configurations. As a final conclusion, in agreement with the analytical results, the best configuration to transport the counterweight would be either A_1 or A_2 configurations.
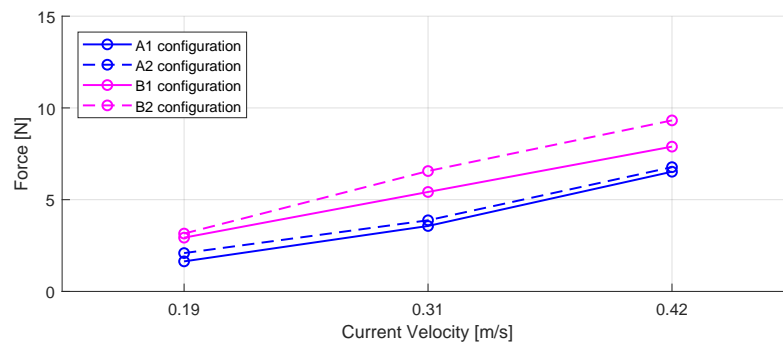

Figure 11. Experimental forces obtained for the different configurations.

3.3. Numerical

The numerical output from the Computational Fluid Dynamic (CFD) analysis of A_1 configuration is shown in Table 5. The force contribution of the CW and the floater are obtained for the three different current speed employed.

Table 5. Numerical forces derived from the CFD analysis.

Velocity [m/s]	Force CW [N]	Force Floater [N]	Total Force [N]
0.19	0.27	1.35	1.62
0.31	0.67	3.58	4.25
0.42	1.23	6.95	8.18

3.4. Comparison

Figure 12 presents the comparison of the forces from the three approaches for A_1 configuration. Moreover, it shows how the real drag coefficient,C_d , is determined.

Looking at Figure 12a it is seen that the experimental and numerical results for the forces have a good correlation between each other, specially at low velocities. The numerical is slightly more conservative than the experiment results. One possible explanation is the assumptions made to the current profile in the numerical solution, where the effect of the walls or seabed is not included. On the other hand, the analytical solution obtained with the theoretical drag coefficient, is rather large compared to numerical and experimental. Since the trend in the three curves is linear with very similar slope, it suggests that a smaller C_d must be used. The optimal drag coefficient is determined based on the numerical solution. The reasons why the experimental solution is not used to calibrate C_d are:

- The inclusion of the floats to the CW in the experiment alters considerably the geometry of the structure, consequently C_d would not be valid for the real scenario.
- The force given in the experiment is just the total one. While the analytical and numerical solutions give the drag force for both floater and CW separately. See Figure 12c and Figure 12d.
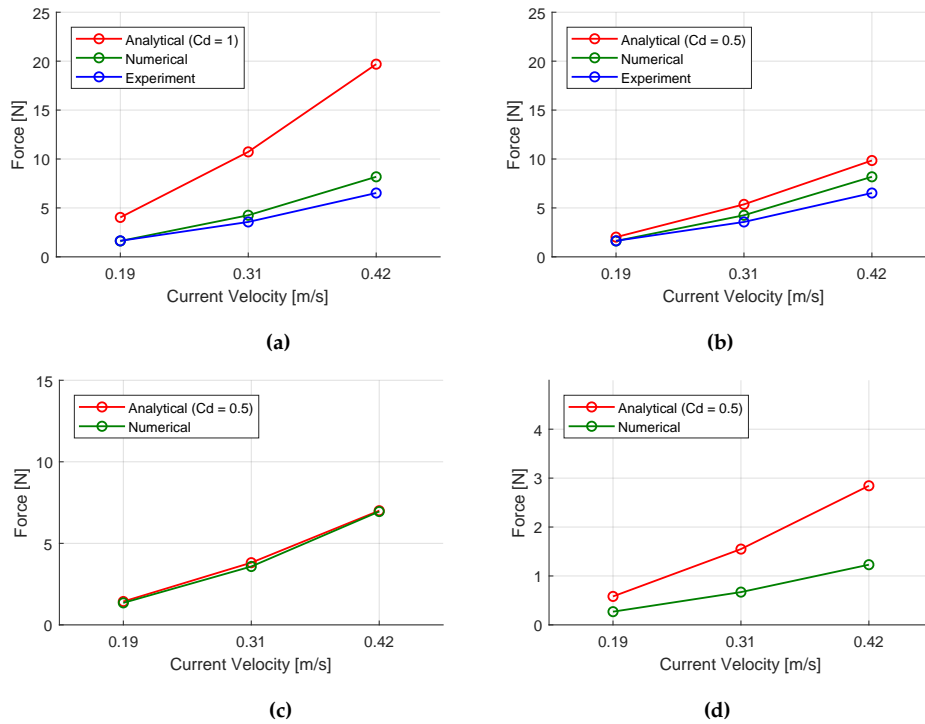

Figure 12. Forces in A_1 configuration. **(a)**Total force and $C_d = 1$. **(b)** Total force and $C_d = 0.5$ **(c)** Floater force. **(d)** Counterweight Force.

By considering only the force in the floater, shown in Figure 12c, if a drag coefficient of $C_d = 0.5$ is used in the analytical solution, the forces from both approaches are practically identical. However this is not the case for the forces acting in the CW. See Figure 12d. This fact suggests that the force on the CW is not predicted well with the analytical approach.

As a final comparison, Figure 12b presents the total force from the three approaches using $C_d = 0.5$ in the analytical solution. Note that the red and green lines are the result of adding the forces from Figures 12c and 12d. Besides the error induced by the above mentioned assumption in the CW contribution, there is a good agreement with the analytical solution if a drag coefficient $C_d = 0.5$ is used.

In order to verify that the new drag coefficient is correct, the forces in B configurations are also compared. One should expect the results to be also very similar between the different approaches. The comparison is presented in Figure 13. In Figure 13a, it can be seen the notable differences between using the theoretical C_d and the calibrated one. By looking at 13b it is seen that unlike in A configurations, the analytical force is in very good agreement with the experimental force for B configurations.
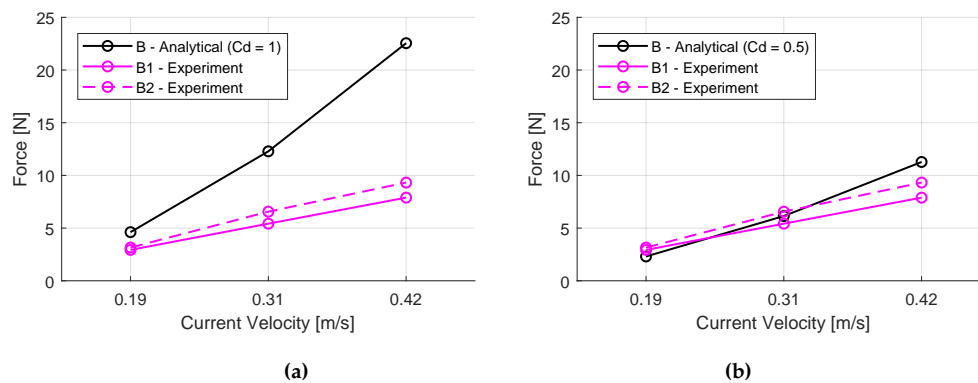

Figure 13. Comparison Experiment and Analytical $C_d = 0.5$. **(a)** *A* configurations. **(b)** *B* confugurations.

3.5. Full scale values

In the present work, forces have been presented in model scale. Effort is here made to provide the reader an insight into the full scale resultant forces. The dominant forces play an important role when it comes to pick a proper scaling law. Froude number typically deals with the relationship between gravity and inertial forces, in other words, it will give a proper scaling of the surface waves. On the other hand, Reynolds number is more closely related to viscous drag, particularly in laminar flow. In this paper, the dominant forces are the viscous forces due to the disregarding of the waves. However, in real life the effects of the drag forces would be relatively weak compared to the effect of gravitational free surface waves. Besides, the R_e found for the three velocity profiles generated show that the flow is turbulent, and as the Reynolds scaling law presents difficulties to generate the model scale towing speed in laboratory experiments; it is deemed appropriate to use Froude scaling law. Table 6 shows the full scale values of the total towing force obtained for the different current velocity used within the analytical, experimental and numerical approaches for the A_1 configuration.

Table 6. Towing force values in full scale for A_1 configuration.

	Total Towing Force [kN]		
Velocity [m/s]	Analytical	Numerical	Experimental
1.47	434	350	354
2.4	1158	918	771
3.25	2128	1767	1410

4. Discussion and Conclusion

The analytical solution, together with the structure simplifications and the theoretical value of C_d, gives a good estimation of which configuration presents larger forces. Since the analytical results are rather conservative, it is clear that C_d must be calibrated based on either experimental or numerical approaches. By using the calibrated C_d, the analytical force is only in good agreement with the experimental results for B configurations. This fact ensures that in A configurations the flow is highly disturbed after passing through the floater. Therefore, it is proven that the analytical solution does not predict the forces accurately for A configurations.

The comparison between numerical and experimental results shows good correlation, which implies that the assumption of uniform flow and slip condition in the outer boundaries can be accepted. Based on the analytical and experimental results, it becomes apparent that the configurations where the CW is placed behind present less resistance force. Besides, given that the CW chains will be already anchored before towing, A_1 is found to be the most optimal configuration as its arrangement is less limited by the length of the chains itself and does not hinder the installation of the TetraSpar system. Further investigations should include the influence of the chains during the tow out, as well as some metocean conditions such as waves and wind forces.

Based on the presented work, the most optimal configuration is found to be A_1, corresponding to the CW placed behind the floater. Furthermore, favourable findings regarding this configuration shows that it reduces the towing force by 30%.

Author Contributions: The authors E.B.V , C.M.G and N.G.K.M contributed equally to this work. The paper is written as part of a master thesis at Aalborg University. L.S contributed in regards to the numerical work from inputs given by E.B.V , C.M.G and N.G.K.M. M.T.A contributed with helping on the project scope and important inputs.

Conflicts of Interest: The authors declare no conflict of interest.

Abbreviations

The following abbreviations are used in this manuscript:

CW	Counterweight
FOWT	Flouting Offshore Wind Turbine
CFD	Computational Fluid Dynamic

References

1. Henrik Stiesdal, Stiesdal Offshore Technologies **2017**.
2. C. Bak,F. Zahle, R. Bitsche, T. Kim, A. Yde, L.C. Henriksen, A. Natarajan, M.H. Hansen, DTU Wind Energy Report-I-0092 **2013**.
3. Eduardo Benitez Villaespesa, Cristino M. Gonzalez, Nils G.K. Martin, Transportation and Installation Of the TetraSpar Floating Offshore Wind Turbine **2018**.
4. Bruce R. Munson, Theodore H. Okiishi, Wade W. Huebsch, Alric P. Rothmayer, Fundamentals of Fluids Mechanics **2007**.
5. J.M.J. Journée and W.W. Massie, Offshore Hydromechanics, First Edition; Delft University of Technology **2001**
6. Fluent Inc. 2001, FLUENT 6.0 Users Guide, NH, USA. **2001**.

Sample Availability: Samples of the compounds ...... are available from the authors.

Part III

Paper B - Investigation of the Dynamic Response of the TetraSpar Floating Offshore Wind Turbine During Installation

Article

Investigation of the Dynamic Response of the TetraSpar Floating Wind Turbine During Installation

Eduardo Benitez Villaespesa [1,‡], Cristino M. Gonzalez [1,‡], Nils G.K. Martin [1,‡,*] and Morten T. Andersen[1]

[1] Department of Civil Engineering, Aalborg University, Aalborg, Denmark; ebenit16@student.aau.dk; cgonza16@student.aau.dk; nmarti16@student.aau.dk; mta@civil.aau.dk

[*] Correspondence: nmarti16@student.aau.dk

[‡] These authors contributed equally to this work.

Abstract: The TetraSpar floating offshore wind turbine design by Stiesdal is a new, innovative design which aims to industrialize floating foundations by simplifying manufacturing and installation processes. The structure is towed out from the harbour in a semi-submersible configuration and once on site it is set into a spar configuration by ballasting a counterweight attached to the foundation. The purpose of this paper is to investigate the behaviour of the foundation during its installation process by the help of a test campaign done at Aalborg University wave basin and numerical models. The responses are compared between the physical model and simulation results in order to validate the numerical model and be able to implement its use for further studies in the same field. As a result, the Response Amplitude Operators of motions and the natural frequencies of the TetraSpar structure show the range in which it could be installed without compromising its safety.

1. Introduction

Numerous types of floating offshore wind turbines (FOWTs) can be found nowadays in the renewable energy market. With this sector thriving on the reduction of the levelised cost of energy (LCOE), the TetraSpar structure is a potential reference for success in its industry. The expected cost of applying this technology is 4.2 m€/MW, making of the TetraSpar the most economically advantageous FOWT. On top of that, its versatility allows it to be installed at water depths from 10 m to 1000 m, which will enhance the worldwide operational area of the wind power production.

In the presented work, effort is made to better understand the installation responses of the TetraSpar system. The installation is comprised of four different stages, as seen in Figure 1. In this paper special attention is paid to hook-up and spar configurations. Hook-up configuration corresponds to the mooring of the floater at the designed location. On the other hand, spar configuration represents the final position of the structure once the counterweight (CW) is ballasted. The design process of a floating offshore wind turbine demands high quality computer simulations due to its complex dynamic response. The amount of degrees of freedom involved and the wide ranging ocean conditions are the main reasons for the development of such numerical models. Several sea states are implemented to get some initial results of simulated dynamic responses of the TetraSpar during the installation process.

The main aim is to find the natural frequencies and the response amplitude operators (RAOs) of three rigid body modes of motion for the TetraSpar structure within an acceptable range during installation. It is intended to demonstrate the technical feasibility of this offshore floating wind turbine by showing that, through a proper design, the natural frequencies of the floating support platform
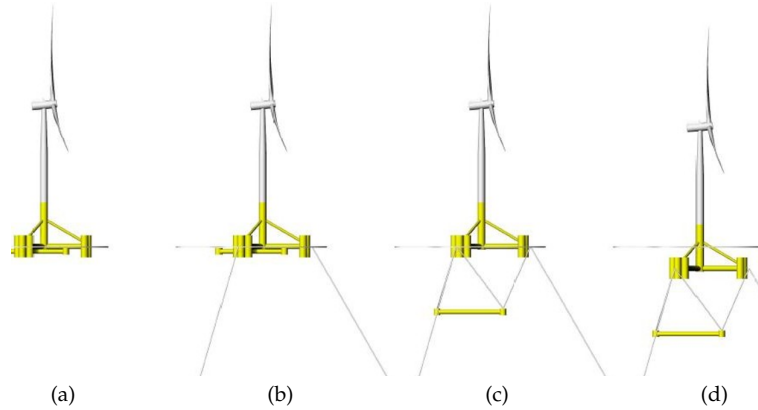
(a)   (b)   (c)   (d)

Figure 1. TetraSpar FOWT installation concept. **(a)** Floating configuration **(b)** Hook-up configuration **(c)** Ballasting **(d)** Spar configuration [2]

can be placed where there is little energy in the wave spectrum to ensure that the overall dynamic response is minimized. The TetraSpar project is divided in four stages: concept, design, scaled model and pilot structure. This paper occurs within a Technology Readiness Level 6 (TRL), sustaining the line of previous investigations made with a 1:60 scale model of the structure. The results of these studies are presented in [6], [7], [8], [11].

2. Materials and Methods

2.1. Structural Model

This paper uses as a starting point a 1:60 scale model. In the following sections all properties are given in 1:60 following Froude scaling law. The outputs will be however presented in full scale.

Figure 2 shows the position of the global coordinate system with the origin located at MWL. The floater motion is described by translational and rotational degrees of freedom (DOF). These are characterized by surge, sway and heave displacements in the $x-$, $y-$ and $z-$directions. Rotations are defined by roll, pitch and yaw about $x-$, $y-$ and $z-$axes.
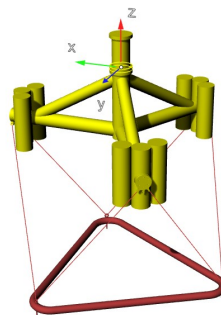
2.1.1. TetraSpar Floater

Figure 2. 3D render of the TetraSpar model.

The floating offshore foundation is divided in two substructures, as shown in Figure 2. The floater, in yellow, is composed of a central column joint to three sets of tanks. The central column is connected to three radial tubes and three diagonal tubes. A connection plate and a transition piece are installed on top of the central column. It is used as the interface between the floater and the wind turbine tower. Finally the floater is balanced by a CW, shown in red in Figure 2, and attached to the fairlead by six chains. The properties in hook-up and spar configurations are shown in Table 1 and in Figures 3a, 3b.

Table 1. Hook-up and spar configuration properties.

Hook-up configuration	Value	Units
Floater dry mass	16.23	[kg]
Draft, d_1	0.160	[m]
Volume displaced	0.0161	[m^3]
Vertical centre of gravity from MWL	0.077	[m]
Spar configuration		
CW dry mass	44.69	[kg]
CW chains dry mass per meter	0.185	[kg]
Draft, d_2	0.455	[m]
Length of the transition piece	0.200	[m]
Volume displaced by floater	0.0512	[m^3]
Volume displaced by CW	0.00745	[m^3]
Vertical CG of floater from MWL	-1.017	[m]

2.1.2. Wind Turbine Model

This paper is using the DTU 10 MW Reference Wind Turbine, for which the description is given in [5]. The actual model scale wind turbine used during the test campaign and for the numerical model is presented in [1].

2.1.3. Mooring system

The mooring system designed considers taut compliant mooring lines, which present a slight difference regarding its setting. In spar configuration the angle, α_2, between the mooring line at the fairlead and the vertical line reads 60°, as seen in Figure 3b. On the other hand, in hook-up configuration the angle, α_1, is equal to 54°, as seen in Figure 3a. The dynamic responses of mooring lines provide the necessary restoring load to keep the floating wind turbine in its proper position. The main properties included in numerical models are tuned according to [8] and summarized in Table 2.

Table 2. Properties of the Mooring system implemented in FAST.

Dimension	Value	Units
Line diameter	0.01	[m]
Mass per unit length	0.04	[kg]
Axial stiffness	38	[N]
Unstretched line length	0.747 - 1.41	[m]

Previous to the test campaign, the axial stiffness is calculated under static condition by applying a known force and measuring the mooring line elongation. Moreover, while the fixed coordinate of the mooring lines are kept unchanged for both configurations, the position of the fairlead are adjusted to account for the lower draft of the hook-up stage. The length of the cables increase accordingly, leading to a longer unstretched line length, which enlarges from 0.747 to 1.41 m.

2.2. Test program and procedure

Figures 3a and 3b presents the sign conventions and the basin set-up for hook-up and spar configurations.
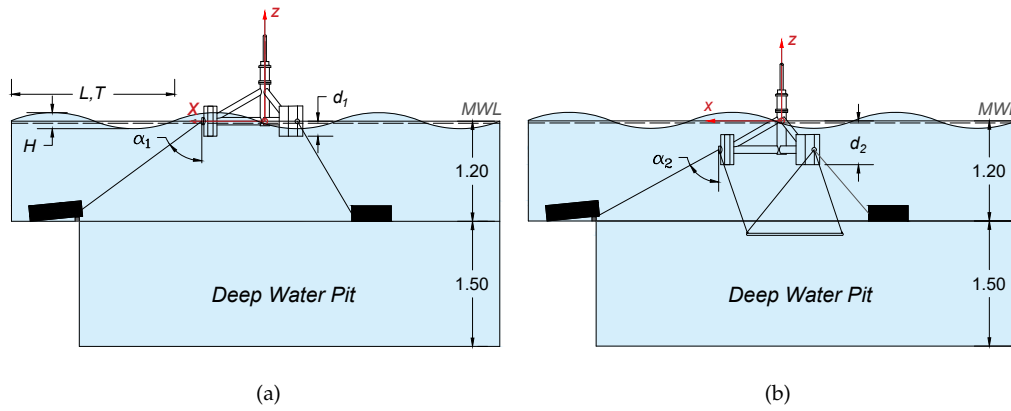
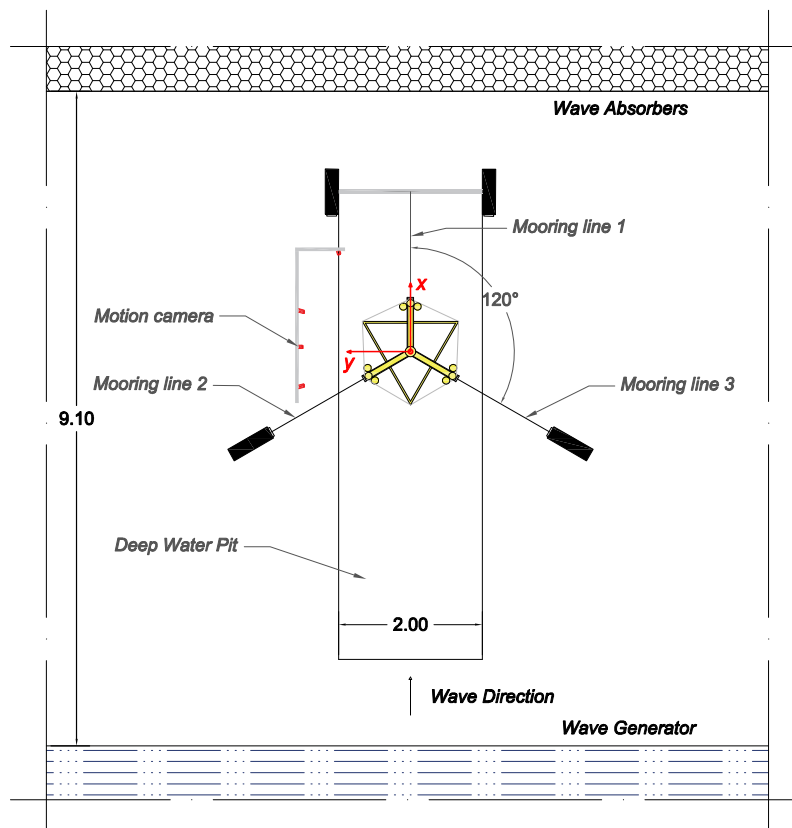**Figure 3.** Basin set up. **(a)** Hook-up configuration. **(b)** Spar configuration.

Figure 4. Wave basin experimental set-up: plan view.

In Figure 4 a plan view of the wave basin is shown. The wave basin is 14.6 m x 19.3 m x 1.5 m (length x width x depth). A deep water pit of 6.5 m x 2.0 m is used with a depth of 1.5 m so that a deep water condition is fulfilled during testing. The TetraSpar floater is placed above the deep water pit and is moored by using three mooring lines at a 120° angle. Long-stroke segmented piston wave generator are used to generate waves tested during the test campaign. The motion of the structure is measured by using four OptiTrack Flex cameras and five reflective markers. These are placed in random positions which provide asymmetrical markers for the cameras to measure.

2.2.1. Free oscillation tests

Free oscillations tests, also called decay tests, are performed to extract the dynamic behaviour of the excited structure by identifying parameters such as the natural frequency and the linear and quadratic damping. For the TetraSpar test campaign particular focus is given to the following DOF: pitch, heave, roll and surge. For each DOF several decay tests are performed as the quality of the test is crucial to the extraction of the dynamic behaviour.

A Butterworth-filter with a cut-off at 1 Hz is applied to the filtered data to reduce the presence of high-frequency noise. Then the signal is converted from time-domain to frequency-domain to obtain the natural frequencies. Finally, the damping ratio, ζ, is determined from the logarithmic decrement, δ, as shown in eq. (1).

$$\delta = \frac{1}{n} \log \frac{A_0}{A_n} \rightarrow \zeta = \frac{\frac{\delta}{2\pi}}{\sqrt{1 + \left(\frac{\delta}{2\pi}\right)^2}}, \tag{1}$$

where A_0 is the first amplitude of the filtered signal and A_n $n^{th}-$ amplitude of the filtered signal. These are plotted with regards to the average cycle amplitude and used in calibration of numerical models. The cycle amplitude is obtained by taking the mean of the two successive peak amplitudes used in determining that specific damping ratio. Example of these damping ratios obtained can be seen in Figure 9.

2.2.2. Regular wave tests

Regular wave tests are performed following the characteristic sea states of the Norwegian Continental Shelf defined in [4]. The wave climate is taken at Utsira, in Norway with a mean water depth of 200 meters and a a distance of 21 km away from the shore. The sea states characteristic parameters are shown in Table 3. During the test campaign only the most extreme sea states are tested, corresponding to sea states 7 to 10. Thus the rest of the sea states are investigated with the help of numerical models as these are the most representative sea states of the wave climate during the installation process. The regular waves are generated with a zero degree heading.

Table 3. Characteristic sea states on the Norwegian Continental Shelf. [4]

		Sea State									
		1	2	3	4	5	6	7	8	9	10
Full scale	H_s **[m]**	0.50	1.25	1.75	2.25	2.75	3.25	3.75	4.25	4.75	5.25
	T_p **[s]**	7.13	7.44	7.69	8.04	8.39	8.80	9.01	9.09	9.51	9.96
Model scale	H_s **[m]**	0.008	0.021	0.029	0.038	0.046	0.054	0.063	0.070	0.079	0.088
	T_p **[s]**	0.92	0.96	0.99	1.04	1.08	1.14	1.16	1.17	1.23	1.28

The RAOs of the TetraSpar motion are obtained from the regular wave tests, which is the ratio between the response amplitude and the wave amplitude, and it is expressed as

$$RAO = \frac{Y_A}{X_A},\tag{2}$$

where Y_A is the measured maxima and minima from the response signal and X_A the wave amplitude.

A steady state response needs to be considered for the response signal. Thus, as shown in Figure 5, the selected values for the study corresponds approximately to 15 oscillations after the transient response has died out. Taking [8] as reference, the experimental wave heights are fulfilled within a confident range which means that a harmonic signal can be assumed. The wave amplitude is then determined as $H_s/2$.
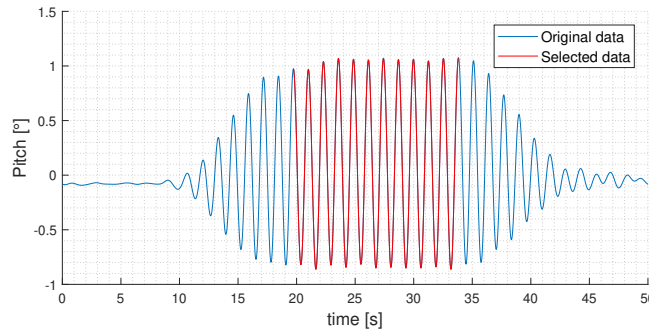
Figure 5. Regular wave data used to perform the RAOs.

2.3. Numerical

The FAST wind turbine design code used in this paper, developed and maintained by the National Renewable Energy Laboratory (NREL) [10], is a nonlinear time domain simulation tool. It is capable of modelling the coupled aero-hydro-servo-elastic response of floating offshore systems for a variety of wind turbine, support platform, and mooring system configurations. In other words, FAST operates with different modules that can be interfaced to analyse the dynamic response from combined wind and wave loading. In this paper only ElastoDyn, HydroDyn and MoorDyn modules are considered. Regarding the support platform kinematics and kinetics, it is assumed that the floating support platform is well represented as a six DOF rigid body with three small rotational displacements. The support platform together with the transition piece are considered to behave as a rigid body. Likewise, the centre of mass (CM) and centre of buoyancy (COB) of the support platform are assumed to lie along the longitudinal axis of the undeflected tower.

2.3.1. Hook-up and Spar configuration models

The focus of the numerical models developed are directed towards the implementation of an adequate prototype of the TetraSpar substructure. Consequently little time is spend on the turbine itself and few adjustments are then applied to the FAST model provided by [5]. For the 1:60 scaled wind turbine, the key properties conferred to each FAST model are shown in Table 1.

Hydrodynamics are included within FAST by incorporating a suitable combination of incident wave kinematics and hydrodynamic loading models. In linear hydrodynamics, the problem can be split into three separate and ordinary problems: one for radiation, one for diffraction, and one for

the incident undisturbed wave field. Due to linearity, the forces obtained in these problems can be subsequently added to give the total hydrodynamic forces, yielding Eq. (3).

$$\phi = \phi_i + \phi_r + \phi_d, \tag{3}$$

where each term stand for the incident, radiation and diffraction wave velocity potential respectively. Potential flow theory is used to model the floater within HydroDyn module by making use of WAMIT in a preprocessing step [9]. It computes the linear radiation and diffraction forces of the platform, as well as the volume of water that it displaces. The WAMIT output also provides the linear hydrostatic restoring matrix for the platform. WAMIT is a panel method solver based on a potential flow formulation of the flow field for analysing the interaction of plane progressive waves with one or multiple interacting offshore structures. Figure 6a shows the triangular 3D mesh of the hook-up configuration. Figure 6b shows the 3D mess developed in [7].

(a)   (b)
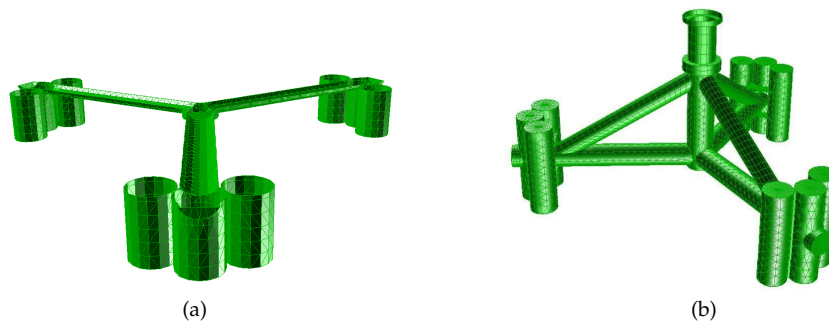
Figure 6. WAMIT input 3D mesh. **(a)** Hook-up configuration. **(b)** Spar configuration.[7]

2.3.2. Calibration

A preliminary test is performed in a zero displacement condition for the 6 DOFs studied. The aim is to calibrate the model to ensure an adequate initial equilibrium position. It can be said that the equilibrium condition is substantially achieved for the 6 DOFs. Less accuracy is reached for the pitch initial position in hook-up and spar configurations, showing a value of -0.18° and 0.12° respectively, which impacts are still considered negligible. The only tuning conducted in the hook-up configuration is focused on the axial and transverse drag coefficients of the floating platform members and the mooring lines respectively. An axial drag coefficient of 3.9 is applied to the bottom of all buoyancy tanks and central column. This value is computed by interpolating the original value of 7.8 tuned by DTU. Taking as reference [1], the transverse drag coefficient of the floater is set to 0.5 for the hook-up configuration. A value 2.0 is chosen for the spar configuration according to [11]. Furthermore, following the definition of the DTU HAWC2 model [7], a transverse drag coefficient of 1.0 is chosen for the mooring lines and CW.

FAST is yet not capable of modelling structures composed of multiple bodies that can move relative to each other. Because of this, for the spar configuration, floater and counterweight are modelled together as a single rigid body. In the previous section, it is noted that WAMIT provides a simulation model for the floater, but not for the CW. The volume displaced by the floater is then computed via WAMIT, while the CW is not taken into account. The volume displaced by the CW is calculated through the HydroDyn module, which models the whole substructure by using the full strip theory solution. Body weight is important for the pitch and roll restoring of deep-drafted floating platforms, such as the TetraSpar in its spar configuration. Therefore, it is necessary to add the contribution from the effects of the CW to the hydrostatic restoring stiffness matrix C_{ij} computed

by WAMIT. In this case, the non zero values are elements (4,4) and (5,5). It is set $C_{44} = C_{55} = $ -100.34 N m/rad, which adjustment stands for the mentioned roll and pitch restoring moments.

Once the model is calibrated, a range of decay tests are performed in order to compare damping properties and natural frequencies between the FAST model and the physical test model. The free decay tests are done by imposing an initial displacement (translation or rotation) to the structure in the direction of each of the 4 DOFs studied, allowing the model to freely oscillate until it returns to equilibrium. No incident waves nor wind are considered. The initial displacement applied are specified in the ElastoDyn module, setting the same values recorded during the test campaign in order to mimic the structure response.

3. Results

3.1. Free oscillation tests

Table 4 summarizes the natural frequencies of both simulated and experimental free decay tests for each platform DOF analyzed. Figures 7 and 8 show examples of the different DOFs decay tests and its corresponding power density function in the frequency domain.

Table 4. Comparison of the full scale hook-up and spar configuration natural frequencies.

DOF	Hook-up Frequency [Hz]			Spar Frequency [Hz]		
	Exp.	FAST	Error [%]	Exp.	FAST	Error [%]
Roll	0.055	0.056	2.3	0.035	0.035	0
Pitch	0.056	0.056	0	0.035	0.035	0.38
Surge	0.019	0.030	35.6	0.011	0.011	2.33
Heave	0.058	0.095	28.2	0.034	0.037	6.64

A very good agreement between numerical and experimental data can be seen in terms of natural pitch and roll frequencies. Tuning the pitch and roll inertia parameters led to an increase of the accuracy for both values. No surge decay test results nor natural frequencies were available to compare with FAST output for the hook-up configuration. As it can be seen in Figure 7b, in the pitch frequency domain plot there is a slight contribution from the surge DOF. This means that during the free decay test, another DOF was excited as well. Therefore, this value is used to couple with for the surge FAST free decay test. That is the reason why surge natural frequency differs about 35.6 % between the numerical model and the value obtained from the pitch decay test. This shows how difficult it is to excite only one DOF at a time during the experimental work. Additionally a large error is obtained for the FAST heave DOF. It can be explained by a poor quality of the free decay recordings, which makes it difficult to match the natural frequency.
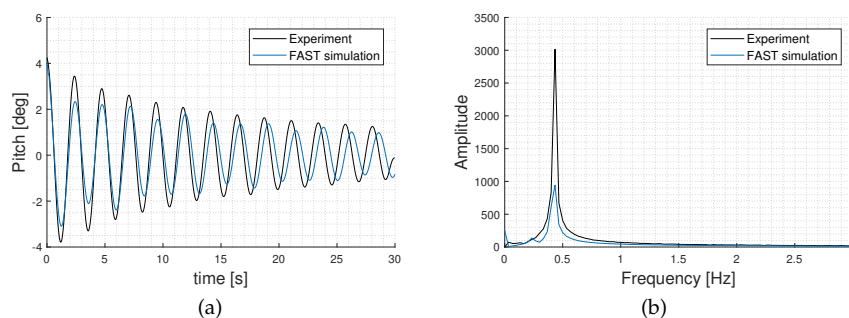

Figure 7. Pitch free oscillation test results for hook-up configuration. **(a)** Filtered data. **(b)** Structural response in the frequency domain.
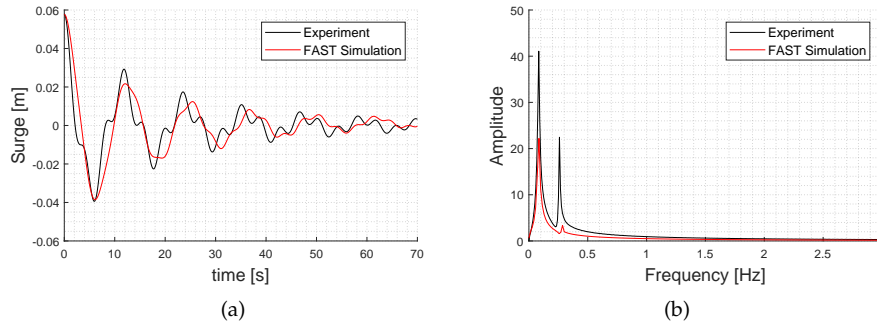
Figure 8. Surge free oscillation test results for spar configuration. **(a)** Filtered data. **(b)** Structural response in the frequency domain.

Figure 9 shows the average amplitude cycle every two successive peaks during the free decay tests. From a first observation, it seems that the the response of the structure in hook-up configuration is less damped than in the spar configuration. This is distinctively due to the fact that there is no CW to counteract the balancing movement.
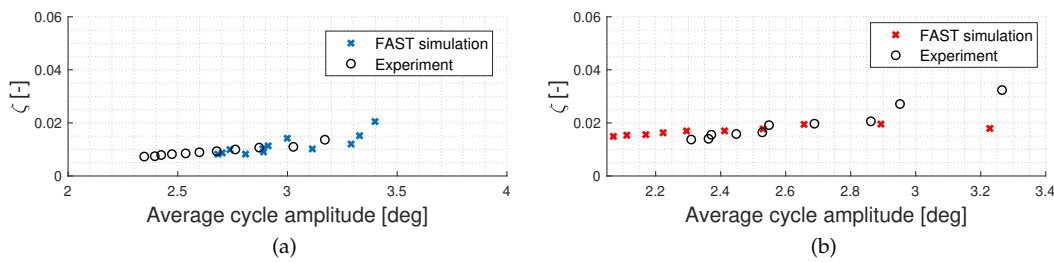

Figure 9. Damping ratio comparison. **(a)** Hook-up configuration. **(b)** Spar configuration.

3.2. Wave validation

The response of the calibrated FAST models are compared to wave basin model test data for the TetraSpar FOWT. The four sea state conditions shape different platform motion response. As example, the response to Sea state 7 for spar configuration is shown in Figure 10. They are deemed acceptable regarding that little difference is obtained between experimental and simulation results. The case considered to validate the response of FAST model against wave excitation only includes regular waves in absence of wind. This approach allows for an identification of discrepancies between test data and FAST simulations to further determine the RAOs.
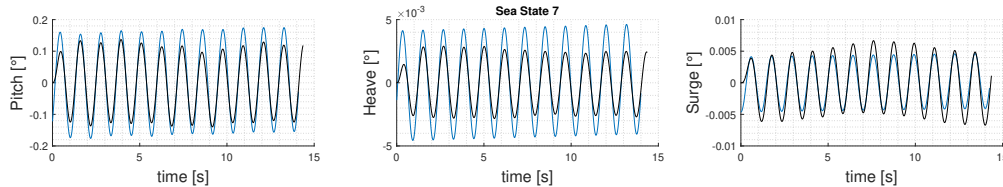
Figure 10. Structural response to regular waves in spar configuration. Blue signal stands for FAST while the black signal for the experimental response.

3.3. Dynamic response analysis : RAO
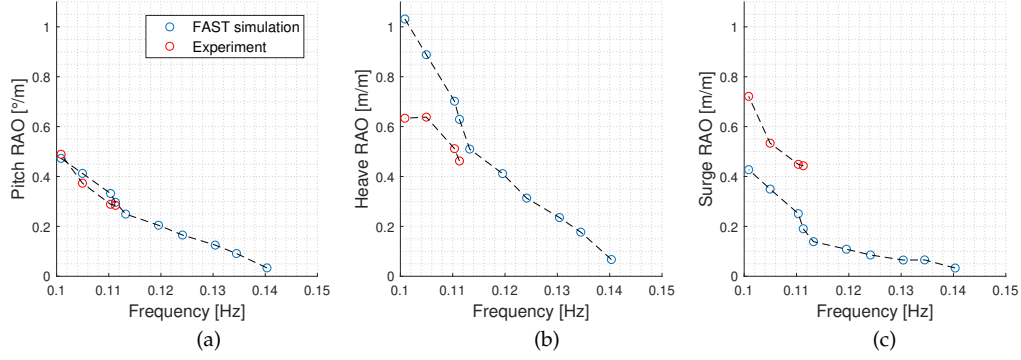
Figure 11. Experimental and FAST RAO results for hook-up configuration. **(a)** Pitch RAO. **(b)** Heave RAO. **(c)** Surge RAO.
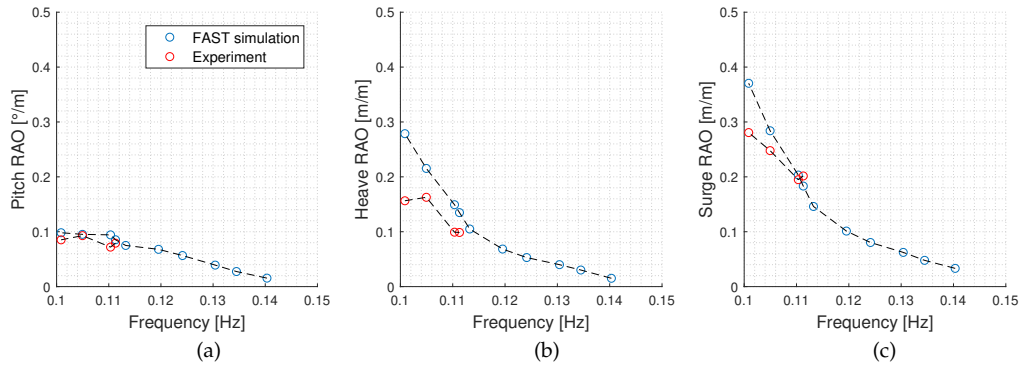

Figure 12. Experimental and FAST RAO results for spar configuration. **(a)** Pitch RAO. **(b)** Heave RAO. **(c)** Surge RAO.

The general response of the floater is determined by performing regular wave tests, as its harmonic behaviour is simpler to evaluate. The results from the RAO are shown in Figures 11 and 12, where the main focus is given to pitch, heave and surge. Fully coupled responses are observed for the pitch DOF in both configurations. In hook-up configuration, higher mismatches are observed in Figure 11b and 11c, even if the heave response seems to behave adequately for higher frequencies. Surge RAO seems to give a larger divergence, which is consistent with the results of numerical natural frequencies. The source of error could be explained by a low value of the unstretched length in the mooring lines. The unavailability of experimental surge decay tests in hook-up configuration hinders the possibility of getting more accurate results for this DOF. General good agreement is found for the spar configuration for the 3 DOFs. As with the heave free decay test, heave RAO presents less accuracy for smaller frequencies. It is observed that for higher frequencies, better compromise is found between experimental and numerical results. For sea states one to six it is expected to be in accordance with the general trend obtained with the numerical model.

4. Discussion and Conclusion

The structural characteristic parameters are calculated from a test campaign done at Aalborg University on a 1:60 scale model. Natural frequencies, periods and damping ratios are given for the reader to know where do these parameters stand with regard to the environmental conditions. The purpose is to know potentially feasible locations where the project planner would intend to install the TetraSpar. With this in mind, it should be performed an extensive climate analysis of the wind and waves at the site to ensure that the structure natural frequencies do not coincide with the wave spectrum. In Figure 13, an example of this kind of analysis is shown where time series of irregular waves are generated from WaveLab with a JonSwap spectrum of Sea State 1. As it can be observed, the natural frequencies for all the DOFs in both configurations meet a stability condition by standing aside from the wave energy spectrum.
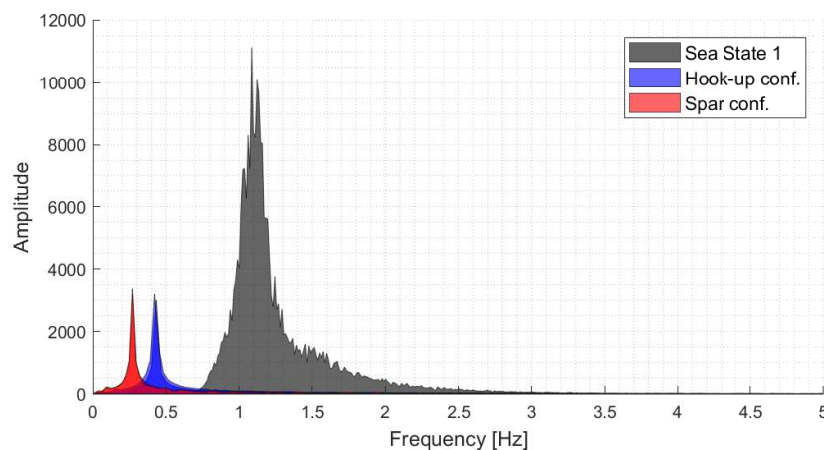
Figure 13. Wave spectrum for sea state 1 and corresponding Jonswap-spectrum. Natural frequencies are marked as dashed red and black vertical lines for each configuration respectively.

Regular waves RAOs of the TetraSpar motions defined by Eq. (2) are obtained for two different models: the scaled model tested in the basin and calibrated numerical models built with FAST from NREL. For these models, two installation configurations (hook-up and spar) are developed and studied. The results show smaller RAOs for waves with higher frequencies. This means that satisfactory findings have been accomplished for the response of the structure during installation, as it is required from the authorities to conduct the installation process under a calm water sea state condition.

A certain unreliability is observed in the hook-up configuration FAST model. It is encouraged to further investigate these differences between the model and the experiment that may well be because of errors in the calibration of the model, errors or inaccuracies in the experimental set up as well as lack of valid tests for some of the DOFs such as surge and yaw. Another source of error could be the scaling law used, which may lead to some inaccuracies in the final results.

In general, the responses are in a good agreement between the experiment and the simulation, particularly for the spar configuration. Moreover, both cases showed an appropriate natural frequency domain away from the region of the wave spectrum frequencies. As it can be seen in Figure 13, the small interface area between the TetraSpar natural frequencies and the irregular waves is an indicative of the very little probability of the structure vibrating in resonance with the waves.

Author Contributions: The authors E.B.V. , C.M.G. and N.G.K.M. contributed equally to this work. The paper is written as part of a master thesis at Aalborg University. M.T.A contributed with helping on the project scope and important inputs.

Conflicts of Interest: The authors declare no conflict of interest.

Abbreviations

The following abbreviations are used in this manuscript:

CG	Centre of gravity
COB	Centre of buoyancy
CW	Counterweight
DOF	Degree of Freedom
DTU	Danmark Teknisk Universitet
FAST	Fatigue Aerodynamics Structures Turbulence
FOWT	Floating Offshore Wind Turbine
LCOE	Levelised Cost of Energy
MWL	Mean Water Level
NREL	National Renewable Energy Laboratory
RAO	Response Amplitude Operator
TRL	Technology Readiness Level

References

1. E. Benitez-Villaespes, C.M. Gonzalez, N.G.K. Martin, M.T. Andersen, Transportation paper [change title] **2018**.
2. Henrik Stiesdal, Stiesdal Offshore Technologies **2017**.
3. J.B. Roberts, Estimation of non-linear ship roll damping from free-decay data **1985**.
4. C. Beels, J.C.C. Henriques, J. De Rouck, M.T. Pontes, G.De Backer, H.Verhaeghe, Wave energy resource in the North Sea **2007**.
5. C. Bak,F. Zahle, R. Bitsche, T. Kim, A. Yde, L.C. Henriksen, A. Natarajan, M.H. Hansen, DTU Wind Energy Report-I-0092 **2013**.
6. H. Bredmose, M.Borg, A. Pegalajar-Jurado, T.R. Nielsen, F.J. Madsen, A.K. Lomholt, R. Mikkelsen and M. Mirzaei, TetraSpar Floating Wind Turbine Scale Model Testing Summary Report :Semi-sub, Spar and TLP configuration; Technical report.**2017**.
7. F.J.Madsen, T.R. Nielsen, H. Bredmose, M. Borg, A.Pegalajar-Jurado, A.K. Lomholt, Scaled TetraSpar Floating Wind Turbine HAWC2 Model Report; Technical report. **2017**.
8. Stian K. Garvik, Magnus T. Bach-Gansmo and Morten T. Andersen, Parametric study of taut compliant mooring system compared to a catenary mooring **2018**.
9. WAMIT Inc., WAMIT user manual Version 7.2; in agreement with Massachusetts Institute of Technology (MIT). **2016**.
10. J.M. Jonkman, NREL, Dynamics Modeling and Loads Analysis of an Offshore Floating Wind Turbine; Technical report. **2007**.
11. F. Wendt, A. Robertson, J.Jonkman, Scaled TetraSpar FAST Model; Technical report. **2018**

Sample Availability: Samples of the compounds ...... are available from the authors.

Bibliography

Bak et al., 2013. C. Bak, F. Zahle, R. Bitsche, T. Kim, A. Yde, L.C. Henriksen, A. Natarajan and M.H. Hansen. *DTU Wind Energy Report-I-0092*, 2013.

Beels et al., 2007. C. Beels, J.C.C. Henriques, J. De Rouck, M.T. Pontes, G.De Backer and H.Verhaeghe. *Wave energy resource in the North Sea*. 2007.

EMODnet, 2016. EMODnet. *European marine observing and data network - portal for bathymetry*. http://www.emodnet-bathymetry.eu, 2016.

EWEA, 2017. EWEA. *Wind Energy in Europe: Outlook to 2020*, 2017.

F.J.Madsen et al., 2017. F.J.Madsen, T.R. Nielsen, H. Bredmose, M. Borg, A.Pegalajar-Jurado and A.K. Lomholt. *Scaled TetraSpar Floating Wind Turbine HAWC2 Model Report*, 2017.

Henrik Stiesdal, 2017. Henrik Stiesdal. *Stiesdal Offshore Technologies*, 2017.

Jonkman and NREL, 2007. J.M. Jonkman and NREL. *Dynamics Modeling and Loads Analysis of an Offshore Floating Wind Turbine*, 2007.

Journée and Massie, 2001. J.M.J. Journée and W.W. Massie. *Offshore Hydromechanics*, 2001.

Mathew Hall, 2017. University of Prince Edward Island Mathew Hall, School of Sustainable Design Engineering. *MoorDyn User's Guide*, 2017.

Musial et al., 2006. W. Musial, S. Butterfield and B. Ram. *Energy from Offshore Wind*, 2006.

NES, 2016. NES. *Offshore and onshore wind farms*, 2016.

New Energy Update, 2016. New Energy Update. *Bullish CAPEX cut for floating plant signals 2020s market challenge*. http://newenergyupdate.com/, 2016.

Remery and van Oortmerssen, 1973. G.F.M. Remery and G. van Oortmerssen. *The mean wave, wind and current forces on offshore structures and their role in the design of mooring systems*. 1973.

WAMIT Inc., 2016. WAMIT Inc. *WAMIT user manual Version 7.2; in agreement with Massachusetts Institute of Technology (MIT)*, 2016.

Experimental A

Towing assessment

Characterization of flow

According to [Remery and van Oortmerssen, 1973], the variation in velocity and direction of the current is very slow, and current may therefore be considered as a steady phenomenon. Although the bottom of the flume has a light slope that may induce an acceleration to the velocity particles. For the analytical and numerical solutions it is assumed that the bottom is flat due to two main reasons:

- The stretch with slope is located at the end of the flow itinerary, being around the 15% of the total itinerary.
- The slope is less than 5%.

Moreover due to the non-slip boundary condition, the current profile may be affected by both the flume walls and the bottom. For simplification and also due to the fact that the bottom surface has a considerably higher roughness compared to the walls, it is assumed that the walls do not affect to the current profile and therefore it will be only a function of the depth.

According to the design requirements for offshore wind turbines given by [DNV (2000)]. The current speed profile can be defined by Eq.(A.1).

$$v(z) = a \cdot \left(\frac{z+d}{d} \right)^{\frac{1}{7}} \tag{A.1}$$

$v(z)$	current velocity at height z
z	height above MSWL (negative in downward direction)
a	fit parameter
d	water depth

The measured velocities by the propeller in the experiment are presented in Table A.1.

Table A.1. Measured mean velocities with the propeller at different heights, z

At $z = $ **-0.06** **[m]**	
Pump Frequency [Hz]	Mean Velocity [m/s]
30	0.19
40	0.31
50	0.42
At $z = $ **-0.30** **[m]**	
Pump Frequency [Hz]	Mean Velocity [m/s]
30	0.11
40	0.22
50	0.29

It is also assumed that the velocity at the bottom is zero. There are three depths where the velocity is known and to which Eq.(A.1) is fitted. Figure A.1 represents the current speed distribution for each pump frequency.
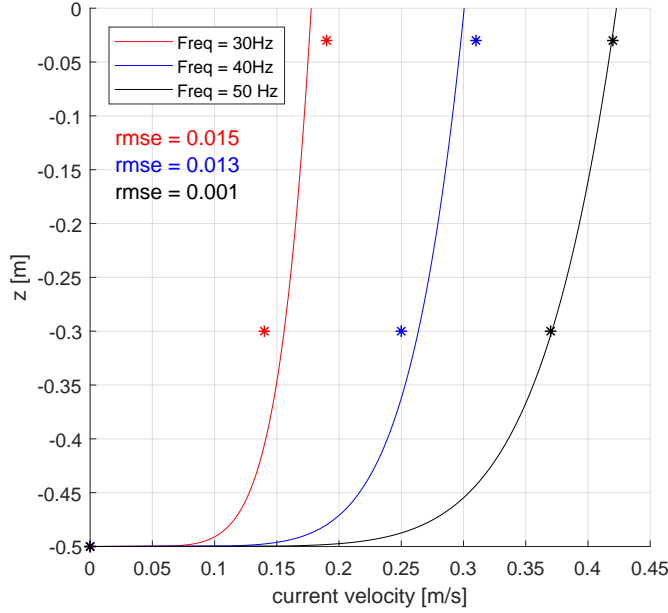
Figure A.1. Mean current speed as a function of depth.

The stars indicate measured values and the lines indicate the fit. *rmse* stands for the root of the mean square error and the fitting is done by finding the fitting parameter a that gives the least *rmse*.

Experimental plan and results

In Table A.2 is presented the experimental campaign procedure in the wave flume. The experimental data results are show in Figures A.2 and A.3.

Table A.2. Experimental test plan.

Date	Log nr.	Description	Test name	Conf.	Pump freq. [Hz]
08-03-2018	1	Towing Test 1	tow_lc_76	B1	30
08-03-2018	2	Towing Test 2	tow_lc_78	B1	40
08-03-2018	3	Towing Test 3	tow_lc_80	B1	50
08-03-2018	4	Towing Test 4	tow_lc_82	B2	30
08-03-2018	5	Towing Test 5	tow_lc_84	B2	40
08-03-2018	6	Towing Test 6	tow_lc_86	B2	50
08-03-2018	7	Towing Test 7	tow_lc_88	A2	30
08-03-2018	8	Towing Test 8	tow_lc_90	A2	40
08-03-2018	9	Towing Test 9	tow_lc_92	A2	50
08-03-2018	10	Towing Test 10	tow_lc_94	A1	30
08-03-2018	11	Towing Test 11	tow_lc_96	A1	40
08-03-2018	12	Towing Test 12	tow_lc_98	A1	50
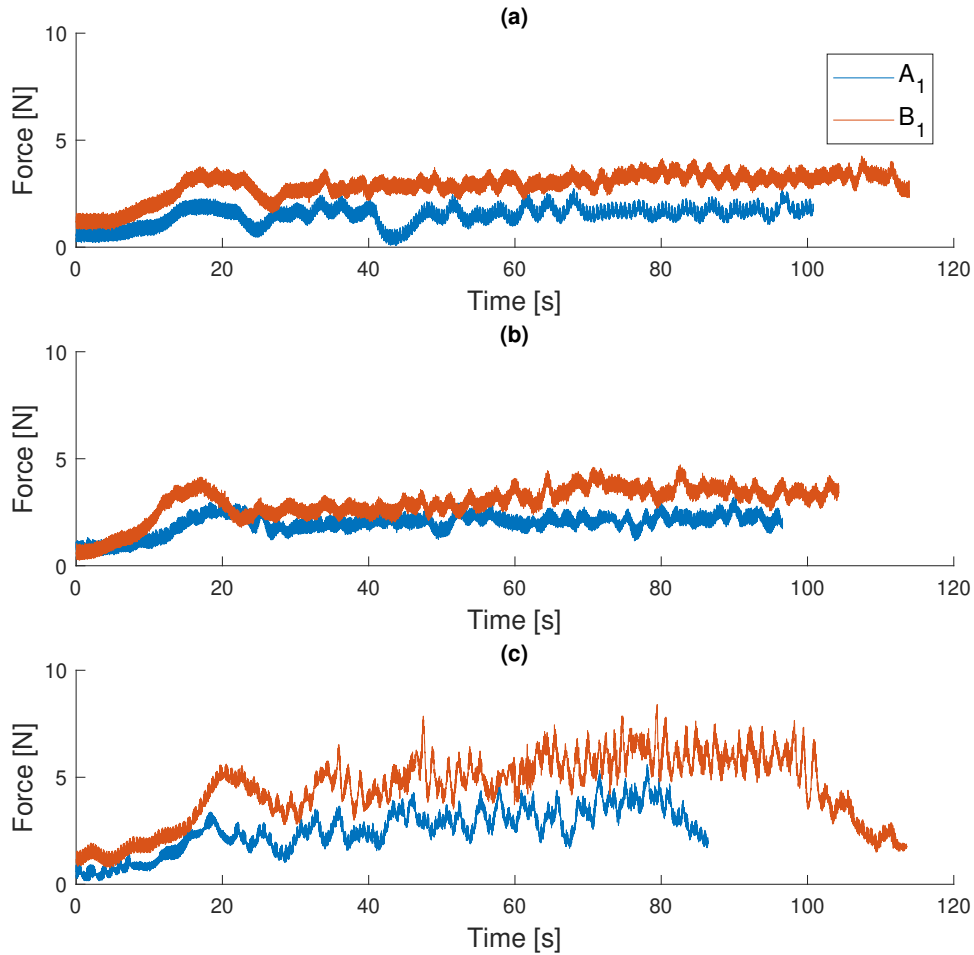
Figure A.2. Experimental towing data in configurations A_1 and B_1. **(a)** Test n°10 and 1, where $v = 0.19\ m/s$. **(b)** Test n°11 and 2, where $v = 0.31\ m/s$. **(c)** Test n°12 and 3, where $v = 0.42\ m/s$.
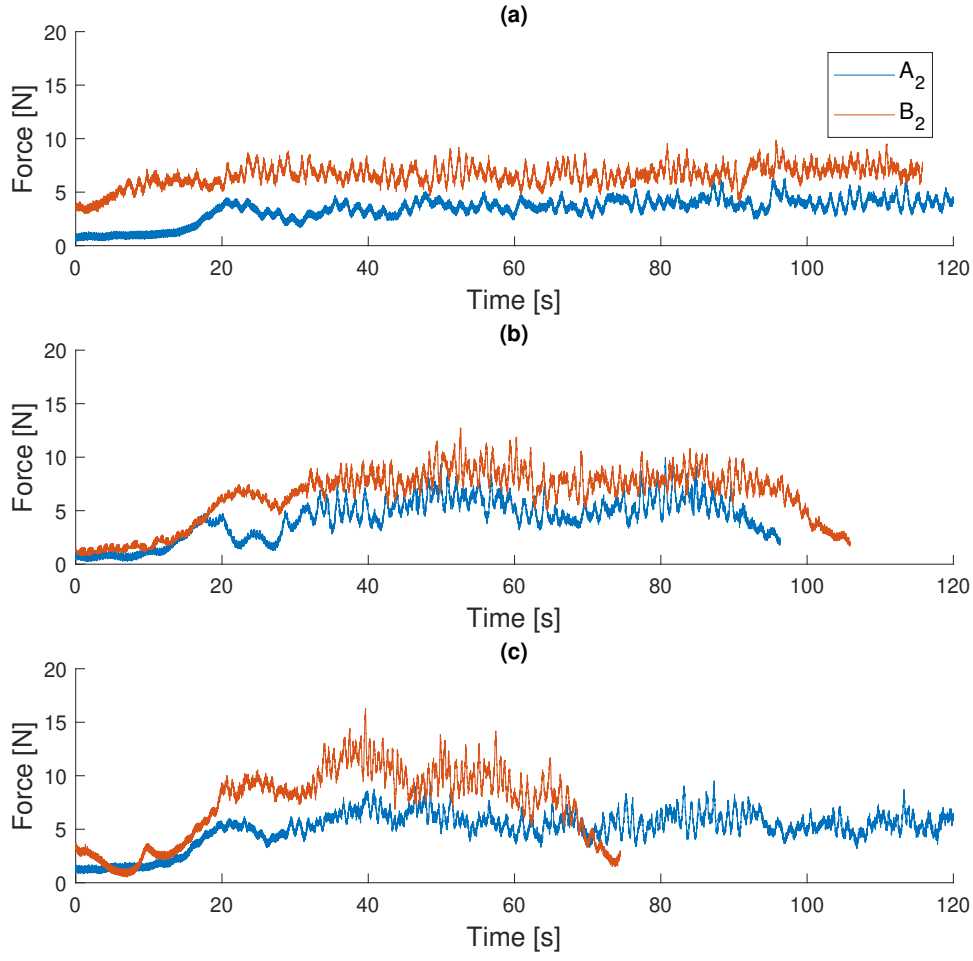
Figure A.3. Experimental towing data in configurations A_2 and B_2. **(a)** Test n°7 and 4, where $v = 0.19 \, m/s$. **(b)** Test n°8 and 5, where $v = 0.31 \, m/s$. **(c)** Test n°9 and 6, where $v = 0.42 \, m/s$.

Installation assessment

Experimental plan and results

In Tables A.3 and A.4 are presented the experimental campaign procedure in the wave basin. The coloured lines represents the data used in further analysis, such as the calibration of numerical models, the determination of natural frequencies, damping ratio and response amplitude operator. The free oscillation test data is represented in Figures A.5 and A.4. The regular wave data used are shown in Figures A.6 and A.7. The data used for further calculations are represented in red.

Table A.3. Experimental test plan for the spar configuration.

Date	Log nr	Description	Location	Test name	Wave Height [m]	Wave Period [s]
Decay test w/o mooring w. counterweight						
21-03-2018	1	Decay Test Pitch 1	Wave Bassin	p_acc_169	-	-
21-03-2018	2	Decay Test Pitch 2	Wave Bassin	p_acc_170	-	-
21-03-2018	3	Decay Test Heave 1	Wave Bassin	h_acc_172	-	-
21-03-2018	4	Decay Test Heave 2	Wave Bassin	h_acc_173	-	-
21-03-2018	6	Decay Test Roll 1	Wave Bassin	r_acc_175	-	-
21-03-2018	7	Decay Test Roll 2	Wave Bassin	r_acc_176	-	-
Decay test spar configuration counterweight depth 1015mm w. mooring						
22-03-2018	8	Decay Test Pitch 1	Wave Bassin	p_acc_178	-	-
22-03-2018	9	Decay Test Pitch 2	Wave Bassin	p_acc_179	-	-
22-03-2018	10	Decay Test Heave 1	Wave Bassin	h_acc_181	-	-
22-03-2018	11	Decay Test Heave 2	Wave Bassin	h_acc_182	-	-
22-03-2018	12	Decay Test Roll 1	Wave Bassin	r_acc_184	-	-
22-03-2018	13	Decay Test Roll 2	Wave Bassin	r_acc_185	-	-
22-03-2018	14	Decay Test Surge	Wave Bassin	s_acc_186	-	-
Wave tests spar configuration counterweight depth 1015mm w. mooring						
21-03-2018	15	Wave Test 1	Wave Bassin	w_acc_187	0.0625	1.163
21-03-2018	16	Wave Test 2	Wave Bassin	w_acc_188	0.0625	0.774
21-03-2018	17	Wave Test 3	Wave Bassin	w_acc_189	0.0625	0.904
21-03-2018	18	Wave Test 4	Wave Bassin	w_acc_190	0.0625	1.033
21-03-2018	19	Wave Test 5	Wave Bassin	w_acc_191	0.07	0.774
21-03-2018	20	Wave Test 6	Wave Bassin	w_acc_192	0.07	0.904
21-03-2018	21	Wave Test 7	Wave Bassin	w_acc_193	0.07	1.033
21-03-2018	22	Wave Test 8	Wave Bassin	w_acc_194	0.07	1.173
21-03-2018	23	Wave Test 9	Wave Bassin	w_acc_195	0.079	0.774
21-03-2018	24	Wave Test 10	Wave Bassin	w_acc_196	0.079	0.904
21-03-2018	25	Wave Test 11	Wave Bassin	w_acc_197	0.079	1.033
21-03-2018	26	Wave Test 12	Wave Bassin	w_acc_198	0.079	1.2277
21-03-2018	27	Wave Test 13	Wave Bassin	w_acc_199	0.0875	0.774
21-03-2018	28	Wave Test 14	Wave Bassin	w_acc_200	0.0875	0.904
21-03-2018	29	Wave Test 15	Wave Bassin	w_acc_201	0.0875	1.033
21-03-2018	30	Wave Test 16	Wave Bassin	w_acc_202	0.0875	1.28

Table A.4. Experimental test plan for the hook-up configuration.

Date	Log nr	Description	Location	Test name	Wave Height [m]	Wave Period [s]
Decay test w. mooring w/o counterweight						
22-03-2018	31	Decay Test Pitch 1	Wave Bassin	p_acc_193	-	-
22-03-2018	32	Decay Test Heave 1	Wave Bassin	h_acc_196	-	-
22-03-2018	33	Decay Test Heave 2	Wave Bassin	h_acc_197	-	-
22-03-2018	34	Decay Test Roll 1	Wave Bassin	r_acc_199	-	-
22-03-2018	35	Decay Test Roll 2	Wave Bassin	r_acc_200	-	-
22-03-2018	36	Decay Test Roll 3	Wave Bassin	r_acc_201	-	-
Wave test w. mooring w/o counterweight						
22-03-2018	37	Wave Test 1	Wave Bassin	w_acc_203	0.0625	0.774
22-03-2018	38	Wave Test 2	Wave Bassin	w_acc_204	0.0625	0.904
22-03-2018	39	Wave Test 3	Wave Bassin	w_acc_205	0.0625	1.033
22-03-2018	40	Wave Test 4	Wave Bassin	w_acc_215	0.0625	1.163
22-03-2018	41	Wave Test 5	Wave Bassin	w_acc_216	0.07	0.774
22-03-2018	42	Wave Test 6	Wave Bassin	w_acc_217	0.07	0.904
22-03-2018	43	Wave Test 7	Wave Bassin	w_acc_218	0.07	1.033
22-03-2018	44	Wave Test 8	Wave Bassin	w_acc_219	0.07	1.173
22-03-2018	45	Wave Test 9	Wave Bassin	w_acc_220	0.079	0.774
22-03-2018	46	Wave Test 10	Wave Bassin	w_acc_221	0.079	0.904
22-03-2018	47	Wave Test 11	Wave Bassin	w_acc_222	0.079	1.033
22-03-2018	48	Wave Test 12	Wave Bassin	w_acc_223	0.079	1.2277
22-03-2018	49	Wave Test 13	Wave Bassin	w_acc_224	0.0875	0.774
22-03-2018	50	Wave Test 14	Wave Bassin	w_acc_225	0.0875	0.904
22-03-2018	51	Wave Test 15	Wave Bassin	w_acc_226	0.0875	1.033
22-03-2018	52	Wave Test 16	Wave Bassin	w_acc_227	0.0875	1.28
22-03-2018	53	Zero reading	Wave Bassin	zero_acc_228	-	-
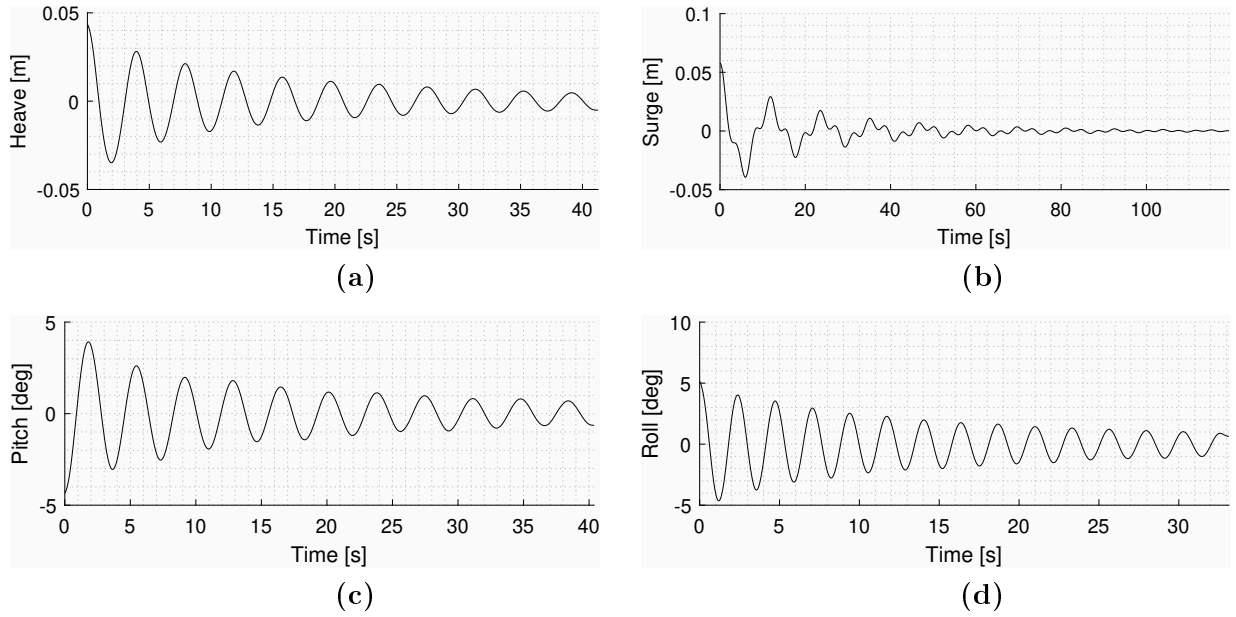
Figure A.4. Decay test data in hook-up configuration. **(a)** Test n°40 **(b)** Test n°44 **(c)** Test n°48 **(d)** Test n°52
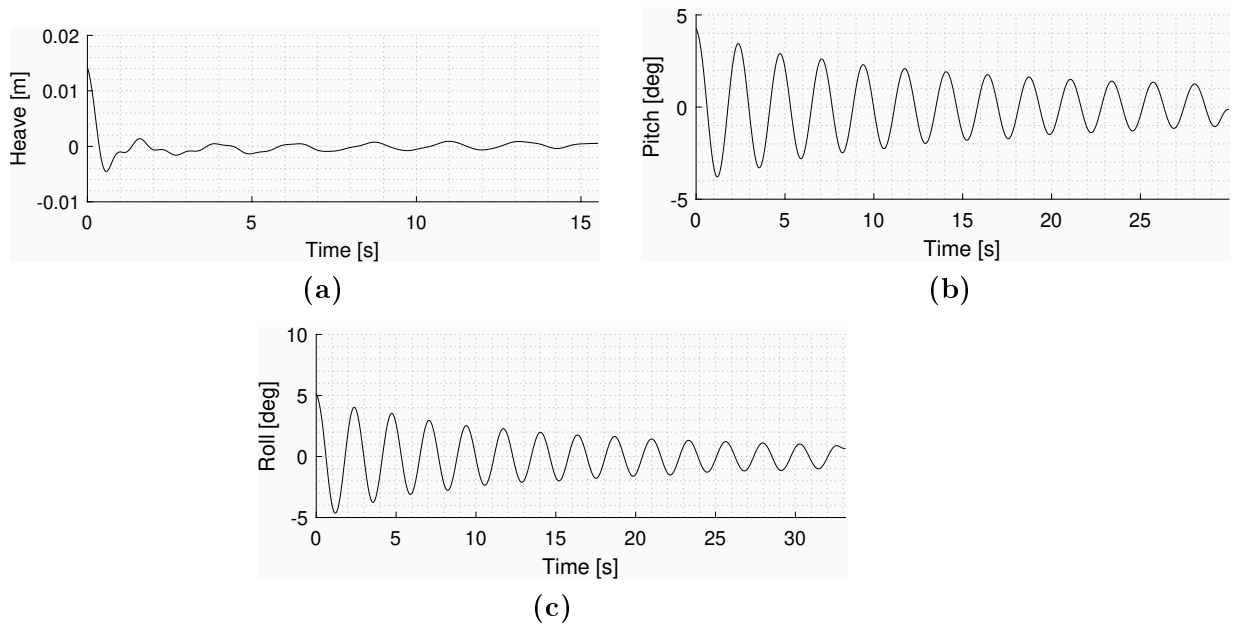
Figure A.5. Decay test data in hook-up configuration. **(a)**Test n°11 **(b)**Test n°14 **(c)**Test n°8.
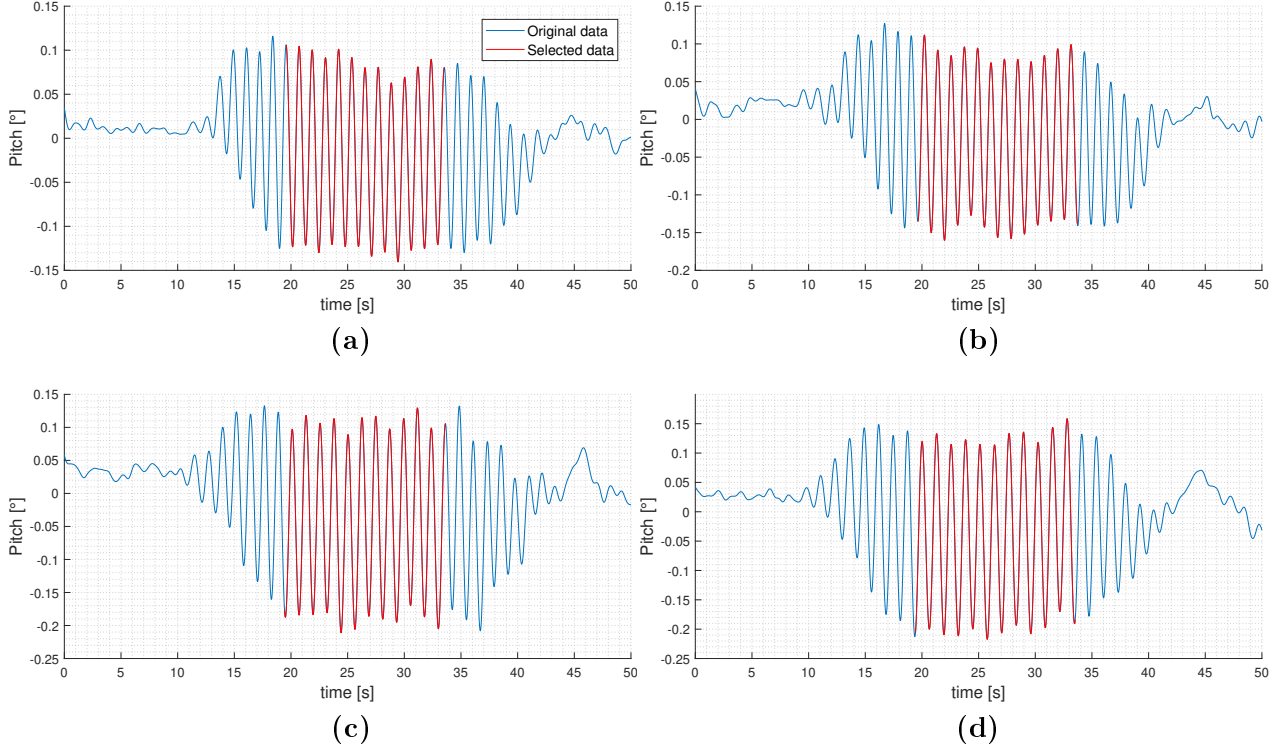
Figure A.6. Regular wave data in spar configuration. Red color stands for the data selected for the analysis. **(a)** Test n°15 **(b)** Test n°22 **(c)** Test n°26 **(d)** Test n°30
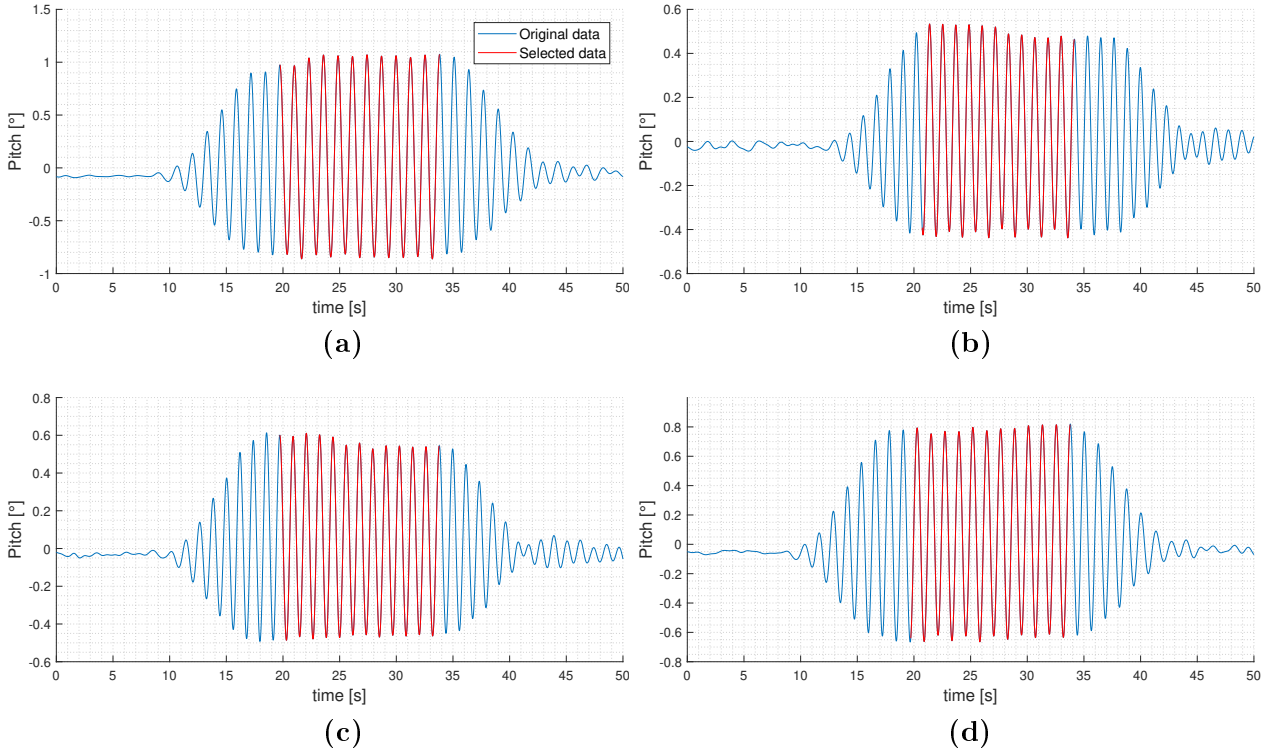
Figure A.7. Regular wave data in hook-up configuration. Red color stands for the data selected for the analysis. **(a)** Test n°40 **(b)** Test n°44 **(c)** Test n°48 **(d)** Test n°52

Numerical: FAST B

FAST modules

FAST operates with different modules that can be interfaced to achieve the coupled time domain aero-hydro-servo-elastic simulation. This feature is necessary to analyse the dynamic response from combined wind and wave loading because both can affect the wind turbine motions, loads, and it power production. Figure B.1 shows a general overview of the different modules present in FAST.
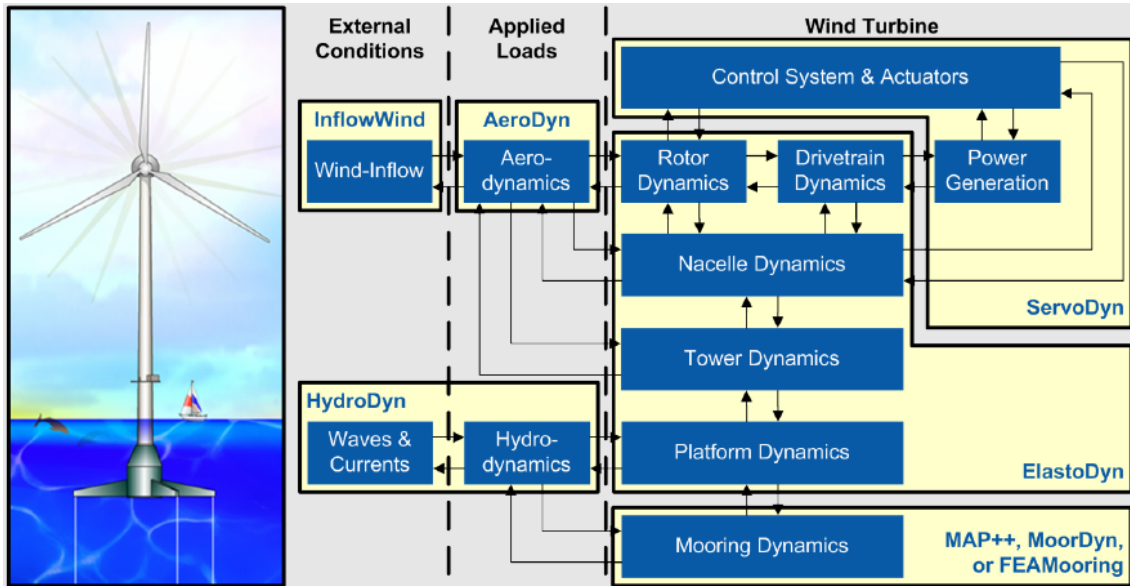
Figure B.1. Interactive modules to achieve aero-hydro-servo-elastic simulation. [Jonkman and NREL, 2007].

The AeroDyn module accounts for the applied aerodynamic and gravitational loads, the behaviour of the control and protection systems, and the structural dynamics of the wind turbine. AeroDyn is not enabled as simulations are performed in absence of wind forces. Regarding the upper part of the structure, the ServoDyn module allows for the control and electrical-drive model of the wind turbine. In the same way, ServoDyn is not implemented in the simulations as it is not the main focus of the study. In this project only ElastoDyn, MoorDyn and HydroDyn modules are considered, which main characteristics are here presented.

ElastoDyn module

First, the ElastoDyn or structural dynamic module, defines the geometry of the whole wind turbine and describes which DOF are enabled for the simulation. It is split in different callable modules with different input files, including structural models of the rotor, nacelle, drivetrain, tower and platform.

MoorDyn module

A mooring system is made up of a number of cables that are attached to the floating support platform at fairlead connections, with the opposite ends anchored to the seabed. Restoring loads from the mooring system are obtained from the quasi-static mooring line module MoorDyn that accounts for the elastic stretching of an array of homogenous taut or slack catenary lines with seabed interaction. This module discretizes the mooring line dynamics over its length, using a lumped mass approach. The lines are split into $n-$ number of segments of equal size and connected by $n+1$ number of nodes. The lower end anchor is the node zero, while node n is the one attached to the structure. Figure B.2 shows graphically the mooring line model structure.
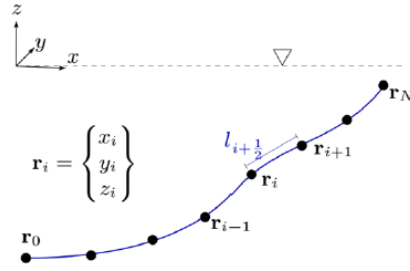
Figure B.2. MooringDyn model structure. [Mathew Hall, 2017]

The properties of diameter, density, unstretched length and Young's modulus are the same for each of the segments in the mooring line. The ends of the lines are defined as Connection objects, existing three types:

- fixed, for nodes that never move.
- vessel, which corresponds to nodes that can move, such as fairlead connection points.
- connect nodes, which are used to connect different mooring lines together.

Hydrodynamic loads are calculated directly at the node points rather than at the segment centers. Further details of the mooring lines configurations can be found in [Mathew Hall, 2017].

HydroDyn module

HydroDyn is a module that computes the applied hydrodynamic loads in the time domain. It is a hydrodynamics module to account for linear hydrostatic restoring; nonlinear viscous drag from incident-wave kinematics, sea currents, and platform motion; the added-mass and damping contributions from linear wave radiation, including free-surface memory effects; and the incident-wave excitation from linear diffraction in regular or irregular seas.

Hydrodynamic loads depend on the support platform's geometry, so HydroDyn need to call an output from another computer program: WAMIT (Wave Analysis at MIT) [WAMIT Inc., 2016]. It offers a great capability to model complex 3D surfaces using numerical panel method in the frequency domain. It solves linearized hydrodynamic radiation and diffraction problems for the interaction of surface waves with offshore platforms with a geometry previously specified.

A summary of the complex calculation procedure of the HydroDyn module is presented in Figure B.3.
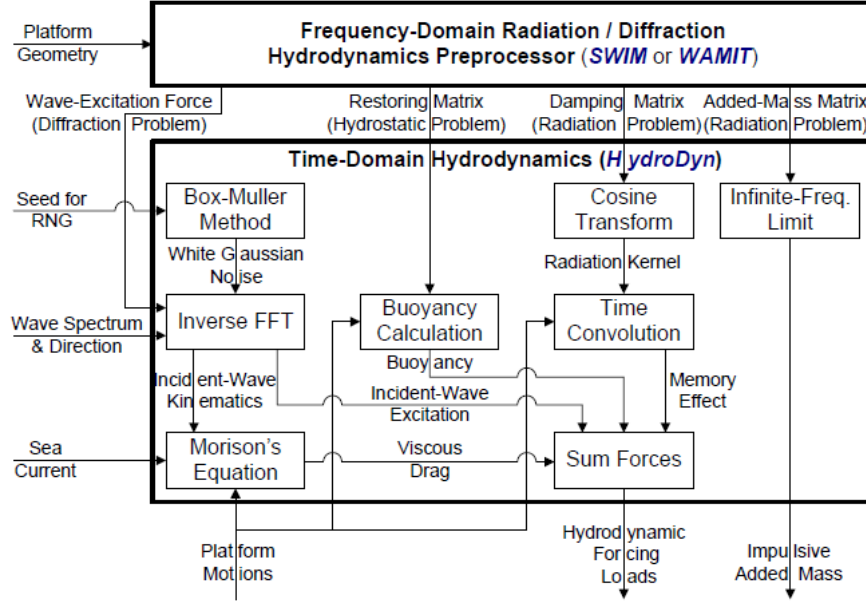
Figure B.3. HydroDyn calculation procedure. [Jonkman and NREL, 2007]

Calibration

The combined dynamics of the turbine and floater can be expressed in a simplified equation of motion, shown in Eq.(B.1). It is intended to give a sense of the different terms acting and how they have been modified in the calibration process. The force F is in reality the sum of the total forces, such as the hydrodynamic,F_i^H, mooring F_i^M and gravitational forces F_i^G, that are acting on the combined system. Wind forces are zero in this case as they are not considered.

$$M_{ij}\ \ddot{x}_i(t) + C_{ij}\ \dot{x}_i(t) + K_{ij}\ x_i(t) = F_i^G + F_i^H + F_i^M + F_i^W \tag{B.1}$$

where $x_i(t)$ corresponds to the 6 DOFs along time: surge, sway, heave, roll, pitch and yaw; $\dot{x}_i(t)$ and $\ddot{x}_i(t)$ corresponds to the first and second displacement derivative respectively. M_{ij} stands for the mass matrix of the whole system (including the contribution of the added mass), C_{ij} is the linear damping matrix and K_{ij} the stiffness matrix.

At the same time, the hydrodynamic force can be divided in different terms, yielding:

$$F_i^H = F_i^W + \rho\ g\ V_0 - C_{ij}^{Hydro}\ x_j - \int_0^t K_{ij}(t - \tau)\ \dot{x}_j\ (\tau)d\tau \tag{B.2}$$

where the first term F_i^W represents the incident waves excitation loads on the floating structure; the second and third terms stand for the contribution from hydrostatic loads and the last term represent the load contribution from wave radiation damping and also the contribution of the added mass not taken into account in the M_{ij} matrix. For the calibration, special attention is paid to both terms that comprise the hydrostatic loads. The first of these terms, $\rho\,g\,V_0$, represents the buoyant force from Archimede's principle, being ρ the water density, g the gravity acceleration and V_0 the water volume displaced by the structure. The second of these terms, $-C_{ij}^{Hydro}\,x_j$, represents the variation in the hydrostatic force and moment due to the effects of the water plane area and the center of buoyancy (COB) when the TetraSpar is being displaced. C_{ij}^{Hydro} is the hydrostatic restoring stiffness matrix and x_j stands for the transposed vector support platform displacements. The vertical location of the COB of the structure, z_{cob}, affects the hydrostatic load when the vector position of the COB changes with the displacement of the structure $(x_j(t))$. The cross product of the buoyancy force with the vector position of the COG produces a hydrostatic moment about the support platform reference point. Similarly, the water plane area of the floating structure in its undisplaced position, A_0, influence the hydrostatic load due to the fact that the water volume displaced changes when the structure is being displaced. When the submerged part of the structure is symmetrical with respect to the vertical $xz-$ and $yz-$ planes, the only non zero values of C_{ij}^{Hydro} are components (3,3), (4,4), (5,5). Matrix C_{ij}^{Hydro} is shown in Eq. (B.3).

$$C_{ij}^{Hydro} = \begin{pmatrix} 0 & 0 & 0 & 0 & 0 & 0 \\ 0 & 0 & 0 & 0 & 0 & 0 \\ 0 & 0 & \rho\,g\,A_0 & 0 & 0 & 0 \\ 0 & 0 & 0 & \rho\,g\iint\limits_{A_0} y^2\,dA + \rho\,g\,V_0\,z_{cob} & 0 & 0 \\ 0 & 0 & 0 & 0 & \rho\,g\iint\limits_{A_0} x^2\,dA + \rho\,g\,V_0\,z_{cob} & 0 \\ 0 & 0 & 0 & 0 & 0 & 0 \end{pmatrix}$$

(B.3)

Body weight is important for the pitch and roll restoring of deep-drafted floating platforms, such as the TetraSpar. All the terms comprised in F^H are considered within WAMIT calculations for the floater, but not for the CW. Therefore, to calibrate the model, the contribution of the CW has to be taken into account in the hydrostatic restoring stiffness matrix. In this case, there is no water plane area term as the CW is completely submerged; therefore the non zero values in Eq. (B.4) are elements (4,4) and (5,5), which adjustment stands for the mentioned roll and pitch restoring.

$$C_{ij}^{Hydro} = \begin{pmatrix} 0 & 0 & 0 & 0 & 0 & 0 \\ 0 & 0 & 0 & 0 & 0 & 0 \\ 0 & 0 & 0 & 0 & 0 & 0 \\ 0 & 0 & 0 & \rho\,g\,V_0\,z_{cob} & 0 & 0 \\ 0 & 0 & 0 & 0 & \rho\,g\,V_0\,z_{cob} & 0 \\ 0 & 0 & 0 & 0 & 0 & 0 \end{pmatrix}$$

(B.4)

The methodology implemented in FAST for the calibration of the system damping consists in adding a global linear damping matrix, C_{ij}^* to the equation of motion in Eq. (B.1) to form Eq. (B.5).

$$M_{ij}\ \ddot{x}_i(t) + C_{ij}\ \dot{x}_i(t) + C_{ij}^*\ \dot{x}_i(t) + K_{ij}\ x_i(t) = F_i^G + F_i^H + F_i^M + F_i^W \qquad (B.5)$$

In this case, only elements along the main diagonal of C_{ij}^* have non zero values. These values are obtained iteratively through trial and error. First, the uncalibrated models are presented from Figure B.4 to give the reader an idea of the rough data of the numerical simmulations. The results from the calibrated models with added linear damping can be seen right after the uncalibrated test of each configuration. From Figures B.4 to B.21 both uncalibrated and calibrated free decay tests and damping ratios for hook-up and spar configurations are presented. Likewise, the regular wave response of the calibrated models are compared to the experimental results in Figures B.22 and B.23.

Uncalibrated hook-up free decay tests
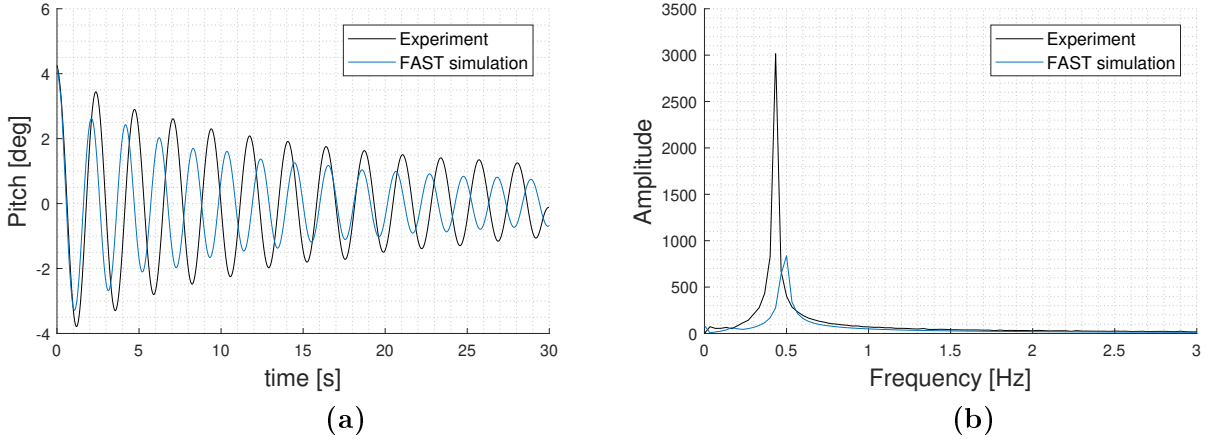
Figure B.4. Uncalibrated pitch decay test.
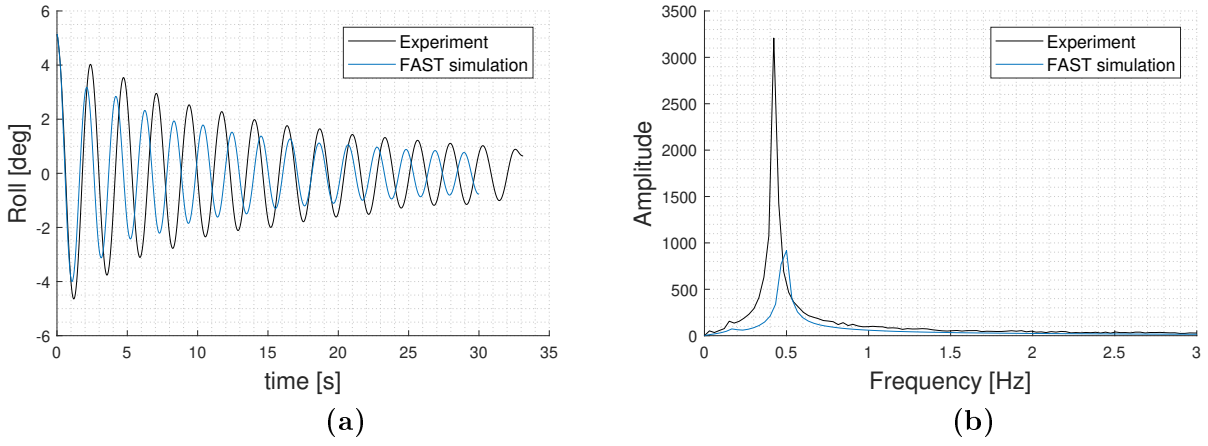
Figure B.5. Uncalibrated roll decay test.
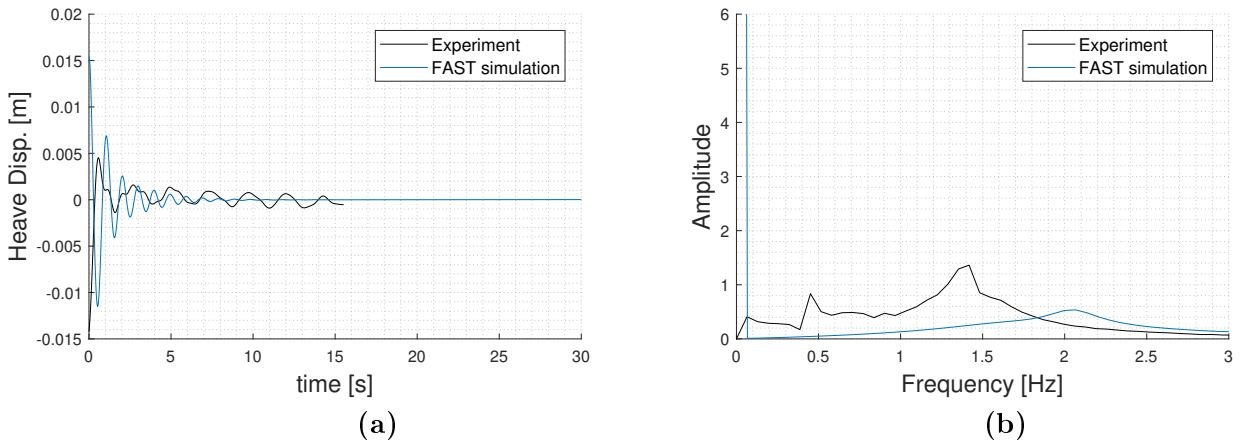
Figure B.6. Uncalibrated heave decay test.

Calibrated hook-up free decay tests
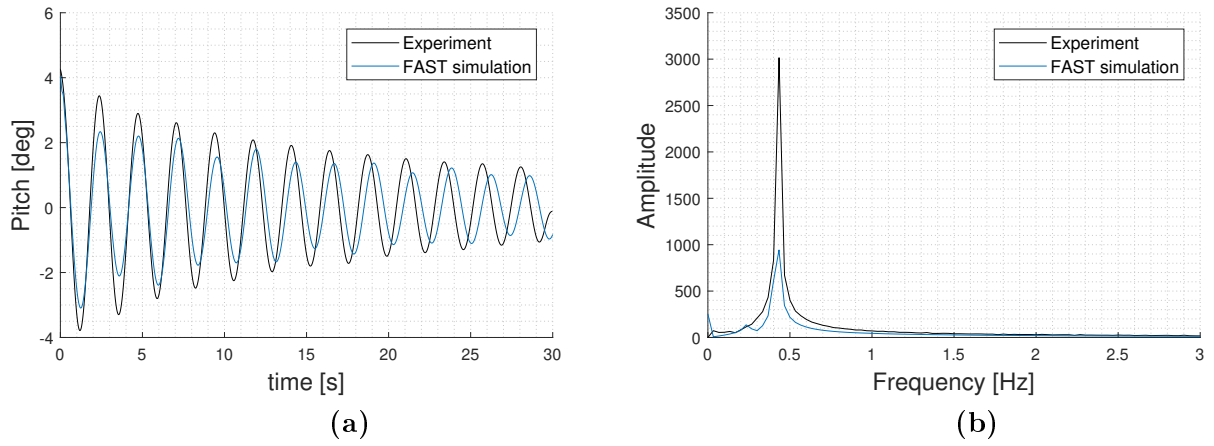
Figure B.7. Calibrated pitch decay test.
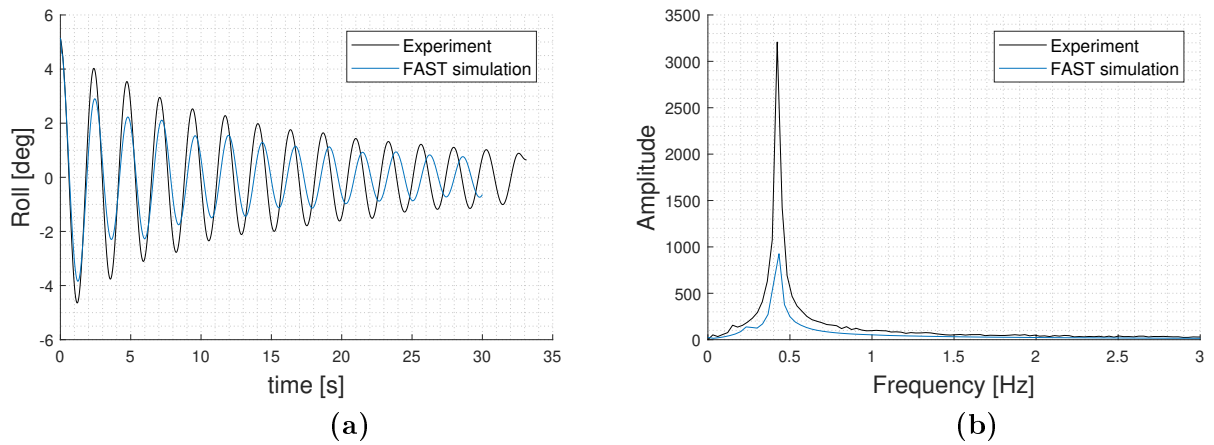
Figure B.8. Calibrated roll decay test.
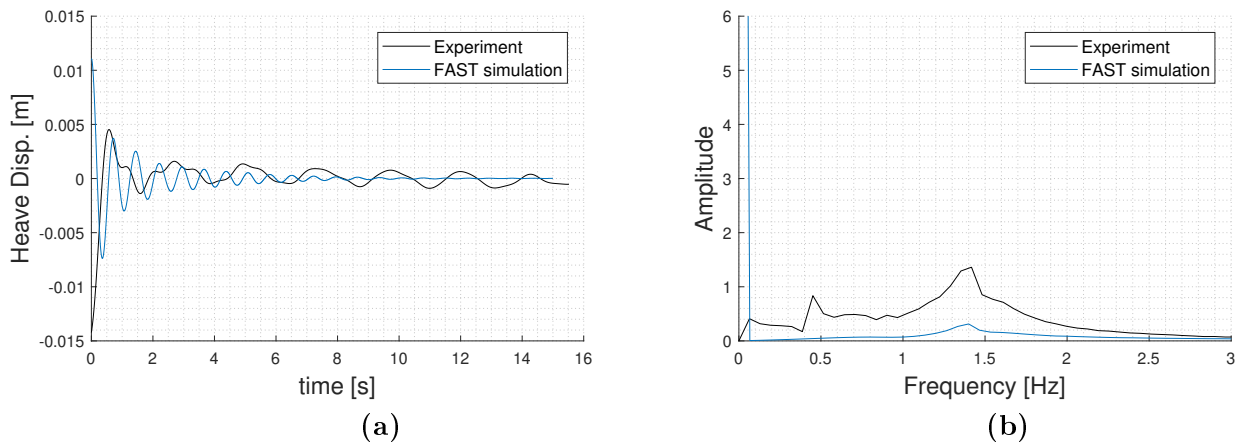
Figure B.9. Calibrated heave decay test.

Uncalibrated spar free decay tests

(a)

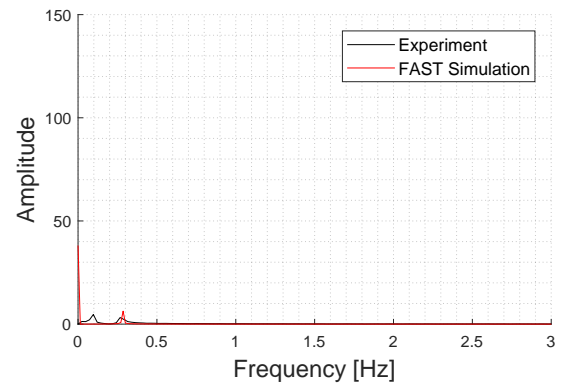(b)
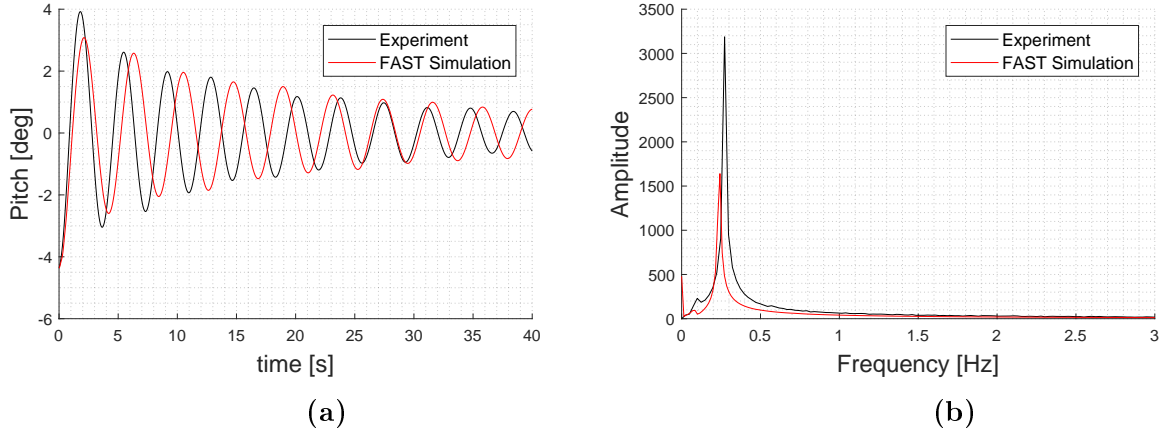
Figure B.10. Uncalibrated pitch decay test.

(a)

(b)
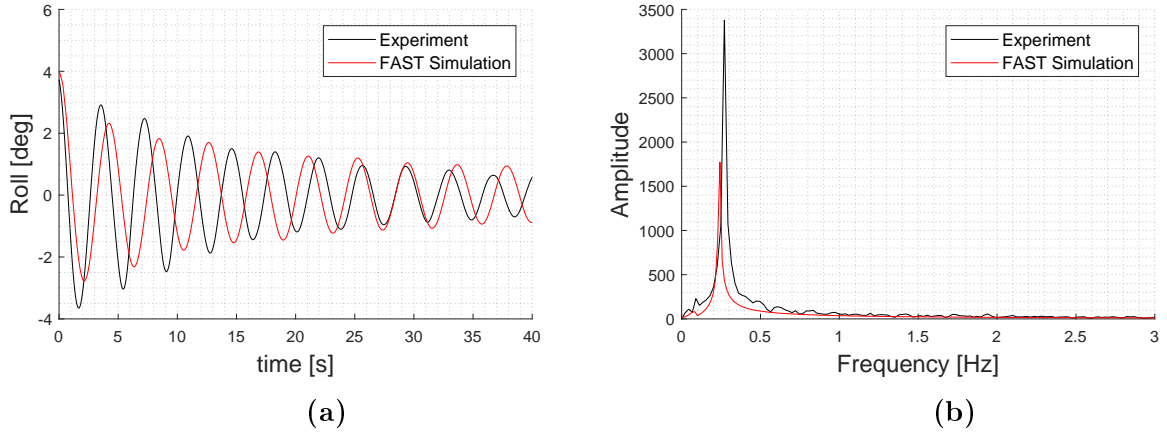
Figure B.11. Uncalibrated roll decay test.

(a)

(b)
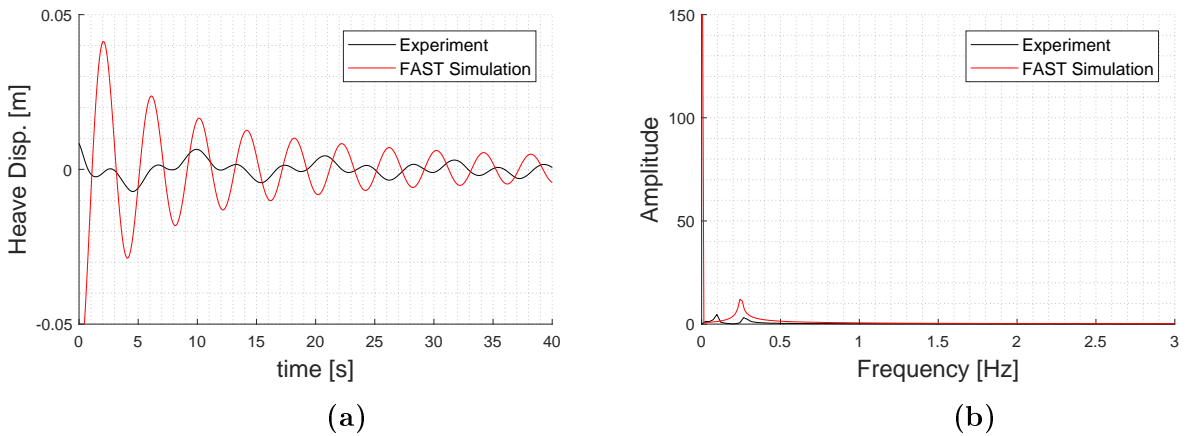
Figure B.12. Uncalibrated heave decay test.

Calibrated spar free decay tests
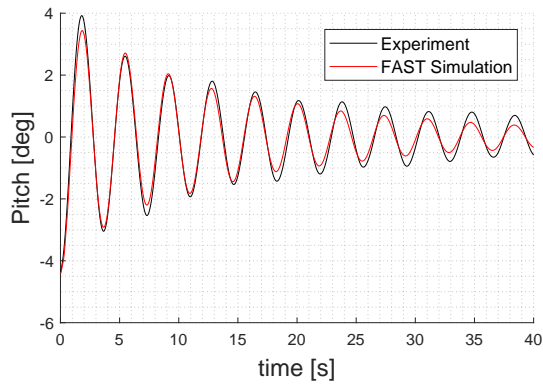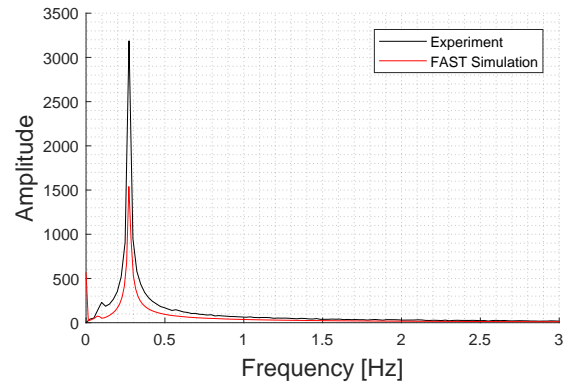
Figure B.13. Calibrated pitch decay test.
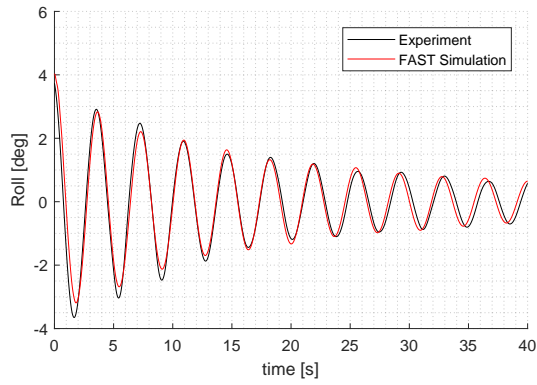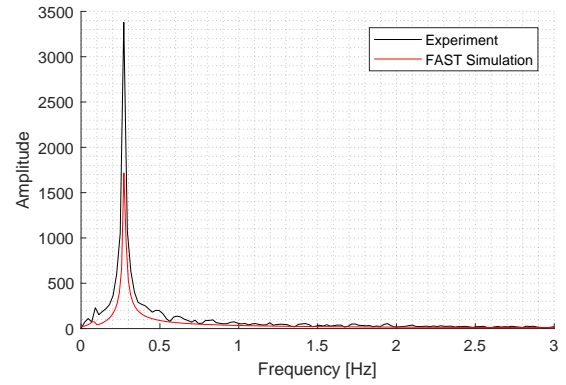
Figure B.14. Calibrated roll decay test.
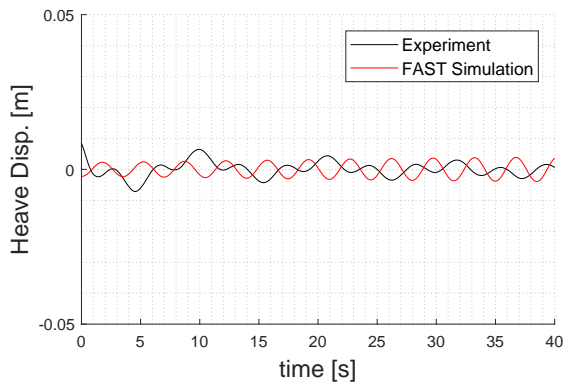
Figure B.15. Calibrated heave decay test.

Unalibrated damping ratios
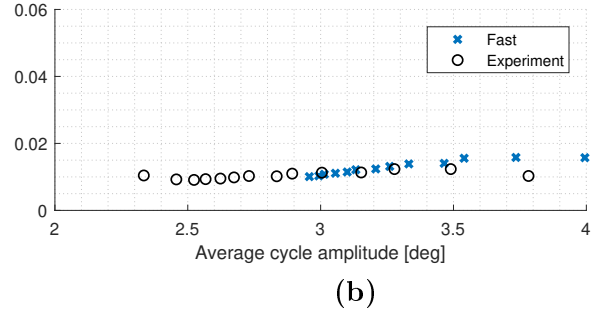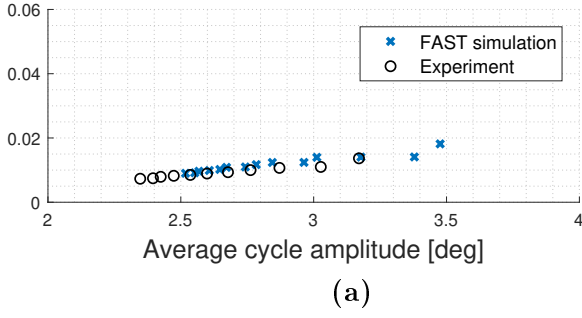
Figure B.16. Uncalibrated damping ratios.**(a)** Pitch test. **(b)** Roll test.
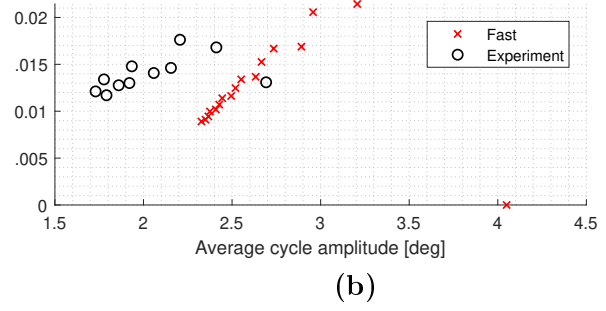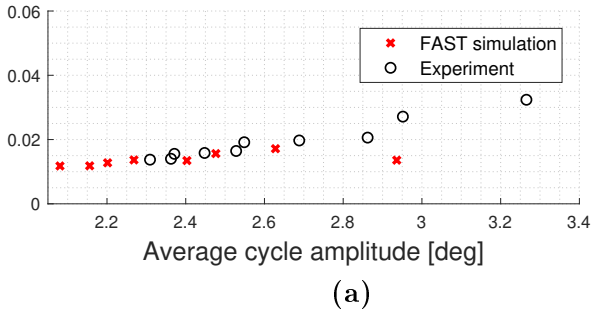
Figure B.17. Uncalibrated damping ratios.**(a)** Pitch test. **(b)** Roll test.
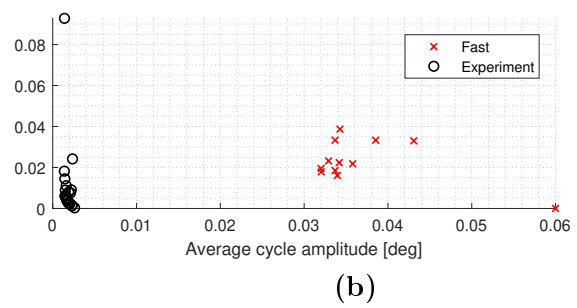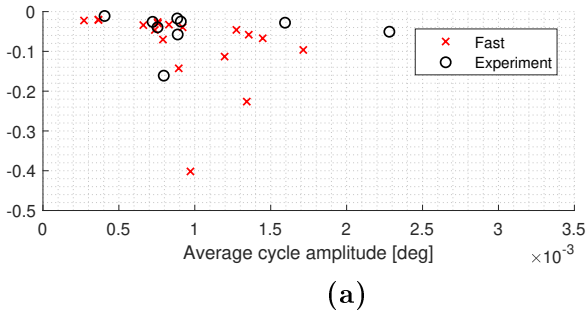
Figure B.18. Uncalibrated damping ratios.**(a)** Heave test. **(b)** Surge test.

Calibrated damping ratios
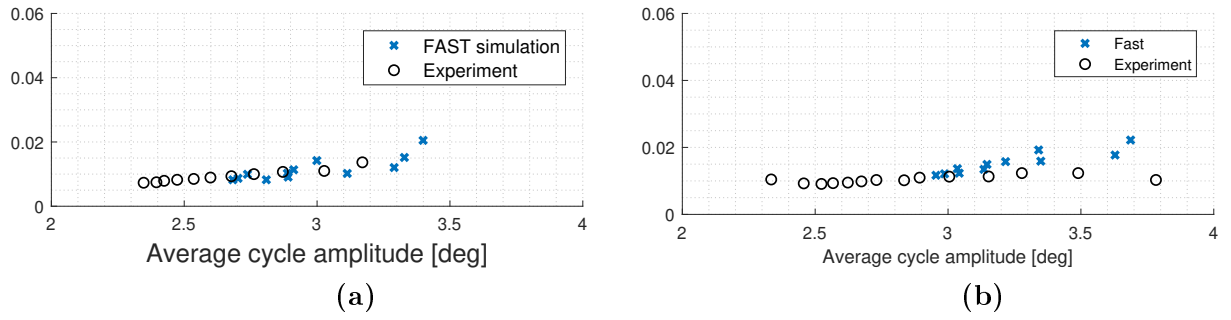
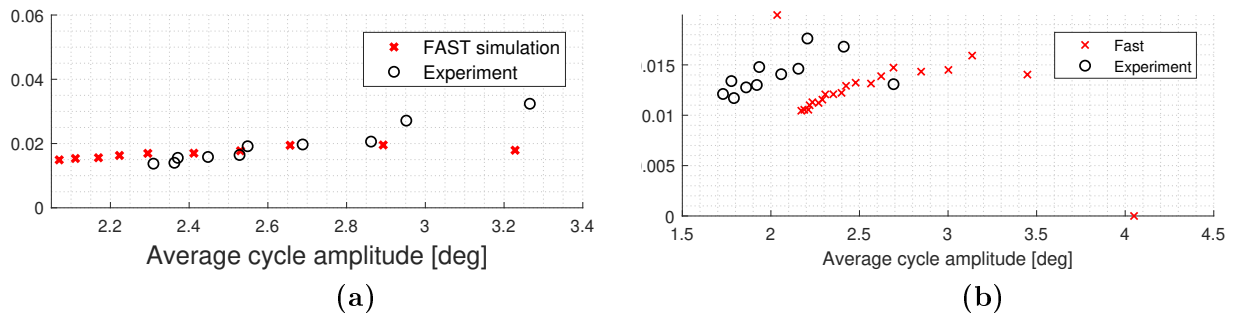*Figure B.19.* Calibrated damping ratios.**(a)** Pitch test. **(b)** Roll test.

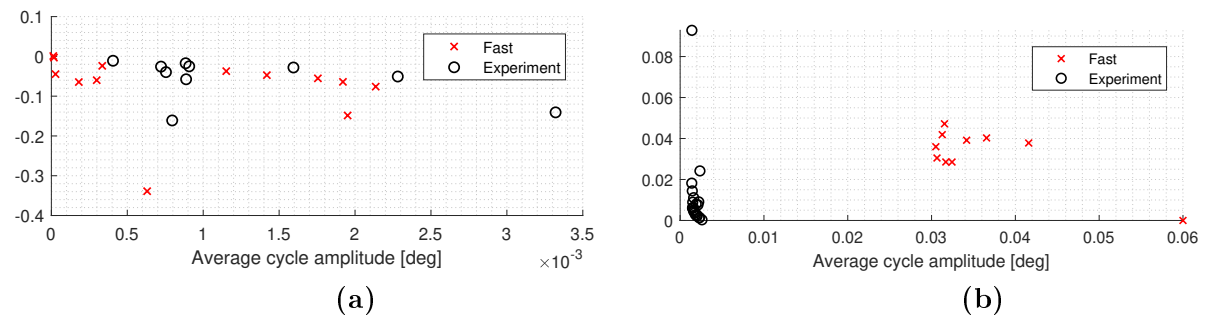*Figure B.20.* Calibrated damping ratios.**(a)** Pitch test. **(b)** Roll test.

Figure B.21. Uncalibrated damping ratios.**(a)** Heave test. **(b)** Surge test.
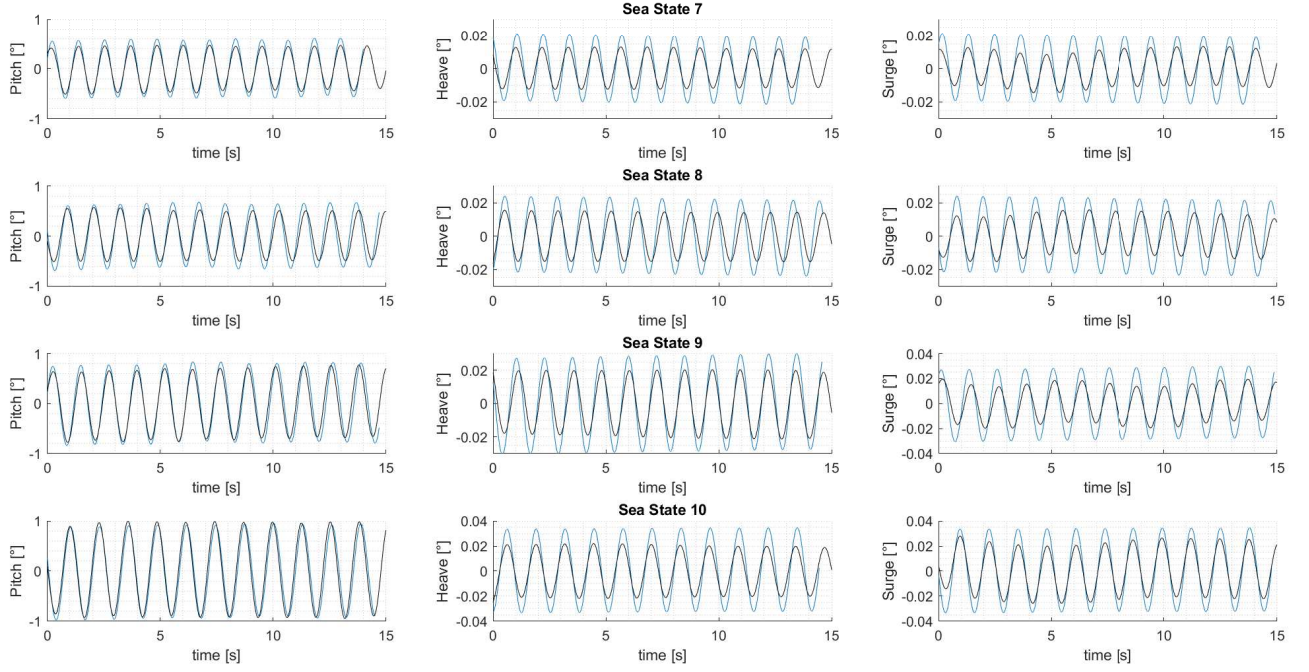
Regular waves response

Figure B.22. Structural response to regular waves in hook-up configuration. Blue signal stands for FAST while the black signal stands for the experimental response.
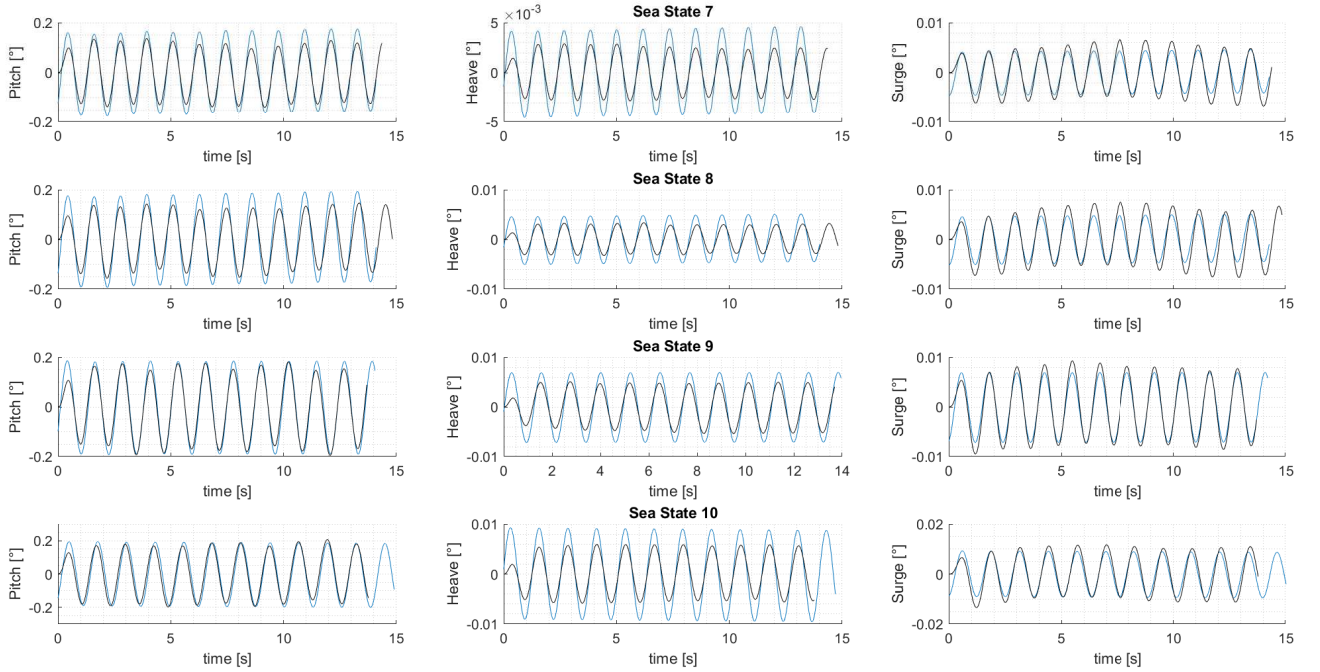

Figure B.23. Structural response to regular waves in spar configuration. Blue signal stands for FAST while the black signal stands for the experimental response.